

UiO : **University of Oslo**

Vegard Vinje

Mathematical Modeling of Cerebrospinal Fluid Pulsatility and Pathways

Thesis submitted for the degree of Philosophiae Doctor

Department of Mathematics
The Faculty of Mathematics and Natural Sciences

Simula School of Research and Innovation



2019

© Vegard Vinje, 2019

*Series of dissertations submitted to the
The Faculty of Mathematics and Natural Sciences, University of Oslo
No. XXX*

ISSN XXX

All rights reserved. No part of this publication may be reproduced or transmitted, in any form or by any means, without permission.

Cover: Hanne Baadsgaard Utigard.
Print production: Reprosentralen, University of Oslo.

Preface

This thesis is submitted in partial fulfillment of the requirements for the degree of *Philosophiae Doctor* at the University of Oslo. The research presented here is conducted under the supervision of chief research scientist Marie E. Rognes, professor Kent-Andre Mardal and professor Yiannis Ventikos.

The thesis is a collection of four papers, presented in chronological order. The papers are preceded by an introduction that ties them together and provides background information and motivation for the work. All papers in this thesis are joint papers.

Acknowledgements

This thesis is the result of three fantastic years at Simula Research Laboratory. I am grateful for being part of such a dynamic and offensive organization, encouraging young researchers to take part in the international forefront of science.

First, I would like to thank my supervisors, Marie E. Rognes, Kent-Andre Mardal and Yiannis Ventikos. Marie, I appreciate the academic freedom you have given me through the years and your contribution to help me develop my scientific writing. Kent, we have had several discussions on the subject of cerebrospinal fluid dynamics, often lasting several hours. I am very grateful for your interest and passion for our work as well as your eagerness to help me develop my ideas. Yiannis, I want to thank you for having me in London for six months, providing me with an office space with one of the leading groups in cerebrospinal fluid flow modeling. In addition, I would like to thank all the co-authors contributing to the papers included in this thesis.

Next, my office mates Timo, Sebastian and especially Jørgen, which have provided moral support in tough times. We have had some great times both in and outside the office.

Finally, I would like to thank my family for unconditional support.

• **Vegard Vinje**
Oslo, August 2019

List of Papers

Paper 1

V. Vinje, J. Brucker, M.E. Rognes, K-A. Mardal and V. Haughton. ‘Fluid dynamics in syringomyelia cavities: Effects of heart rate, CSF velocity, CSF velocity waveform and craniovertebral decompression’. In: *The Neuroradiology Journal* **31** (2018), pp. 482–489. DOI: 10.1177/1971400918795482.

Paper 2

V. Vinje, G. Ringstad, E.K. Lindstrøm, L.M. Valnes, M.E. Rognes, P.K. Eide, K-A. Mardal ‘Respiratory influence on cerebrospinal fluid flow – a computational study based on long-term intracranial pressure measurements’. In: *Nature Scientific Reports* **9.1** (2019): 9732. DOI: 10.1038/s41598-019-46055-5

Paper 3

V. Vinje, M. Croci and M.E. Rognes ‘Uncertainty quantification of tracer distribution in the brain using random interstitial fluid velocity fields’. Submitted to *Fluids and Barriers of the CNS*.

Paper 4

V. Vinje, K.H. Støverud, M.E. Rognes, A. Eklund, K-A. Mardal ‘Intracranial pressure elevation alters CSF clearance pathways’. In preparation for submission.

List of Papers

The published papers are reprinted with permission from the publishers. All rights reserved.

Contents

1	Introduction	5
1.1	Motivation and aim	5
1.2	Anatomy of the central nervous system	7
1.2.1	The brain and the spinal cord	7
1.2.2	Cerebrospinal fluid	9
1.2.3	Chiari malformation and syringomyelia	10
1.2.4	Interstitial fluid	11
1.2.5	Para- and perivascular channels	12
1.3	Cerebrospinal fluid cycles	14
1.3.1	Steady CSF flow	15
1.3.2	The cardiac cycle	16
1.3.3	The respiratory cycle	17
1.3.4	The circadian rhythm	18
1.3.5	CSF cycles in this thesis	18
1.4	Mathematical modeling	19
1.4.1	Conservation of mass	20
1.4.2	Conservation of momentum	20
1.4.3	Conservation of tracer molecules	21
1.4.4	Linear elasticity	21
1.4.5	Fluid-structure interaction	22
1.4.6	Compartment models	23
1.4.7	Numerical methods	23
1.5	Summary of papers	24
1.5.1	Paper 1: Fluid dynamics in syringomyelia cavities: Effects of heart rate, CSF velocity, CSF velocity waveform and craniovertebral decompression	24
1.5.2	Paper 2: Respiratory influence on cerebrospinal fluid flow – a computational study based on long-term intracranial pressure measurements	25
1.5.3	Paper 3: Uncertainty quantification of parenchy- mal tracer distribution using random diffu- sion and convective velocity fields	26
1.5.4	Paper 4: Intracranial pressure elevation al- ters CSF clearance pathways	28

1.6	Limitations	29
1.7	An integrated view of the findings	30
1.8	Future work and outlook	31
2	Papers	43
	Paper 1: Fluid dynamics in syringomyelia cavities: Effects of heart rate, CSF velocity, CSF velocity waveform and craniovertebral decompression	45
	Paper 2: Respiratory influence on cerebrospinal fluid flow – a computational study based on long-term intracranial pressure measurements	61
	Paper 3: Uncertainty quantification of parenchymal tracer distribution using random diffusion and convective velocity fields	115
	Paper 4: Intracranial pressure elevation alters CSF clearance pathways	151

List of abbreviations

ALE arbitrary Lagrangian-Eulerian

A β amyloid-beta

CNS central nervous system

CSF cerebrospinal fluid

IPAD intramural periarterial drainage pathway

ISF interstitial fluid

PC-MRI phase-contrast magnetic resonance imaging

PVS paravascular space

SAS subarachnoid space

1 Introduction

1.1 Motivation and aim

Physiological background

Neurological disorders significantly reduce the life quality of patients and their families, and are one of the main burdens on the healthcare systems in the Western world. Only in the US, the annual cost to society of just nine of the most common forms of neurological disorders is \$789 billion a year [35]. These disorders include Alzheimer’s disease and other forms of dementia, spinal cord injury and Parkinson’s disease. As of 2017 there are 35 million dementia patients worldwide, with an estimated cost for care of \$ 600 billion per year [53]. Because the world’s population is aging, these disorders represent a fundamental challenge unless prevention of disease is possible.

Medical experiments involving the central nervous system has a high cost, and may also involve great risk for the patients. Even in the forefront of medical literature, results very often have to be extrapolated from other species to humans. As a supplement to medical experiments on animals, computer models may assist in progressing the knowledge of human physiology, both in health and disease. Current research efforts on the human brain have focused mainly on the biochemical or electrophysiological activity, despite the fact that also concepts from classical mechanics play an important role in modulating brain function [36].

The cerebrospinal fluid (CSF) is found in the subarachnoid spaces (SAS) surrounding the brain. CSF flow is regulated by pressure fluctuations in the SAS and plays a crucial role in maintaining the homeostasis of the central nervous system [54]. Many diseases in the central nervous system have been related to abnormal CSF flow [17, 74, 37], but the underlying causes are not agreed upon, and in some cases poorly understood. For instance, Alzheimer’s disease is characterized by accumulation of certain proteins known as amyloids in the brain [73]. Such waste products have been suggested to leave the brain through a convective flow of CSF. However, the mechanism of which the brain disposes of waste products is still up

for debate [20, 43].

Thesis aims

Therefore, the aim of this thesis is to **use concepts in classical mechanics to better understand the role of CSF in the central nervous system, both in health and disease.** In particular, the four studies included in this thesis all address different cycles of CSF flow, including the cardiac and respiratory cycle, the circadian rhythm and constant steady state flow.

More specifically, we aim to:

- Establish a relationship between pulsatile CSF flow in the SAS and pulsatile fluid flow within cavities within the the spinal cord (paper 1).
- Quantify the relative importance of different CSF cycles on pressure gradients and flow in the intracranial compartment (paper 2).
- Investigate clearance by diffusion versus convection in the brain (paper 3), and different routes of clearance of CSF from the SAS (paper 4).

Main findings

The main findings in this thesis can be summarized as follows

- Pulsatile flow in spinal cord cysts is initiated by pulsatile flow in the SAS and flow patterns may be altered after surgery (paper 1).
- Intracranial pressure gradients are dominated by the cardiac, rather than the respiratory, cycle. For flow patterns however, fluid velocity is evenly regulated by the two components, while the total volume over one cycle is greater for respiration (paper 2).
- Diffusion alone is not sufficient to explain transport of tracer into regions deep within the brain. Adding a physiologically

plausible convective fluid velocity field increases transport to these areas (paper 3).

- CSF outflow from the intracranial compartment occurs through many different routes of absorption. The relative importance of each outflow route is likely to be altered with changes in intracranial pressure.

Overview of the introduction

The remainder of the introduction is organized as follows. In Section 1.2, basic anatomy of the central nervous system (CNS) and the CSF is given. This section is mainly a summary of textbook knowledge, but also involves two newer concepts of waste clearance from the brain. In Section 1.3, different CSF cycles and their importance for CSF flow are discussed. At the end of Section 1.3, there is a short elaboration on how effects of different CSF cycles are relevant for this thesis. In Section 1.4, the mathematical models used in the papers are described in more detail. In Section 1.5, a summary of each paper is given, while Section 1.6 discuss the limitations, Section 1.7 provides an integrated view of the separate studies in the thesis. Finally Section 1.8 is a short note on future work and outlook.

1.2 Anatomy of the central nervous system

In this section, I will present the basic anatomy of the central nervous system. After the introduction of the brain and the spinal cord, the anatomy of the cerebrospinal fluid will be presented. I will go in more detail into different theories on CSF circulation, some of them which will be further discussed in Section 1.3. Unless otherwise stated, this section is based on the textbook "Human Anatomy and Physiology" [80].

1.2.1 The brain and the spinal cord

The central nervous system (CNS), shown on the left in Figure 1, consists of the brain and the spinal cord. The CNS is the processing

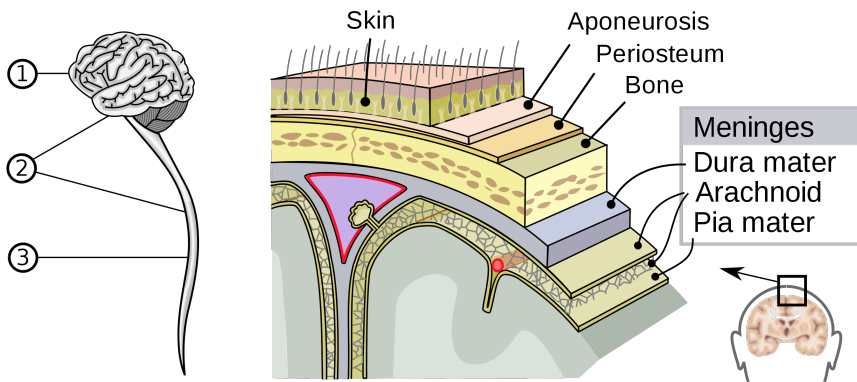


Figure 1: Left: The brain (1) and the spinal cord (3) comprise the central nervous system (2). The upper end of the spinal cord is continuous with the brainstem. Right: Anatomical figure of the meninges of the brain. Below the pia mater, the gray matter (in dark green/gray in the figure) is found, while beneath the gray matter the white matter is found. (Images from Wikimedia Commons [22])

point of signals sent from all parts of the body. The human CNS consumes about 20 % of the basal metabolism [56] and the brain itself receives 15 % of the cardiac output and 20 % of the total body oxygen consumption [75]. A fully functional CNS is thus important to maintain both physical and mental health. The CNS is divided into two types of tissue, white and gray matter. Gray matter contains neuronal cell bodies, neuropil, glial cells, synapses and capillaries. The white matter are mainly made up of myelinated axons, or tracts, connecting parts of gray matter to each other. Both tissues also contain some glial cells. In the brain, the gray matter surrounds the white matter. In the spinal cord, the gray matter is found inside the central cord, and is surrounded by the white matter.

Surrounding the CNS, there are three layers of protecting meninges. The innermost layer, the pia mater, is a thin layer tightly covering the CNS surface. The next protective layer is known as the arach-

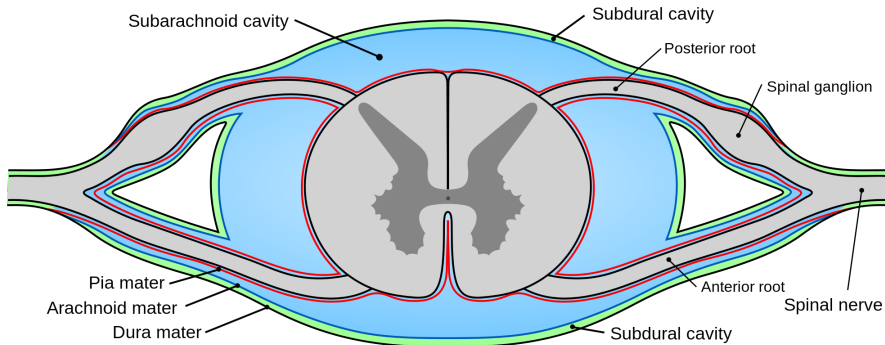


Figure 2: Anatomy of a cross-section of the spinal cord. (Image from Wikimedia Commons [22])

noid, while the outermost layer is called the dura mater, a thick layer composed of dense fibrous tissue. Between the pia mater and the arachnoid, there is a small space known as the subarachnoid space (SAS). In this space, the cerebrospinal fluid (CSF) acts as a protecting layer, for instance between the brain and the skull. The meninges, the SAS and the white and gray matter can be seen in Figure 1 (right) for the brain, and in Figure 2 for the spinal cord.

1.2.2 Cerebrospinal fluid

The CSF is a colorless fluid consisting mainly of water. In addition to buoyancy and protection of the brain [76], the CSF also plays an important role in maintaining homeostasis [54] and a stable cerebral blood flow [85]. In humans, there is approximately 140 mL of CSF, of which 30 mL are found in the ventricles, and 80 mL and 30 mL are found in the cerebral and spinal SAS respectively [16]. According to the textbook view, CSF is produced by the choroid plexus within the ventricles, flows through the narrow cerebral aqueduct, along the fourth ventricle passing through the lateral or median aperture, before reaching the SAS. From there, CSF may flow along the spinal cord, but eventually CSF flows to the intracranial SAS, and is drained at the arachnoid granulations, mainly into the superior sagittal sinus.

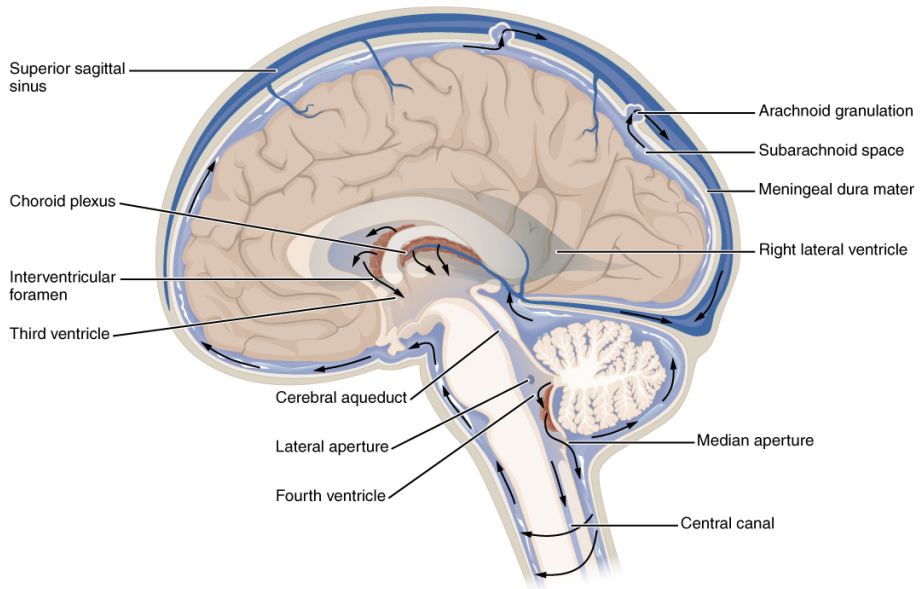


Figure 3: Circulation of the Cerebrospinal Fluid. (Image from Wikimedia Commons [22])

1.2.3 Chiari malformation and syringomyelia

The Chiari I malformation, or just Chiari malformation, is characterized by a downwards displacement of the cerebellar tonsils into the foramen magnum in the SAS.

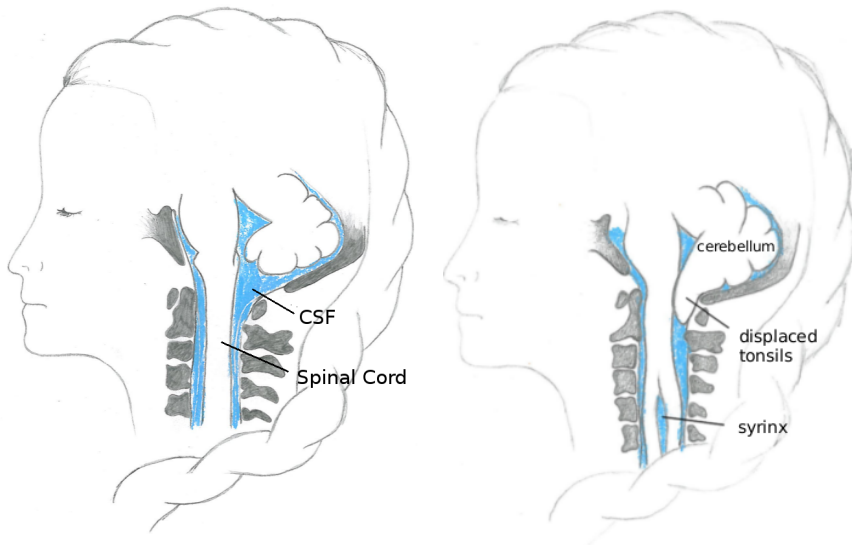


Figure 4: Illustrations of a healthy subject (left) and a subject with Chiari I malformation and syringomyelia (right). Illustrations by Synnøve S. Beitnes.

The cerebellum partially blocks the free flow of CSF between the SAS of the brain and the spinal cord. The Chiari malformation is frequently seen together with syringomyelia, a disease where a fluid filled space, or syrinx, develops within the spinal cord. Figure 4 shows a healthy subject with free CSF flow and an intact spinal cord, presented together with a subject with Chiari and syringomyelia. A number of theories have been proposed on the relationship between Chiari and syringomyelia, many of them related to abnormal CSF related to the obstruction of free flow at the foramen magnum seen in Chiari patients [37].

1.2.4 Interstitial fluid

The interstitial fluid (ISF) is the main component of the extracellular fluid, which is fluid found outside the cells in the body. In the brain, ISF is found in narrow gaps between cells [6]. Recent studies has demonstrated that CSF and ISF continuously inter-

change [54, 18].

1.2.5 Para- and perivascular channels

Peri- and paravascular channels are small fluid filled spaces surrounding blood vessels. Virchow [81] and Robin [67], identified what they called perivascular spaces already in the middle of the 19th century, but the understanding of these has been challenged and modified. Although para- and perivascular spaces may be anatomically distinct, the exact boundaries of the Virchow-Robin spaces are not clearly defined [6]. The perivascular spaces are have been referred to as the space within smooth muscle cells of arterioles and arteries. Paravascular spaces (PVS) are often used (also in this thesis) to denote the space outside the smooth muscle cells, outside the pia mater (or pial sheath), and enclosed within the basement membranes of glial limitans separating PVS from the brain parenchyma [6]. Whether the PVS are continuous with the SAS or have a surrounding membrane is not exactly clear. Iliff et al. [43] indicated a paravascular space, separated from the CSF in the SAS. However, Bedussi et al. [13] describe the SAS and the PVS as a single compartment with preferential pathways. In their view, PVS are simply regions in the SAS where resistance to flow is lower. More puzzling, in recent papers including researchers behind the glymphatic theory and paravascular inflow, Mestre et al. [55], Tithof et al. [79] and Ray et al. [63] have used the term perivascular space to describe these channels.

Regardless of their exact anatomical structures, fluid-filled spaces surrounding blood vessels have been suggested to play an important role in clearance of excess fluid and interstitial solutes. The mechanism of which waste clearance occurs from the brain has been a long-standing scientific question, as lymphatic vessels, the clearance system in the rest of the body, are absent in the brain parenchyma [1]. In the following I will describe two hypotheses of waste clearance, namely the glymphatic system, and the intramural periarterial drainage (IPAD) pathway. A short description of these pathways are given, while the possible drivers of flow will be discussed in Section 1.3.

The glymphatic system In 2012, Iliff et al. [43] described the glymphatic pathway for waste clearance from the brain. In their experiments, tracer injected into the cisterna magna in the SAS, rapidly entered the brain parenchyma. These observations were essentially a re-discovery of the pathways described by Rennels et al. [65], which found the CSF tracer horseradish peroxidase to rapidly enter the PVS of the brain. On a longer timescale, Cserr et al. [23] found evidence for bulk flow within the brain by injection of radiolabelled tracers of different molecular weight to the brain parenchyma in 1981. However, Iliff et al. [43] conceptualized these findings and put them into a complete theory for brain clearance. In this theory, CSF flows from the SAS, entering into the brain along the PVS. From the PVS, the CSF and brain ISF are coupled through low-resistant pathways known as astroglial AQP-4 channels [43]. By serving as a "lymphatic system" of the brain, and by the importance of the glial cells for fluid exchange between CSF and ISF, the system was named the glymphatic system [43, 45]. Inside the parenchyma, a bulk flow from arterioles to venules occurs before the fluid is drained out along paravenous spaces. Such a convective flow has the potential to remove waste from deeper inside the brain than diffusion alone.

The intramural periarterial drainage pathway In contrast to the glymphatic system, clearance along the IPAD pathway is in the reverse direction, out along the basement membranes of capillaries and arteries [20]. This pathway has been identified by the injection of fluorescent tracers into the brain [20, 57]. Morris et al. [57] also injected nanoparticles into mouse CSF in the SAS. Within 5 minutes after injection, nanoparticles were present along basement membranes on the outer aspects of cortical arteries, between the pia mater and the glia limitans, what has been referred to by others as *paravascular spaces* [34]. Nevertheless, experimental studies on para- and perivascular pathways suggest that these spaces play a crucial role in clearance of solute such as e.g. amyloid- β ($A\beta$), one of the proteins accumulating within the brain in Alzheimer's disease [45, 20, 84].

Old discussion revisited The debate regarding the exact pathways and mechanisms behind CSF clearance, whether it be according to the glymphatic system or the IPAD pathway has created renewed interest in the subject. On the other hand, the observation of two possibly distinct spaces surrounding cerebral blood vessels walls is not exactly new. One of the pioneers of medical studies in the early 20th century, Harvey Cushing discussed views of absorption and drainage of the CSF in *The Third Circulation and its channels* from 1925 [24]. While having difficulties in distinguishing fluid filled spaces around vessels as described by pathologist Feredrick W. Mott and anatomist E. E. Goldman he wrote:

It may be assumed that both pathologist and anatomist are talking of the same thing when the one mentions the perivascular spaces of Virchow [81] and of Robin [67] and the other the space of His [41]. However all three of these distinguished investigators originally gave such causal descriptions of the spaces in question that it is surprising that they should have become eponymic. Certainly the space which His disclosed by his injections must now be regarded as an artifact; and the view still maintained by many pathologists that the space of Robin is an adventitial lymph space within the wall of the blood vessel itself is surely erroneous even though it has crept into our anatomies.

– *Harvey Cushing, 1925*

1.3 Cerebrospinal fluid cycles

Movement of CSF in subarachnoid spaces (SAS) and within the cranium is regulated by several components ranging over many different time scales. In the traditional CSF hypothesis formulated by Harvey Cushing in 1925 [24], CSF is believed to flow in a unidirectional manner from the choroid plexuses to the arachnoid villi. The CSF production rate is normally around 500 mL/day [39]. Over the last 30 years however, cranial CSF flow has been possible to study noninvasively via phase-contrast magnetic resonance imaging (PC-MRI) techniques (e.g. [38, 33, 9, 26, 88, 50, 77]). These studies

have shown that pulsatile cardiac and respiratory effects dominate the small steady state flow predicted by the traditional hypothesis, and that CSF and cerebral blood flow are closely related.

1.3.1 Steady CSF flow

Studying CSF flow in the beginning of the 20th century did not allow for non-invasive measurements of CSF flow rate. Instead, sites of production and absorption was a topic of interest. Weed [83], Dandy [25] and Cushing [24] all pointed to the choroid plexus as the main site of production or "*the active spring whence the river of cerebrospinal fluid arises*" as Cushing phrased it. CSF would then flow down the cerebral aqueduct, into the SAS, out over the convexities of the brain, eventually reaching the arachnoid villi. In some medical textbooks, this notion of CSF circulation is more or less unchanged [39]. Variation of CSF flow over time was not addressed in the early studies, and the underlying assumption seemed to be the river-like steady flow as described by Cushing [24]. Choroid plexus secretion was assumed to be an active process, while the absorption at the arachnoid villi was assumed to be passive and driven by hydrostatic pressure differences.

More recently, the notion of a 500 mL/day production has been challenged by reports of net aqueductal flows of several liters a day [51]. However, these experiments have been questioned and in particular the ability of PC-MRI to measure large daily net flows calculated from a small net signal on the averaged cardiac cycle [7]. Another newer theory involving a more or less constant CSF production has been put forth and named the Bulat-Klarica-Orešković hypothesis [18]. According to this view, water is constantly filtered by capillaries and mixed with CSF. Similarly, capillaries absorb water from the CSF, such that production and absorption are in balance. In contrast to the traditional CSF hypothesis, the Bulat-Klarica-Orešković hypothesis states that CSF production and absorption are in balance within the ventricles [19].

1.3.2 The cardiac cycle

At rest, the cardiac cycle typically has a frequency at around 1 Hz. Blood is thus transported through the head in a pulsatile manner. Because the brain is contained within the rigid skull, the additional blood causes an increase in intracranial pressure (ICP) and a corresponding movement of CSF [82, 8]. At the initial phase of the cycle, arterial inflow exceeds the venous outflow, resulting in CSF flow from the SAS around the brain down along the spinal cord [10]. Following systole, a significant venous outflow occurs. Later, the aqueduct flow occurs caudally, followed by a transient equilibrium state and slow refilling of CSF to the cranium when venous outflow exceeds arterial inflow [10]. In addition to flow in the SAS, arterial pulsations have been claimed to be the main driver of flow into paravascular spaces (PVS) both in the brain [64, 44] and the spinal cord [15]. As already mentioned in Section 1.2.5, flow in PVS in the brain has been suggested to play a major role in waste clearance [45]. Although experimental studies in rodents have shown pulsatile flow entering PVS [12, 55] with a speed of approximately 20 $\mu\text{m}/\text{sec}$, modeling efforts have not been able to attribute this flow to arterial pulsations alone [5]. In terms of the IPAD pathway, flow in opposite direction of the blood flow have been proposed to occur along the reflection wave from the arterial pulsation [70].

Alterations in cardiac pulsatility of blood flow, and or CSF flow have been linked to disease progression in the brain and spinal cord. Hypertension has been shown to reduce flow into PVS in the brain, thus possibly reducing the clearance of $A\beta$ [55]. In the spinal cord, alterations in CSF flow due to Chiari malformation have been suggested to increase PVS flow into the spinal cord, a possible explanation of syrinx initiation and progression within the cord [52]. In particular, a change in the relative timing between blood and CSF pressure pulsations at the spinal level, has been proposed as a driver of additional CSF into PVS, possibly initiating a syrinx [15].

1.3.3 The respiratory cycle

In many of the earlier MRI-investigations [14, 33, 29, 49], CSF flow was measured with cardiac-gated MRI. With this technique, velocities are averaged over a range of cardiac cycles [8], while other cycles are lost in the averaging process [71]. For a long time, it was therefore not well known whether respiration affected CSF movement, and even less about its possible role in maintaining CNS function. In 1992, Schroth and Klose [72] found a respiratory component of oscillatory CSF pulsations in the cerebral aqueduct using real time MRI. Later, Klose et al. [48] detected a respiratory component of CSF flow with echoplanar MRI. With better technology and MRI-sequences, quantification of the respiratory-induced pulsations is now possible. Several studies have found the respiratory component of CSF flow to be of comparable size as the cardiac component [87]. Some studies have even concluded that respiration is the main driver of upwards CSF flow during inspiration [26], related to a simultaneous downwards flow of venous blood [27].

Even though investigators disagree on exactly how strong the influence of respiration is, the fact that respiration affects CSF flow seems clear. The role of respiration on CNS function is less clear. Respiratory movement of CSF has been directly related to venous flow and pressure [27, 47]. This suggests that respiration may also play a role in maintaining the counter pressure of blood flow from the arterial side, and thus acting as a regulator of cerebral blood flow. Similarly, respiration may be hypothesized to be an important regulator of the counter-pressure in the glymphatic circulation, under the assumption that efflux from the brain occurs along paravenous spaces [45].

Slow breathing has been used in practice for centuries with perceived health benefits [69] without knowledge of the exact underlying physiological mechanisms. Slow breathing increases oscillations in blood pressure and SAS width, and the increase is strictly dependent on the respiratory component [61]. At the same time, the cardiac component of the blood pressure and CSF pulse amplitude is diminished [61]. Elevated cardiac blood pressure amplitude may be sufficient to produce hypertrophy, even without an increase in

the mean arteriole pressure [11]. Increased cardiac blood flow pulsatility may also lead to cerebral small-vessel disease [40]. For this reason, a decrease in the cardiac pulsatility of these components, as seen during slow breathing, may be beneficial for cerebral circulation [61]. CSF dynamics, at least in the spine, varies depending on the respiratory performance [2], thus respiration represents a way to control CSF dynamics consciously.

1.3.4 The circadian rhythm

Circadian rhythms are endogenous oscillations with a period of approximately 24 hours [68]. Examples include the sleep-wake cycle, changes in body temperature and the number of dividing cells in tissue at a given point in time [3]. The circadian rhythm has been reported to affect several aspects of cerebral fluid dynamics and brain function. For instance, brain diffusivity has been shown to change over the course of a day [78], and is also affected by sleep deprivation [32]. Similar effects are seen on the brain functional connectome [46], and cerebral blood flow [31].

CSF production in the choroid plexus has been reported to display a strong circadian rhythm with an increase during nighttime [60, 59, 58]. Also, sleep has been suggested to have a restorative function due to increased clearance of degradation products [86]. Clearance in mice was equal in sleeping and anesthetized mice, suggesting it is sleep itself, and not the circadian rhythm, that switches the brain into a functional state that facilitates clearance [86]. In the sleeping or anesthetized state, clearance of $A\beta$ was twofold that of the awake state, suggesting that sleep plays an important role in brain function and possible prevention of neurodegenerative diseases.

1.3.5 CSF cycles in this thesis

In this thesis, all of the above time scales have been considered to a varying extent. In Paper 1 the focus is on cardiac oscillations in the spinal SAS related to syringomyelia in the spinal cord. In Paper 2, the effect of the cardiac versus respiratory component of aqueductal CSF flow is quantified. Also in Paper 2, pressure oscillations

are investigated in the sleep/wake cycle. In Paper 3, we consider clearance of solutes by diffusion and the glymphatic circulation in a steady manner. In Paper 4, a model of CSF clearance from the SAS in light of an infusion test is investigated to consider the plausibility of different (passive) outflow routes.

1.4 Mathematical modeling

This section presents the mathematical models used in this thesis. All models described in this section are based on the continuity equation which describes local conservation of a quantity.

In the following, assume Ω is a region, constant with respect to time. The famous scientist Osbourne Reynolds [66] stated:

Any change whatsoever in the quantity of any entity within a closed surface can only be effected in one or other of two distinct ways:

1. it may be effected by the production or destruction of the entity within the surface, or
2. by the passage of the entity across the surface.

In mathematical terms, this statement can be expressed as

$$\frac{d}{dt} \int_{\Omega} \phi(x, t) dx = \int_{\Omega} s(x, t) dx - \int_S q \cdot n dS. \quad (1)$$

Here, $\phi(x, t)$ is the quantity of interest, $q(x, t)$ is the flux of ϕ , $s(x, t)$ represents sources or sinks within the domain Ω , and the domains surface is denoted S . n is the outward pointing normal on S .

When Ω is constant with respect to time, the left hand side can be rewritten, and after rearrangement:

$$\int_{\Omega} \frac{\partial \phi(x, t)}{\partial t} + \nabla \cdot q(x, t) - s(x, t) dx = 0. \quad (2)$$

The closed surface Ω is arbitrary, thus the integrand has to be zero also locally. This yields the differential form of the continuity equation:

$$\frac{\partial \phi(x, t)}{\partial t} + \nabla \cdot q(x, t) - s(x, t) = 0. \quad (3)$$

For convective transport of a quantity $\phi(x, t)$ in a fluid, the flux is given by $q = \phi(x, t)v$, where $v = v(x, t)$ is the fluid velocity. Thus for a fluid, we can write

$$\frac{\partial \phi(x, t)}{\partial t} + \nabla \cdot (\phi(x, t)v) - s(x, t) = 0. \quad (4)$$

1.4.1 Conservation of mass

To derive an equation for conservation of mass in a fluid with velocity $v = v(x, t)$, insert $\phi(x, t) = \rho$ and $s(x, t) = 0$ in Equation (4). Here, ρ is a constant density of the quantity under consideration. The substitution results in

$$\frac{\partial \rho}{\partial t} + \nabla \cdot (\rho v) = \frac{\partial \rho}{\partial t} + \rho \nabla \cdot v + v \cdot \nabla \rho = \rho \nabla \cdot v = 0, \quad (5)$$

where the last step follows from the assumption that ρ is constant. Dividing by ρ we arrive at the mass conservation equation for incompressible flow

$$\nabla \cdot v = 0. \quad (6)$$

1.4.2 Conservation of momentum

Following the steps of the previous Section, insert $\phi(x, t) = \rho v(x, t)$ in Equation (4). Again, assuming ρ is constant, the substitution results in

$$\rho \frac{\partial v}{\partial t} + \nabla \cdot (\rho v v) = s(x, t). \quad (7)$$

Here vv denotes the dyadic product of $v = v(x, t)$ with itself. In a Newtonian fluid, forces $s(x, t)$ can be modeled by the stress tensor $\sigma(p, v) = -pI + 2\mu\varepsilon(v)$, where $\varepsilon(v) = \frac{1}{2}(\nabla v + \nabla v^T)$ and I is the identity tensor of the same spatial dimension as Ω . μ is the fluid viscosity, and $p = p(x, t)$ denotes the fluid pressure. Denoting other body forces (such as e.g. gravity) as f , the momentum equation for an incompressible fluid can thus be written in its familiar form:

$$\rho \left(\frac{\partial v}{\partial t} + v \cdot \nabla v \right) = -\nabla p + \mu \nabla^2 v + f. \quad (8)$$

Equations (6) and (8) together are often referred to as the Navier-Stokes equations, and are fundamental in fluid dynamics. These equations govern the flow of an incompressible fluid such as CSF.

1.4.3 Conservation of tracer molecules

The spread of tracers injected in the SAS or directly into the brain is often tracked to investigate the movement of CSF. To obtain a continuity equation for the conservation of molecules in a solution without convective motion, Fick's law of diffusion can be used:

$$J = -D\nabla c. \quad (9)$$

where $J = J(x, t)$ is the diffusion flux, $D = D(x)$ is the diffusion coefficient, and $c = c(x, t)$ denotes the concentration of molecules in a solution. If the solution also experiences convective flow, the convective transport can be denoted $F = vc$, where $v = v(x, t)$ is the fluid velocity. Inserting, $\phi(x, t) = c$, $q = J + F$ and $s(x, t) = 0$ in Equation (3) yields the diffusion-convection equation in an incompressible fluid

$$\frac{\partial c}{\partial t} + v \cdot \nabla c = \nabla \cdot (D\nabla c). \quad (10)$$

1.4.4 Linear elasticity

The linear elasticity equation is a statement of conservation of momentum, similar to Equation (8). The linear elasticity tensor, which describes stress-strain relations for an elastic material according to Hooke's law reads

$$\sigma_s(u) = \lambda \text{tr}(\epsilon(u))I + 2\mu\epsilon(u). \quad (11)$$

Here, $u = u(x, t)$ is the displacement field, λ and μ are material parameters known as Lamé parameters, I is the identity tensor, and $\epsilon(u) = \frac{1}{2}(\nabla u + \nabla u^T)$. By performing the similar steps as for momentum conservation for a fluid, but now assuming small deformations (i.e. nonlinear terms are small) we arrive at

$$\rho \frac{\partial^2 u}{\partial t^2} = \nabla \cdot \sigma_s + f. \quad (12)$$

1.4.5 Fluid-structure interaction

In all previous equations, the domain Ω was assumed constant with respect to time. However, many biological phenomena involve fluid in contact with a moving elastic material. Examples include pulsatile blood flow in contact with elastic vessel walls and CSF in contact with elastic tissue such as the CNS. Now consider a moving domain consisting of two distinct domains in contact with each other, one fluid domain and one solid domain $\Omega(t) = \Omega_f(t) \cup \Omega_s(t)$. The equations may be transformed the Arbitrary Lagrangian-Eulerian (ALE) formulation. By coupling Navier-Stokes equations (Equation (6) and (8)), with the linear elasticity equation (Equation (11)), the fluid-structure interaction problem reads [62, 28]:

$$\rho_f \left(\frac{\partial v}{\partial t} + (v - w) \cdot \nabla v \right) = \nabla \cdot \sigma_f(v, p) + f_f \quad \text{in } \Omega_f(t) \quad (13)$$

$$\nabla \cdot v = 0 \quad \text{in } \Omega_f(t) \quad (14)$$

$$\rho_s \frac{\partial^2 u}{\partial t^2} = \sigma_s(u) + f_s \quad \text{in } \Omega_s(t). \quad (15)$$

Here, $w = w(x, t)$ is the velocity of the domain, σ_s is the elastic stress tensor and σ_f is the fluid stress tensor. So far, initial and boundary conditions have not been addressed. Certain boundary conditions are needed in order to have a well posed problem, but in general boundary conditions are problem specific. However, in the fluid-structure interaction problem (Equations (13)-(15)), conservation of mass and momentum also needs to be specified on the interface $\Gamma(t)$ between them [62]. Thus on the boundary we also require

$$v = \frac{\partial u}{\partial t} \quad \text{on } \Gamma(t), \quad (16)$$

$$\sigma_f(p, v) \cdot n = \sigma_s(u) \cdot n \quad \text{on } \Gamma(t). \quad (17)$$

Here, n is the unit vector on the interface $\Gamma(t)$, and its direction is arbitrary as long as it is used consistently.

1.4.6 Compartment models

Compartment models for fluid pressure consider mass conservation in a given region or compartment, and assume a given relationship between the pressure and volume within the compartment. These models is often described by the ordinary differential equation [30]

$$C(p) \frac{dp}{dt} = Q_{\text{in}} - \frac{1}{R}(p - p_{\text{out}}). \quad (18)$$

Here, p denotes the pressure in the given compartment, Q_{in} represents fluid production or injection to the compartment, R is the resistance to outflow to a different compartment with pressure p_{out} . $C(p) = \frac{dV}{dp}$ is often referred to as the compliance of the compartment in consideration. Assuming an exponential relationship between pressure and volume, which is typically appropriate for intracranial models, the final model reads

$$\frac{1}{E(p - p_r)} \frac{dp}{dt} = Q_{\text{in}} - \frac{1}{R}(p - p_{\text{out}}). \quad (19)$$

Here, p_r is a constant reference pressure. For a thorough derivation of Equation (19), see e.g. Eisenträger & Sobey [30]. In Equation (19), pressure is modeled for one compartment with one outflow route only. However, these compartment models are easy to extend to include more outflow routes or additional compartments where pressure is modeled.

1.4.7 Numerical methods

To solve the mathematical models presented in this section numerically, different discretization schemes and numerical techniques can be used. The numerical methods used in this thesis are all standard finite difference and finite element methods (see e.g. [21]).

1.5 Summary of papers

1.5.1 Paper 1: Fluid dynamics in syringomyelia cavities: Effects of heart rate, CSF velocity, CSF velocity waveform and craniovertebral decompression

The displaced position of the cerebellum in Chiari I malformation partly blocks the normal flow of CSF between the cranium and the spinal cord. Many Chiari patients also develop syringomyelia, i.e. fluid-filled cavities within the spinal cord. To this date, many theories on the initiation and progression of a syrinx have been proposed, none of which have been fully accepted by the community. One of the theories includes rapid movement of fluid within the spinal cord, e.g. due to coughing tearing spinal cord tissue. In this paper we tested how pulsatile flow in the spinal SAS is related to pulsatile flow in a syrinx within the spinal cord under normal conditions.

To do so, we used a fluid-structure interaction model based on the equations described in Section 1.4.5. Data from a Chiari patient obtained before and after surgery was used as inlet boundary conditions for the fluid flow field in the SAS. We varied the inlet velocity and cycle rate in the SAS as well as the syrinx diameter.

The data from the MRI-analysis showed decreased velocities after surgery, both within the syrinx and in the SAS, and higher oscillatory frequency within the syrinx. Similarly, our model predicted decreased flow as a result of lower inlet boundary conditions. The decrease in syrinx peak velocity changed linearly with the velocity of the boundary condition in the SAS. Increased heart rate was also found to affect peak velocities in the syrinx, in particular a close to resonance frequency was found at 120 cycles per minute, increasing syrinx velocities with up to 300 %. In accordance with the MRI data, the syrinx fluid oscillatory frequency did not change with changes in frequency in the SAS. Syrinx diameter did not change syrinx velocity to the extent as the other parameters.

In conclusion, we found decreased SAS and syrinx velocities after surgery in a Chiari patient using MRI. In our model, we found a linear relationship between SAS and syrinx velocity, while cycle rate affected syrinx velocities in a nonlinear manner.

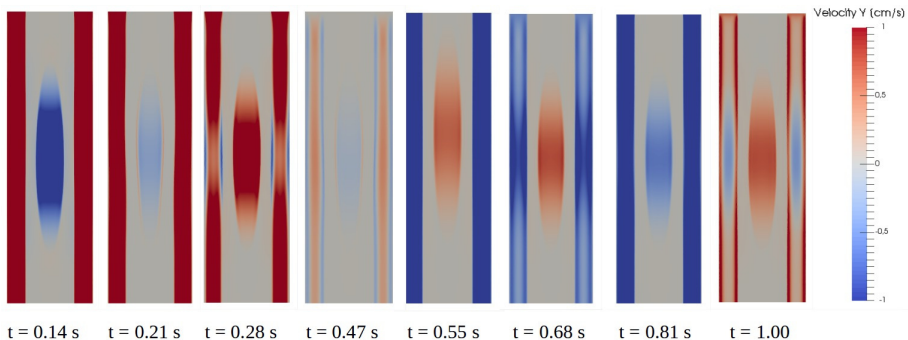


Figure 5: Spatial distribution of the flow pattern in the syrinx and the subarachnoid space at 8 different time points during a cardiac cycle of 1 second. Red color indicates caudal flow while blue indicates cranial flow. Cerebrospinal fluid flow in the SAS is pulsatile at a rate of 1 Hz, while the syrinx fluid oscillates four times faster.

1.5.2 Paper 2: Respiratory influence on cerebrospinal fluid flow – a computational study based on long-term intracranial pressure measurements

According to the glymphatic theory, solutes are cleared from the brain through convective CSF flow driven by arterial pulsations rather than respiratory effects. ICP measurements have also shown a dominance in the cardiac amplitude over the respiratory. On the other hand, several recent MRI studies have reported that respiration is a, if not *the* main driver of CSF flow. In this study, we aimed to compute CSF flow in one of the main conduits of the brain, the cerebral aqueduct.

Flow was computed by the Navier-Stokes equations (Equations (6) and (8)) with long-term intracranial pressure measurements from two separate locations in the intracranial space in 9 iNPH patients as driving forces. From the flow fields, we computed peak volumetric flow rate and total flow volumes over a cycle for both the cardiac and respiratory component. In all 9 patients, we used a simplified pressure gradient based on the Fourier spectrum of given 6-minute windows in a cylindrical geometry representing the aqueduct. In total 502 6-minute windows with approximately 182,000

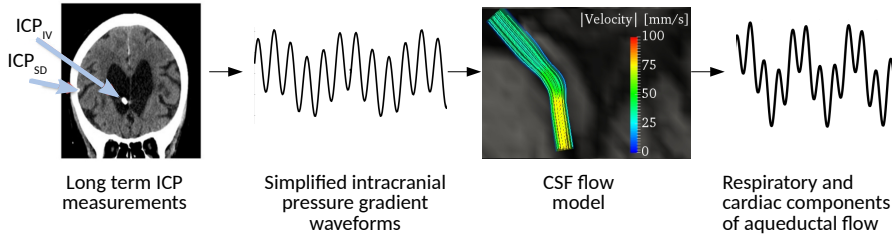


Figure 6: Conceptual figure representing the methodology in paper 2. Intracranial pressure measurements are used to calculate a simplified pressure gradient driving flow in a fluid dynamics model of the cerebral aqueduct.

cardiac and 48,000 respiratory cycles were analyzed. Patient-specific geometries were also used to ensure our that results were robust with respect to changes in the geometry.

On average, pulsatile pressure gradients in the brain was found to be 1.46 mmHg/m for the cardiac and 0.52 mmHg for the respiratory cycle. Peak volumetric flux was evenly regulated between the two components, with a factor 0.90 between the cardiac and respiratory peak volumetric flux. Volume of flow over one cycle was greater for the respiratory component due to its longer period, with a factor of 0.21 between the cardiac and respiratory volume.

In conclusion, we showed that small pulsatile respiratory gradients may induce flow at comparable magnitude as the larger cardiac gradient. Furthermore, respiration dominates the total flow volume over one respective cycle.

1.5.3 Paper 3: Uncertainty quantification of parenchymal tracer distribution using random diffusion and convective velocity fields

The relative importance of diffusion versus convection in clearing waste products from the brain is under debate. In the glymphatic theory, convective flow plays an important role, not only in paravascular spaces, but also in the brain interstitium. However, other experimental as well as modeling studies report diffusion to be the

main mechanism for transport in interstitial spaces. For modeling purposes, differences in the diffusion coefficient and velocity field (both magnitude and direction) determine the relative importance of diffusion versus convection. However, on a global scale, parameters are hard to measure, and not free from measurements errors. In this study we used uncertainty quantification to account for errors and uncertainties when modeling tracer distribution into the brain after intrathecal injection.

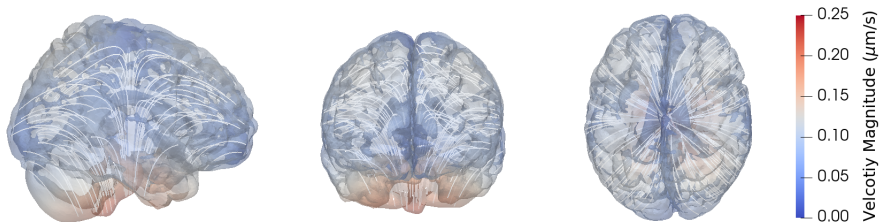


Figure 7: Illustration of one of the velocity fields considered in paper 3. The velocity field in this figure represents the directionality of the blood pulse propagation originating at the lower parts of the brain.

As a baseline model, we solved the convection-diffusion-reaction equation (Equation (10)) with an extra sink term) on a mesh of the human brain, and varied the diffusion coefficient and velocity field. The boundary condition was modeled based on tracer distribution in the SAS following intrathecal injection as seen on MRI-images from humans. Monte Carlo simulations were performed to quantify the total amount of tracer found in the gray and white matter.

With diffusion as the only mechanism of transport, assumed constant in space, variation in the diffusion constant within a factor 3 – 4 did not cause dramatic changes for the distribution to gray matter. For the white matter however, a variation of more than 100% was seen. A heterogeneous diffusion coefficient decreased the variability substantially, but in small regions, the same amount of variation was observed.

In our model, diffusion was not sufficient to explain transport into deep structures of the brain as seen on MRI. Adding a random velocity field representing the glymphatic system to the convection-diffusion equation did not increase transport unless the velocity field had a given net directionality to it.

1.5.4 Paper 4: Intracranial pressure elevation alters CSF clearance pathways

Pressure increases due to infusion of fluid to the SAS can be measured by an infusion test. Similarly, investigations into fluid flow in the brain have been performed by injection of tracers at volumes high enough to increase ICP. In this paper, we investigated whether a rise in ICP would affect the relative importance of different outflow routes from the SAS.

We considered a compartment model (extending Equation (19)) representing the pressure in the SAS and in the PVS. The CSF in the SAS was assumed to flow through the arachnoid granulations, the cribriform plate or into PVS. During a standard infusion test, we observed how pressure in the two compartments increased, and whether the flow distribution to different outflow pathways changed as a consequence of increased ICP. At baseline ICP, a relatively

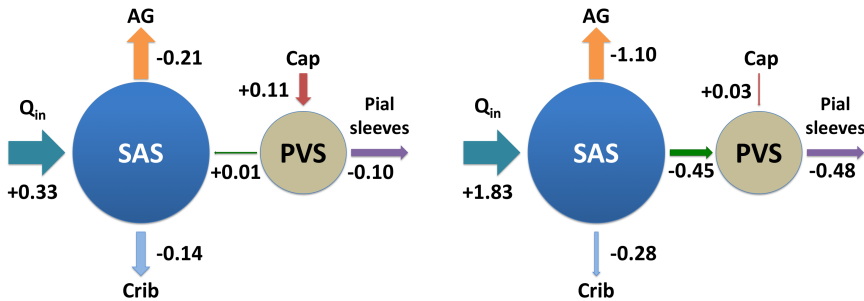


Figure 8: Outflow to each compartment considered when modelling the pressure in the SAS and PVS as unknowns. The flow rates (in mL/min) to each outflow route are given at baseline ICP (left) and plateau ICP (right). AG: arachnoid granulations, Cap: capillaries, Crib: cribriform plate, PVS: paravascular spaces.

stagnant flow was seen within the PVS, while 60% of the fluid left the SAS through the arachnoid granulations and 40% through the cribriform plate. At plateau ICP, flow into PVS increased drastically, with 25 % of the CSF entering these spaces.

In this paper, we found that the relative distribution to each outflow route was highly dependent on the ICP. The arachnoid granulations consistently dominated outflow, however reversal of PVS flow direction during an infusion test was seen. This observation might have implications for the validity of results obtained in tracer studies where high flow rates are used.

1.6 Limitations

Limitations are discussed in each paper, and this section considers some general limitations common for the papers in the thesis. There are many important mechanisms on the micro-level that we have ignored. For instance, the effect of osmotic gradients, electrophysiology and astrocyte networks connected by AQP-4 channels [4] have not been addressed in any of the mathematical models.

Modeling of paravascular spaces in this thesis were not performed at the level of a single paravascular space. Although it has already been shown that gradients induced by arterial pulsations are not sufficient to drive PVS flow in cylindrical geometries, a change in curvature, tapering, or splitting of the arterioles may affect this result.

In general, patient specific geometries were not considered, except the three aqueducts in paper 2. Patient specific geometries may provide insight in patient variability, but as we show in paper 2, is not the sole reason for differences in e.g. flow patterns. 3D patient specific geometries would definitely be preferred trying to draw conclusions affecting treatment related to paper 1. However, parameter exploration in 3D patient-specific two-way-coupling FSI simulations were found to be too time-demanding, both for time spent building the solver, and the simulation time it would require. In paper 2, the patients undergoing ICP monitoring were unfortunately not imaged at the resolution necessary to make meaningful geometries of the aqueduct. In all papers in this thesis, several pa-

rameters in each model were tested and varied. The use of patient specific geometries could be seen as an (expensive) expansion in the number of parameters.

Paper 3 and 4 both consider great variability in the constants or coefficients used in the model, and uncertainty quantification would be a possible approach in both cases. However, we found the model in paper 3 better suited for uncertainty quantification as the use of random fields can be employed in 3D. In addition, the baseline equation in paper 3 (diffusion-convection-reaction) was the same for all models, while in paper 4, we also experimented with expansion of the mathematical model and added different connections between compartments. Furthermore, post-processing after UQ to draw conclusions from the output would be difficult in paper 4 considering 9 models with 13 parameters for each model. Considering the fact that these 13 parameters are possibly dependent on each other, we decided to test some extreme and some plausible modifications of our model.

1.7 An integrated view of the findings

In this thesis, we focused on mechanical modeling of cerebrospinal fluid in the central nervous system. We have used concepts from classical mechanics and showed, in many different ways, how they impact the pulsatile nature of CSF dynamics.

Each individual paper in this thesis, provides information that could have been put to use by the other papers in the thesis as well. For instance, we were not aware to which extent respiration affects CSF flow (as found in paper 2), when studying pulsatile flow in the spinal SAS (paper 1). Similarly, in paper 3 we did not consider CSF clearance as quantitatively as in paper 4. In paper 3, better knowledge about the routes of CSF absorption might guides us in the direction of a better model for absorption at the capillary level. Furthermore, it would be possible to add intensity decay in the boundary condition determined by the tracer concentration in the SAS.

The velocity field in paper 3 was based on velocities found in the literature. However, in paper 4 we also performed several back-

of-the-envelope calculations investigating whether the pressure differences found in paper 2 were sufficient to drive glymphatic flow. In paper 4, the flow through paravascular spaces were on the order of 0.1 mL/min, corresponding to average velocities of a few $\mu\text{m/s}$. Inserting the average pulsatile cardiac pressure gradient from paper 2 (195 Pa/m), in the Poiseuille's equation for an annulus used in paper 4 might also provide information whether paravascular flow is plausible. At the level where the lumen radius is $23.5 \mu\text{m}$, flow velocities are found to be $16.16 \mu\text{m/s}$, exactly what has been found by Bedussi et al. [12] and Mestre et al. [55]. As we find in paper 4, the total resistance through the glymphatic system is much higher than in the paraarterial spaces themselves. Therefore pressure gradients of the magnitude found in paper 2 are not sufficient to drive flow through the glymphatic system at velocities previously reported [55, 12]. To this end, some of the models in paper 3 relies on the assumption that these flows exists despite the findings from paper 2. Findings from paper 4 suggests the flow fields used in paper 3 is possible, but most likely to occur during infusion tests or when the ICP is increased in the SAS.

1.8 Future work and outlook

Since the glymphatic theory was first proposed in 2012, mathematical modeling has added value to the discussion on cerebral clearance systems. The glymphatic theory consists of at least three important concepts: 1) Paravascular flow, 2) aqp-4 dependent entry to the parenchyma and 3) convective flow in the parenchyma. Concepts from mechanics have been used to cast doubt on both paravascular flow [5, 34] and bulk flow in the parenchyma[42]. Integrating the concepts from the glymphatic theory could be done for instance by coupling different models. As an example: paper 1 considers spinal SAS flow, paper 2 considers aqueductal flow, paper 3 considers parenchymal flow and concentration, while paper 4 models pressure and flow in the cerebral SAS and parenchyma. These processes are obviously connected and in theory modeled together.

In this thesis, we have amongst others pointed to respiration

(paper 2) and the infusion of tracer (paper 4) as possible factors affecting experimental results. Future studies investigating these questions amongst many others may determine whether the glymphatic system, or a slight modification of it, plays the major role of the lymphatic system in the brain.

References

- [1] N. J. Abbott. Evidence for bulk flow of brain interstitial fluid: significance for physiology and pathology. *Neurochemistry international*, 45(4):545–552, 2004.
- [2] G. Aktas, J. M. Kollmeier, A. A. Joseph, K.-D. Merboldt, H.-C. Ludwig, J. Gärtner, J. Frahm, and S. Dreha-Kulaczewski. Spinal CSF flow in response to forced thoracic and abdominal respiration. *Fluids and Barriers of the CNS*, 16(1):10, 2019.
- [3] J. Aschoff. Circadian rhythms in man. *Science*, 148(3676):1427–1432, 1965.
- [4] M. Asgari, D. De Zélicourt, and V. Kurtcuoglu. How astrocyte networks may contribute to cerebral metabolite clearance. *Scientific reports*, 5:15024, 2015.
- [5] M. Asgari, D. De Zélicourt, and V. Kurtcuoglu. Glymphatic solute transport does not require bulk flow. *Scientific reports*, 6:38635, 2016.
- [6] E. N. Bakker, B. J. Bacskai, M. Arbel-Ornath, R. Aldea, B. Bedussi, A. W. Morris, R. O. Weller, and R. O. Carare. Lymphatic clearance of the brain: perivascular, paravascular and significance for neurodegenerative diseases. *Cellular and molecular neurobiology*, 36(2):181–194, 2016.
- [7] O. Balédent, Z. Czosnyka, and M. Czosnyka. “Bucket” cerebrospinal fluid bulk flow—is it a fact or a fiction? *Acta neurochirurgica*, 161(2):257–258, 2019.

- [8] O. Balédent, L. Fin, L. Khuoy, K. Ambarki, A.-C. Gauvin, C. Gondry-Jouet, and M.-E. Meyer. Brain hydrodynamics study by phase-contrast magnetic resonance imaging and transcranial color doppler. *Journal of Magnetic Resonance Imaging: An Official Journal of the International Society for Magnetic Resonance in Medicine*, 24(5):995–1004, 2006.
- [9] O. Balédent, I. Idy-Peretti, et al. Cerebrospinal fluid dynamics and relation with blood flow: a magnetic resonance study with semiautomated cerebrospinal fluid segmentation. *Investigative radiology*, 36(7):368–377, 2001.
- [10] O. Balédent. *Imaging of the cerebrospinal fluid circulation*, chapter 12. Cambridge University Press, 2014.
- [11] G. L. Baumbach. Effects of increased pulse pressure on cerebral arterioles. *Hypertension*, 27(2):159–167, 1996.
- [12] B. Bedussi, M. Almasian, J. de Vos, E. VanBavel, and E. N. Bakker. Paravascular spaces at the brain surface: Low resistance pathways for cerebrospinal fluid flow. *Journal of Cerebral Blood Flow & Metabolism*, 38(4):719–726, 2018.
- [13] B. Bedussi, N. N. van der Wel, J. de Vos, H. van Veen, M. Siebes, E. VanBavel, and E. N. Bakker. Paravascular channels, cisterns, and the subarachnoid space in the rat brain: A single compartment with preferential pathways. *Journal of Cerebral Blood Flow & Metabolism*, 37(4):1374–1385, 2017.
- [14] G. Bergstrand, M. Bergström, B. Nordell, F. Ståhlberg, A. Ericsson, A. Hemmingsson, G. Sperber, K.-A. Thuomas, and B. Jung. Cardiac gated MR imaging of cerebrospinal fluid flow. *Journal of computer assisted tomography*, 9(6):1003–1006, 1985.
- [15] L. E. Bilston, M. A. Stoodley, and D. F. Fletcher. The influence of the relative timing of arterial and subarachnoid space pulse waves on spinal perivascular cerebrospinal fluid flow as a possible factor in syrinx development: Laboratory investigation. *Journal of neurosurgery*, 112(4):808–813, 2010.

- [16] R. Bozanovic-Sosic, R. Mollanji, and M. Johnston. Spinal and cranial contributions to total cerebrospinal fluid transport. *American Journal of Physiology-Regulatory, Integrative and Comparative Physiology*, 281(3):R909–R916, 2001.
- [17] W. Bradley. CSF flow in the brain in the context of normal pressure hydrocephalus. *American Journal of Neuroradiology*, 36(5):831–838, 2015.
- [18] M. Bulat and M. Klarica. Recent insights into a new hydrodynamics of the cerebrospinal fluid. *Brain research reviews*, 65(2):99–112, 2011.
- [19] M. Bulat, V. Lupret, D. Orešković, and M. Klarica. Transventricular and transpial absorption of cerebrospinal fluid into cerebral microvessels. *Collegium antropologicum*, 32(1):43–50, 2008.
- [20] R. Carare, M. Bernardes-Silva, T. Newman, A. Page, J. Nicoll, V. Perry, and R. Weller. Solutes, but not cells, drain from the brain parenchyma along basement membranes of capillaries and arteries: significance for cerebral amyloid angiopathy and neuroimmunology. *Neuropathology and applied neurobiology*, 34(2):131–144, 2008.
- [21] T. Chung. *Computational fluid dynamics*. Cambridge university press, 2010.
- [22] W. Commons. Main page. <http://commons.wikimedia.org>. Accessed: 2019-05-01.
- [23] H. Cserr, D. Cooper, P. Suri, and C. Patlak. Efflux of radiolabeled polyethylene glycols and albumin from rat brain. *American Journal of Physiology-Renal Physiology*, 240(4):F319–F328, 1981.
- [24] H. Cushing et al. The third circulation and its channels. *Lancet*, 2:851–857, 1925.
- [25] W. E. Dandy. Experimental hydrocephalus. *Annals of surgery*, 70(2):129, 1919.

- [26] S. Dreha-Kulaczewski, A. A. Joseph, K.-D. Merboldt, H.-C. Ludwig, J. Gärtner, and J. Frahm. Inspiration is the major regulator of human CSF flow. *Journal of Neuroscience*, 35(6):2485–2491, 2015.
- [27] S. Dreha-Kulaczewski, A. A. Joseph, K.-D. Merboldt, H.-C. Ludwig, J. Gärtner, and J. Frahm. Identification of the upward movement of human CSF in vivo and its relation to the brain venous system. *Journal of Neuroscience*, 37(9):2395–2402, 2017.
- [28] F. Duarte, R. Gormaz, and S. Natesan. Arbitrary Lagrangian–Eulerian method for Navier–Stokes equations with moving boundaries. *Computer Methods in Applied Mechanics and Engineering*, 193(45-47):4819–4836, 2004.
- [29] R. Edelman, V. Wedeen, K. Davis, D. Widder, P. Hahn, G. Shoukimas, and T. Brady. Multiphasic MR imaging: a new method for direct imaging of pulsatile CSF flow. *Radiology*, 161(3):779–783, 1986.
- [30] A. Eisenträger, I. Sobey, and M. Czosnyka. Parameter estimations for the cerebrospinal fluid infusion test. *Mathematical medicine and biology: a journal of the IMA*, 30(2):157–174, 2012.
- [31] T. Elvsåshagen, H. J. Mutsaerts, N. Zak, L. B. Norbom, S. H. Quraishi, P. Ø. Pedersen, U. F. Malt, L. T. Westlye, E. J. van Someren, A. Bjørnerud, et al. Cerebral blood flow changes after a day of wake, sleep, and sleep deprivation. *NeuroImage*, 186:497–509, 2019.
- [32] T. Elvsåshagen, L. B. Norbom, P. Ø. Pedersen, S. H. Quraishi, A. Bjørnerud, U. F. Malt, I. R. Groote, and L. T. Westlye. Widespread changes in white matter microstructure after a day of waking and sleep deprivation. *PLoS One*, 10(5):e0127351, 2015.

- [33] D. Enzmann and N. Pelc. Normal flow patterns of intracranial and spinal cerebrospinal fluid defined with phase-contrast cine MR imaging. *Radiology*, 178(2):467–474, 1991.
- [34] M. M. Faghih and M. K. Sharp. Is bulk flow plausible in perivascular, paravascular and paravenous channels? *Fluids and Barriers of the CNS*, 15(1):17, 2018.
- [35] C. L. Gooch, E. Pracht, and A. R. Borenstein. The burden of neurological disease in the united states: a summary report and call to action. *Annals of neurology*, 81(4):479–484, 2017.
- [36] A. Goriely, M. G. Geers, G. A. Holzapfel, J. Jayamohan, A. Jérusalem, S. Sivaloganathan, W. Squier, J. A. van Dommelen, S. Waters, and E. Kuhl. Mechanics of the brain: perspectives, challenges, and opportunities. *Biomechanics and modeling in mechanobiology*, 14(5):931–965, 2015.
- [37] D. Greitz. Unraveling the riddle of syringomyelia. *Neurosurgical review*, 29(4):251–264, 2006.
- [38] D. Greitz, A. Franck, and B. Nordell. On the pulsatile nature of intracranial and spinal CSF-circulation demonstrated by MR imaging. *Acta radiologica*, 34(4):321–328, 1993.
- [39] A. C. Guyton and J. E. Hall. Textbook of medical physiology. 11th. *WB Saunders Company, Philadelphia*, 2006.
- [40] L. H. Henskens, A. A. Kroon, R. J. Van Oostenbrugge, E. H. Gronenschild, M. M. Fuss-Lejeune, P. A. Hofman, J. Lodder, and P. W. De Leeuw. Increased aortic pulse wave velocity is associated with silent cerebral small-vessel disease in hypertensive patients. *Hypertension*, 52(6):1120–1126, 2008.
- [41] W. His. *Über ein perivascularäres Canalsystem in den nervösen Centralorganen und über dessen Beziehungen zum Lymphsystem: Mit einer in Farben gedruckten Tafel.* W. Engelmann, 1865.

- [42] K. E. Holter, B. Kehlet, A. Devor, T. J. Sejnowski, A. M. Dale, S. W. Omholt, O. P. Ottersen, E. A. Nagelhus, K.-A. Mardal, and K. H. Pettersen. Interstitial solute transport in 3d reconstructed neuropil occurs by diffusion rather than bulk flow. *Proceedings of the National Academy of Sciences*, page 201706942, 2017.
- [43] J. J. Iliff, M. Wang, Y. Liao, B. A. Plogg, W. Peng, G. A. Gundersen, H. Benveniste, G. E. Vates, R. Deane, S. A. Goldman, et al. A paravascular pathway facilitates CSF flow through the brain parenchyma and the clearance of interstitial solutes, including amyloid β . *Science translational medicine*, 4(147):147ra111–147ra111, 2012.
- [44] J. J. Iliff, M. Wang, D. M. Zeppenfeld, A. Venkataraman, B. A. Plog, Y. Liao, R. Deane, and M. Nedergaard. Cerebral arterial pulsation drives paravascular CSF–interstitial fluid exchange in the murine brain. *Journal of Neuroscience*, 33(46):18190–18199, 2013.
- [45] N. A. Jessen, A. S. F. Munk, I. Lundgaard, and M. Nedergaard. The glymphatic system: a beginner’s guide. *Neurochemical research*, 40(12):2583–2599, 2015.
- [46] T. Kaufmann, T. Elvsåshagen, D. Alnæs, N. Zak, P. Ø. Pedersen, L. B. Norbom, S. H. Quraishi, E. Tagliazucchi, H. Laufs, A. Bjørnerud, et al. The brain functional connectome is robustly altered by lack of sleep. *Neuroimage*, 127:324–332, 2016.
- [47] V. Kiviniemi, X. Wang, V. Korhonen, T. Keinänen, T. Tuovinen, J. Autio, P. LeVan, S. Keilholz, Y.-F. Zang, J. Hennig, et al. Ultra-fast magnetic resonance encephalography of physiological brain activity–glymphatic pulsation mechanisms? *Journal of Cerebral Blood Flow & Metabolism*, 36(6):1033–1045, 2016.
- [48] U. Klose, C. Strik, C. Kiefer, and W. Grodd. Detection of a relation between respiration and CSF pulsation with an echo-planar technique. *Journal of Magnetic Resonance Imaging*, 11(4):438–444, 2000.

- [49] L. Levy and G. Di Chiro. MR phase imaging and cerebrospinal fluid flow in the head and spine. *Neuroradiology*, 32(5):399–406, 1990.
- [50] E. K. Lindstrøm, G. Ringstad, K.-A. Mardal, and P. K. Eide. Cerebrospinal fluid volumetric net flow rate and direction in idiopathic normal pressure hydrocephalus. *NeuroImage: Clinical*, 20:731–741, 2018.
- [51] E. K. Lindstrøm, G. Ringstad, A. Sorteberg, W. Sorteberg, K.-A. Mardal, and P. K. Eide. Magnitude and direction of aqueductal cerebrospinal fluid flow: large variations in patients with intracranial aneurysms with or without a previous subarachnoid hemorrhage. *Acta neurochirurgica*, 161(2):247–256, 2019.
- [52] R. A. Lloyd, D. F. Fletcher, E. C. Clarke, and L. E. Bilston. Chiari malformation may increase perivascular cerebrospinal fluid flow into the spinal cord: A subject-specific computational modelling study. *Journal of biomechanics*, 65:185–193, 2017.
- [53] P. Maresova, H. Mohelska, J. Dolejs, and K. Kuca. Socio-economic aspects of Alzheimer’s disease. *Current Alzheimer Research*, 12(9):903–911, 2015.
- [54] M. Matsumae, O. Sato, A. Hirayama, N. Hayashi, K. Takizawa, H. Atsumi, and T. Sorimachi. Research into the physiology of cerebrospinal fluid reaches a new horizon: intimate exchange between cerebrospinal fluid and interstitial fluid may contribute to maintenance of homeostasis in the central nervous system. *Neurologia medico-chirurgica*, 56(7):416–441, 2016.
- [55] H. Mestre, J. Tithof, T. Du, W. Song, W. Peng, A. M. Sweeney, G. Olveda, J. H. Thomas, M. Nedergaard, and D. H. Kelley. Flow of cerebrospinal fluid is driven by arterial pulsations and is reduced in hypertension. *Nature communications*, 9(1):4878, 2018.

- [56] J. W. Mink, R. J. Blumenshine, and D. B. Adams. Ratio of central nervous system to body metabolism in vertebrates: its constancy and functional basis. *American Journal of Physiology-Regulatory, Integrative and Comparative Physiology*, 241(3):R203–R212, 1981.
- [57] A. W. Morris, M. M. Sharp, N. J. Albargothy, R. Fernandes, C. A. Hawkes, A. Verma, R. O. Weller, and R. O. Carare. Vascular basement membranes as pathways for the passage of fluid into and out of the brain. *Acta neuropathologica*, 131(5):725–736, 2016.
- [58] J. Myung, C. Schmal, S. Hong, Y. Tsukizawa, P. Rose, Y. Zhang, M. J. Holtzman, E. De Schutter, H. Herzog, G. Borodyugov, et al. The choroid plexus is an important circadian clock component. *Nature communications*, 9(1):1062, 2018.
- [59] J. Myung, D. Wu, V. Simonneaux, and T. J. Lane. Strong circadian rhythms in the choroid plexus: implications for sleep-independent brain metabolite clearance. *Journal of experimental neuroscience*, 12:1179069518783762, 2018.
- [60] C. Nilsson, F. Stahlberg, C. Thomsen, O. Henriksen, M. Herning, and C. Owman. Circadian variation in human cerebrospinal fluid production measured by magnetic resonance imaging. *American Journal of Physiology-Regulatory, Integrative and Comparative Physiology*, 262(1):R20–R24, 1992.
- [61] M. K. Nuckowska, M. Gruszecki, J. Kot, J. Wolf, W. Guminski, A. F. Frydrychowski, J. Wtorek, K. Narkiewicz, and P. J. Winklewski. Impact of slow breathing on the blood pressure and subarachnoid space width oscillations in humans. *Scientific reports*, 9(1):6232, 2019.
- [62] A. Quaini. Algorithms for fluid-structure interaction problems arising in hemodynamics. Technical report, EPFL, 2009.
- [63] L. Ray, J. J. Iliff, and J. J. Heys. Analysis of convective and diffusive transport in the brain interstitium. *Fluids and Barriers of the CNS*, 16(1):6, 2019.

- [64] M. Rennels, O. Blaumanis, and P. Grady. Rapid solute transport throughout the brain via paravascular fluid pathways. *Advances in neurology*, 52:431–439, 1989.
- [65] M. L. Rennels, T. F. Gregory, O. R. Blaumanis, K. Fujimoto, and P. A. Grady. Evidence for a ‘paravascular’ fluid circulation in the mammalian central nervous system, provided by the rapid distribution of tracer protein throughout the brain from the subarachnoid space. *Brain research*, 326(1):47–63, 1985.
- [66] O. Reynolds. *Papers on Mechanical and Physical Subjects, The Sub-Mechanics of the Universe*, volume 3. Cambridge University Press, Cambridge, 1903.
- [67] C. Robin. Recherches sur quelques particularites de la structure des capillaires de l’encephale. *J. Physiol. Homme. Anim.*, 2:537–548, 1859.
- [68] B. Rusak and I. Zucker. Neural regulation of circadian rhythms. *Physiological reviews*, 59(3):449–526, 1979.
- [69] M. A. Russo, D. M. Santarelli, and D. O’Rourke. The physiological effects of slow breathing in the healthy human. *Breathe*, 13(4):298–309, 2017.
- [70] D. Schley, R. Carare-Nnadi, C. Please, V. Perry, and R. Weller. Mechanisms to explain the reverse perivascular transport of solutes out of the brain. *Journal of theoretical biology*, 238(4):962–974, 2006.
- [71] G. Schroth and U. Klose. Cerebrospinal fluid flow. *Neuroradiology*, 35(1):1–9, 1992.
- [72] G. Schroth and U. Klose. Cerebrospinal fluid flow. II. Physiology of respiration-related pulsations. *Neuroradiology*, 35(1):10–15, 1992.
- [73] Y. Shinkai, M. Yoshimura, Y. Ito, A. Odaka, N. Suzuki, K. Yanagisawa, and Y. Ihara. Amyloid β -proteins 1–40 and 1–42 (43) in the soluble fraction of extra- and intracranial blood vessels. *Annals of neurology*, 38(3):421–428, 1995.

- [74] M. J. Simon and J. J. Iliff. Regulation of cerebrospinal fluid (CSF) flow in neurodegenerative, neurovascular and neuroinflammatory disease. *Biochimica et Biophysica Acta (BBA)-Molecular Basis of Disease*, 1862(3):442–451, 2016.
- [75] L. Sokoloff. Circulation and energy metabolism of the brain. *Basic neurochemistry*, 2:338–413, 1989.
- [76] R. Spector, S. R. Snodgrass, and C. E. Johanson. A balanced view of the cerebrospinal fluid composition and functions: focus on adult humans. *Experimental neurology*, 273:57–68, 2015.
- [77] J. M. Spijkerman, L. J. Geurts, J. C. Siero, J. Hendrikse, P. R. Luijten, and J. J. Zwanenburg. Phase contrast MRI measurements of net cerebrospinal fluid flow through the cerebral aqueduct are confounded by respiration. *Journal of Magnetic Resonance Imaging*, 2018.
- [78] C. Thomas, N. Sadeghi, A. Nayak, A. Treffer, J. Sarlls, C. I. Baker, and C. Pierpaoli. Impact of time-of-day on diffusivity measures of brain tissue derived from diffusion tensor imaging. *Neuroimage*, 173:25–34, 2018.
- [79] J. Tithof, D. H. Kelley, H. Mestre, M. Nedergaard, and J. H. Thomas. Hydraulic resistance of perivascular spaces in the brain. *bioRxiv*, page 522409, 2019.
- [80] D. Van WYnsberghe, C. R. Noback, and R. Carola. *Human anatomy and physiology*. McGraw-Hill College, 1995.
- [81] R. Virchow. Ueber die erweiterung kleinerer gefäße. *Virchows Archiv*, 3(3):427–462, 1851.
- [82] M. E. Wagshul, P. K. Eide, and J. R. Madsen. The pulsating brain: a review of experimental and clinical studies of intracranial pulsatility. *Fluids and Barriers of the CNS*, 8(1):5, 2011.
- [83] L. Weed. Studies on cerebro-spinal fluid. No. IV: the dual source of CSF. *J Med Res*, 26:93–118, 1914.

- [84] R. Weller, M. Subash, S. Preston, I. Mazanti, and R. Carare. Perivascular drainage of amyloid- β peptides from the brain and its failure in cerebral amyloid angiopathy and Alzheimer's disease. *Brain pathology*, 18(2):253–266, 2008.
- [85] B. L. Wright, J. T. Lai, and A. J. Sinclair. Cerebrospinal fluid and lumbar puncture: a practical review. *Journal of neurology*, 259(8):1530–1545, 2012.
- [86] L. Xie, H. Kang, Q. Xu, M. J. Chen, Y. Liao, M. Thiyagarajan, J. O'Donnell, D. J. Christensen, C. Nicholson, J. J. Iliff, et al. Sleep drives metabolite clearance from the adult brain. *science*, 342(6156):373–377, 2013.
- [87] S. Yamada, M. Miyazaki, Y. Yamashita, C. Ouyang, M. Yui, M. Nakahashi, S. Shimizu, I. Aoki, Y. Morohoshi, and J. G. McComb. Influence of respiration on cerebrospinal fluid movement using magnetic resonance spin labeling. *Fluids and barriers of the CNS*, 10(1):36, 2013.
- [88] S. Yildiz, S. Thyagaraj, N. Jin, X. Zhong, S. Heidari Pahlavian, B. A. Martin, F. Loth, J. Oshinski, and K. G. Sabra. Quantifying the influence of respiration and cardiac pulsations on cerebrospinal fluid dynamics using real-time phase-contrast MRI. *Journal of Magnetic Resonance Imaging*, 46(2):431–439, 2017.

2 Papers

Paper 1

Fluid dynamics in syringomyelia cavities: Effects of heart rate, CSF velocity, CSF velocity waveform and craniovertebral decompression

Fluid dynamics in syringomyelia cavities: Effects of heart rate, CSF velocity, CSF velocity waveform and craniovertebral decompression

V Vinje^{1,*}, J Brucker², ME Rognes¹, KA Mardal^{1,3}, and Victor Haughton²

¹Simula Research Laboratory, Norway.

²Department of Radiology, University of Wisconsin, USA

³Department of Mathematics, University of Oslo, Norway

*vegard@simula.no

August 2018

Abstract

Purpose: How fluid moves during the cardiac cycle within a syrinx may affect its development. We measured syrinx fluid velocities before and after craniovertebral decompression in a patient and simulated syrinx fluid velocities for different heart rates, syrinx sizes and cerebrospinal fluid (CSF) flow velocities in a model of syringomyelia.

Materials and methods: With phase-contrast magnetic resonance we measured CSF and syrinx fluid velocities in a Chiari patient before and after craniovertebral decompression. With an idealized two-dimensional model of the subarachnoid space (SAS), cord and syrinx, we simulated fluid movement in the SAS and syrinx with the Navier-Stokes equations for different heart rates, inlet velocities and syrinx diameters.

Results: In the patient, fluid oscillated in the syrinx at 200 to 210 cycles per minute before and after craniovertebral decompression. Velocities peaked at 3.6 and 2.0 cm per second respectively in the SAS and the syrinx before surgery and at 2.7 and 1.5 cm per second after surgery. In the model, syrinx velocity varied between 0.91 and 12.70 cm per second. Increasing CSF inlet velocities from 1.56 to 4.69 cm per second increased peak syrinx fluid velocities in the syrinx by 151% to 299% for the three cycle rates. Increasing cycle rates from 60 to 120 cpm increased peak syrinx velocities by 160% to 312% for the three inlet velocities. Peak velocities changed inconsistently with syrinx size.

Conclusions: CSF velocity, heart rate and syrinx diameter affect syrinx fluid velocities, but not the frequency of syrinx fluid oscillation. Craniovertebral decompression decreases both CSF and syrinx fluid velocities.

Introduction

Fluid within syringomyelia cavities moves during the cardiac cycle. Dynamic MR imaging in a patient with Chiari I and syringomyelia showed cranial and caudal fluid jets in syrinx fluid related to the cardiac cycle [3]. Phase Contrast MR (PC MR) in patients with Chiari I and syringomyelia have shown a spatially and temporally complex pattern of fluid movement in the syrinx [10]. Craniovertebral decompression altered flow in a Chiari I patient both in the subarachnoid space (SAS) and in the syrinx, and decreased syrinx velocities by an order of magnitude [4]. In vitro flow experiments in physical models of syringomyelia have revealed pulsatile pressure and flow within the syrinx during cardiac cycles [7]. Computational studies have demonstrated syrinx fluid motion close to 1 cm/sec initiated by pulse waves traveling along the spinal cord related to coughing, a velocity too small to generate sufficient force to lengthen a syrinx [1]. It was suggested that greater syrinx velocities may cause tearing of spinal cord tissue. The movement of syrinx fluid vis-a-vis CSF movement in the subarachnoid space (SAS) has yet to be thoroughly evaluated.

The goal of this study was to determine the range of syrinx fluid velocities for a set of physiological conditions. We obtained MR flow images of the CSF and syrinx fluid in a patient with syringomyelia and compared SAS and syrinx fluid dynamics before and after craniovertebral decompression. We simulated syrinx fluid movement in a computational model to study syrinx and CSF velocities. In the model, we measured the effects of CSF velocity waveform, CSF velocity, heart rate and syrinx size on the movement of syrinx fluid.

Materials and methods

In-vivo fluid velocity measurements



Figure 1: T2-weighted sagittal magnetic resonance images prior to (left) and at two months (middle) and 10 months (right) after craniovertebral decompression. Preoperatively, a syrinx 7 mm in diameter expands the cervical spinal cord from C1 to C6. The syrinx resolved partially by two months and completely by 10 months.

This study was performed with the approval of the local institutional review board, which granted a waiver of consent for the retrospective use of imaging data acquired as part of the clinical evaluations for diagnosis of Chiari I malformation. The serial anatomical MR and PC-flow imaging data of a 14 year old female with a Chiari I malformation and syringomyelia obtained between 2013 and 2014 was selected for retrospective review, which included time-points before and after craniovertebral decompression; serial imaging had demonstrated resolution of the patient's symptoms and syringomyelia following postsurgical decompression (Figure 1).

Imaging was performed on a 3 Tesla wide-bore MRI scanner (Discovery 750w; General Electric Healthcare, Waukesha, WI, USA) with an 8-channel head coil. Per our institutions standard clinical protocol for spinal CSF-flow imaging, peripherally gated multilevel axial 2-D phase-contrast imaging was performed perpendicular to the long axis of the cervical spinal canal at the C1-C2, C2, C2-C3, C3, C3-C4, and C4-C5 spinal levels (flip angle = 20 degrees; TR = 6.74 ms; TE = 3.8 ms; slice thickness = 5 mm; field of view (FOV) = 180 mm; matrix = 256 x 256; velocity encoding gradient (VEnc) = 20 cm/sec; 14 cardiac phases; 10% arrhythmia rejection rate). Other standard anatomical imaging of the cervical spine includes; Sagittal and axial T1 Fluid attenuated inversion recovery (T1 FLAIR) weighted spin echo imaging (flip angle = 142 degrees; TR = 2432.1 ms; TE = 24.9 ms; TI = 920 ms; echo train length = 4; slice thickness = 4mm; FOV = 220 mm; matrix = 512 x 512; NEX = 1), sagittal T2-weighted fast spin echo imaging (flip angle = 142 degrees; TR = 3600 ms; TE = 109.9 ms; TI = 920 ms; echo train length = 24; slice thickness = 4mm; FOV = 220 mm; matrix = 512 x 512; NEX = 2), and axial T2* MERGE (flip angle = 25 degrees; TR = 1000 ms; TE = 12.2 ms; TI = 920 ms; echo train length = 4; slice thickness = 4mm; FOV = 200 mm; matrix = 512 x 512; NEX = 2).

Multilevel axial PC-flow data was calculated with the CV Flow Analysis software package (General Electric Healthcare; Waukesha, WI, USA). At each cervical spinal level, axial CSF flow velocities were sampled with elliptical ROIs drawn in twelve clockface sectors that subdivided the subarachnoid space around the cervical cord, with the 12 o'clock location being the anterior side. This segmentation was performed in order to account for topographic variations in CSF flow around the cord, to avoid including structures traversing the CSF space that might interfere with accurate measure of peak velocities (e.g. nerve rootlets, blood vessels, cord margins), and to avoid low-flow boundary phenomena around the margins of the SAS and cord. An additional ROI was also drawn within the center of the syrinx; for the syrinx flow measurements, the hand-drawn ROI covered the main part of the syrinx cavity and excluded the low flow boundary regions of the syrinx. Velocities within each ROI were then extracted and normalized to their respective sampling areas, prior to being plotted over the cardiac cycle. To compare the MR results to the 2D-model we focused on one ROI at each horizontal level of the cervical spine, all at the 1 o'clock location in the cross-section of the SAS, and computed the weighted average of the velocity in these ROIs.

Flow simulations

For flow simulations, we used a 2D computational model of the subarachnoid space, 6 cm in length and 1.8 cm in width (Figure 2), permitting flow measurements with greater spatial resolution (submillimeter all directions) and temporal resolution (millisecond) than in the PC MR images. Fluid in the model was assigned the properties of water at 37 degrees centigrade. Centrally in the spinal cord in the model we inserted a rectangle 6 cm in length and 1 cm in width to

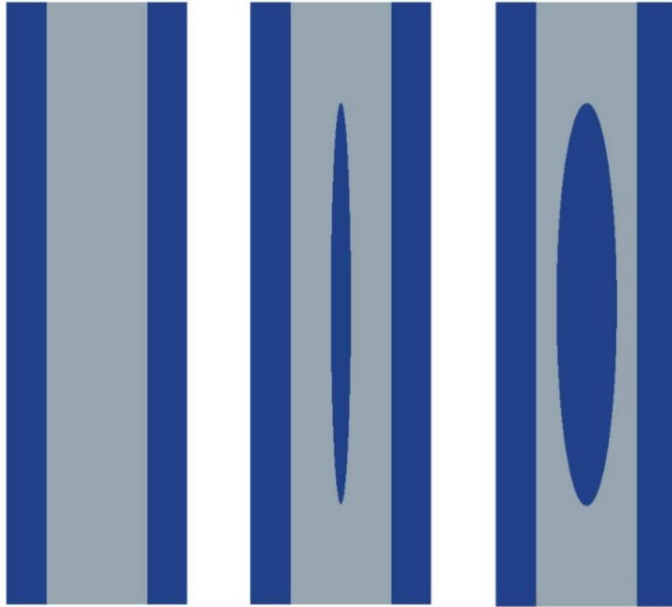


Figure 2: Sketches showing the model with no syrinx (left) and the two modifications of the model with a 2 mm (middle) or 6 mm (right) elliptical fluid-filled space (syrinx). Blue areas represent fluid; gray areas represent spinal cord tissue.

represent the spinal cord and assigned it linearly elastic properties of the spinal cord (Young's modulus of 16 kPa [9] and Poisson's ratio of 0.479 [12]). We created two modifications of the model, one with an elliptical central water-filled space 4 cm in length and 2 mm in peak diameter and another with an elliptical space 4 cm in length and 6 mm in peak diameter.

At the outer boundaries of the CSF and syrinx fluid spaces, we applied no slip conditions. At the interfaces between the fluid and the tissue, we assumed continuity of stresses and velocities. The top and bottom of the cord were assumed to be fixed. We applied flow at one end of the subarachnoid space, designated the cranial end, by specifying a flow condition varying in time, while a zero pressure condition was applied to the outlet (caudal end). Flow in the caudal direction was assigned a positive sign and in the cranial direction a negative sign.

The different flow conditions applied at the cranial end included two waveforms, three flow velocities and three cycle rates, tested on all three models. The two waveforms were sinusoid and quasi-sinusoid. The quasi-sinusoidal wave was the spatial average of the flow measurement acquired at the foramen magnum with PC MR in the Chiari patient (Figure 3), adjusted to have zero net flow over one cycle. This waveform displayed a period of 0.87 sec, with 0.37 sec of caudally directed flow and 0.50 sec of cranially directed flow. Peak velocity was 3.13 cm/sec in the caudal direction and 2.14 cm/sec in the cranial direction. The sinusoidal waveform had a period of 1 sec and an amplitude of 3.13 cm/sec. To compare results from the two different waveforms, the period of the quasi-sinusoidal waveform was adjusted (by standard stretching)

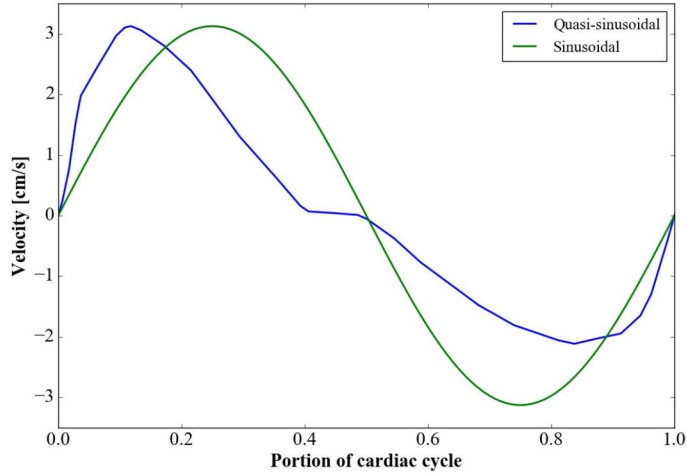


Figure 3: The quasi-sinusoidal inlet velocity waveform acquired by phase-contrast magnetic resonance (solid line) and the sinusoidal waveform (dotted line) used in the models. The quasi-sinusoidal waveform has caudal (positive) flow of short duration (40% of the cycle) corresponding to systole and cranial (negative) flow of longer duration (approximately 60% of the cycle) corresponding to diastole.

to 1 sec. Moreover, to test the effect of cycle rates, we used the quasi-sinusoidal waveform. Three cycle rates were created by changing the period length of the inlet velocity wave to 60, 90 and 120 cycles per minute (cpm). Finally, for the different flow velocities, the peak caudal velocity at the inlet was set to 1.56, 3.13 and 4.69 cm/sec.

The Navier-Stokes equations for an incompressible Newtonian fluid were used to simulate fluid flow in the SAS and in the syrxinx for each of the conditions. The equations (Navier-Stokes and the dynamic linear elasticity equation) were solved simultaneously in a moving domain using the FEniCS [6] finite element software, with methods previously described [13]. Simulations were performed over 8 seconds, to reach an oscillatory steady state solution. Peak caudal and cranial velocities from the final cycle were tabulated for each model and boundary condition.

CSF and syrxinx fluid velocities through the cardiac cycle were displayed in color-coded images. Peak velocities were plotted over time in Paraview for the 3 models and the different boundary conditions. The velocity in the middle of the syrxinx through a cycle was inspected to determine the frequency of the fluid oscillations within the syrxinx.

Results

In vivo fluid velocity measurements

Sagittal images obtained prior to surgery in the patient showed a syrxinx 7 mm in diameter which diminished in size at 2 months and disappeared at 10 month after craniovertebral de-

compression (Figure 1). The length of the syringe did not change from the preoperative state to 2 months after surgery. In the preoperative study, peak weighted mean velocity (magnitude) was 3.6 cm/sec in the SAS (caudal direction) and 2.0 cm/sec in the syringe (cranial direction) (Figure 4). The heart rate was 73 beats per minute, and the fluid in the syringe displayed close to three full oscillations per cardiac cycle, a cycle rate of approximately 210 cpm. Preoperatively, CSF flow in the SAS was synchronously bidirectional at some cardiac phases.

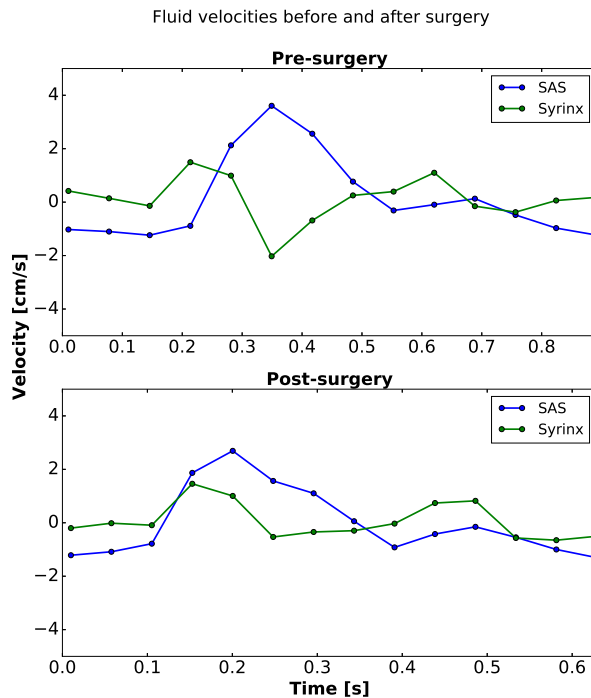


Figure 4: Plot of cerebrospinal fluid (CSF) and syringe fluid velocities over one cardiac cycle before and after surgery. Subarachnoid space (SAS) velocities are averaged along the cervical cord at the 1 o'clock location in the SAS. Preoperatively, the SAS has a peak of 3.6 cm per second in the caudal direction, and fluid in the syringe has a peak velocity of 2.0 cm per second in the cranial direction. The CSF flow has a unimodal pattern, with one peak in the positive direction and one of smaller magnitude and greater duration in the negative direction. Flow in the syringe fluid has a multimodal pattern with three peaks in each direction. Peak caudal flow in the CSF coincides with peak cranial flow in the syringe. The heart rate was recorded as 73 beats per minute (bpm). Postoperatively, CSF flow had a peak of 2.7 cm per second in the caudal direction, a 29% reduction from the preoperative study. The fluid in the syringe had a peak of 1.5 cm per second, also in the caudal direction, a 25% decrease from the preoperative study. The pulse was recorded at 97 bpm. Peak CSF velocity in the same locations in the SAS at 10 months after surgery remained stable at 2.4 cm per second in the caudal direction (no plot shown).

At two months post-surgery, peak weighted average velocities in the SAS were reduced to 2.7 cm/sec (caudal direction) and in the syringe to 1.5 cm/sec (caudal direction) (4). The relative decrease in flow was 29% in the SAS and 25% in the syringe. In general, fluid velocities throughout the subarachnoid space and syringe were reduced post-surgery. The heart rate during the image acquisition post-surgery was 97 beats per minute, and the fluid in the syringe postoperatively had close to two full oscillations per cardiac cycle, a cycle rate of approximately 200 cpm.

At the 10-month postoperative time point, the syringe had essentially resolved. CSF flow throughout the cervical SAS remained in the range of the velocities measured at 2 months post-operation.

Flow simulations

Fluid velocities in the syringe varied with location in the fluid space, time in the cycle, syringe diameter, CSF inlet velocity, inlet waveform and cycle rate (Table 1).

Table 1: Peak syringe fluid and cerebrospinal fluid (CSF) velocities in the subarachnoid space (SAS) as a function of inlet velocity amplitude, cycle rate and syringe size for the quasi-sinusoidal inlet profile.

		Inlet velocity 1.56 cm/sec		Inlet velocity 3.13 cm/sec		Inlet velocity 4.69 cm/sec	
Cycle rate (cpm)	Syringe diameter (mm)	SAS velocity (cm/sec)	Syringe velocity (cm/sec)	SAS velocity (cm/sec)	Syringe velocity (cm/sec)	SAS velocity (cm/sec)	Syringe velocity (cm/sec)
60	No Syringe	1.79	NA	3.57	NA	5.36	NA
	2	2.06	1.41	4.10	2.82	6.16	4.21
	6	2.43	1.03	4.86	1.87	7.31	3.08
90	No Syringe	1.85	NA	3.23	NA	5.55	NA
	2	1.87	1.47	3.73	2.85	5.62	4.42
	6	2.25	0.91	4.49	1.71	6.65	2.65
120	No Syringe	1.82	NA	3.64	NA	5.46	NA
	2	2.19	4.35	4.25	7.87	5.57	10.94
	6	3.06	3.18	7.92	7.70	13.09	12.70

SAS = subarachnoid space; NA = not available; cpm = cycles per minute;

Spatially, velocities varied with distance from the edges of the fluid spaces. Velocities were greater in the central zones in the syringe and SAS than at the borders. A detailed illustration of flow patterns of CSF and syringe fluid throughout the cardiac cycle is given in Figure 5. In this figure, the quasi-sinusoidal inlet waveform at 60 cpm with 3.13 cm/sec inlet velocity amplitude was used in the model with the larger syringe.

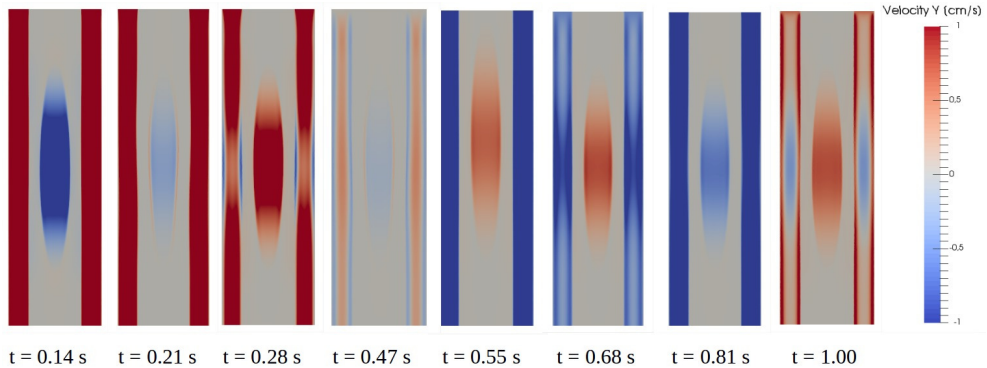


Figure 5: Flow images showing spatial variation from eight time points in the cardiac cycle in the 6 mm syringe model, at 60 cycles per minute cycle rate, 3.13 cm per second inlet velocity and quasi-sinusoidal velocity waveform. The first three images show cerebrospinal fluid (CSF) flow primarily in the caudal direction and change from cranial to caudal flow in the syringe. The fourth image shows relatively stagnant flow with bidirectionality both in the CSF and the syringe. The next three images show CSF flow in the cranial direction. The final image shows relatively stagnant flow again. The first image ($t = 0.14$ seconds) shows CSF and syringe peak velocities in the caudal and cranial direction, respectively. At $t = 0.21$ seconds, bidirectional flow is seen in the syringe as fluid close to the syringe walls reverses direction earlier than fluid in central regions. Between $t = 0.28$ seconds and $t = 0.47$ seconds, CSF flow is close to stagnant, and has some changes in directionality near the wall, and flow in the syringe is caudal ($t = 0.28$ seconds), cranial (not shown) and caudal again ($t = 0.47$ seconds). In the next three phases, ($t = 0.55$ seconds, $t = 0.68$ seconds, $t = 0.81$ seconds), CSF flows in the cranial direction, while syringe fluid oscillates back and forth at a rate of approximately 240 cycles per minute. At the final stage of the cycle ($t = 1.00$), CSF flow has started to flow in the caudal direction. Longitudinal variation of flow in the subarachnoid space is associated with movements of spinal cord tissue, especially adjacent to the syringe.

The effect of inlet waveform With the sinusoidal waveform at 60 cpm and inlet velocity amplitude of 3.13 cm/sec, syringe fluid moved concurrently in the syringe and SAS, but in opposite directions and with different magnitudes, reaching a peak of 0.29 cm/sec in the middle of the 6 mm diameter syringe compared to 3.4 cm/sec in the central SAS (Figure 6). Moreover, with the sinusoidal waveform, the oscillation rate within the syringe equaled the cycle rate in the SAS (as in Figure 6) for all inlet velocities and all cycle rates.

Changing the inlet velocity waveform from sinusoidal to quasi-sinusoidal (the waveform obtained in the Chiari I patient) increased the frequency and amplitude of the syringe fluid oscillations (Figure 6). Peak syringe fluid velocity occurred in the cranial direction, simultaneously with peak SAS velocity in the caudal direction. When the inlet velocity was quasi-sinusoidal, fluid in the syringe had 2, 3 or 4 oscillations per cycle in the SAS (Figure 6). The fluid in the syringe oscillated with frequency of about 240 cpm, independent of the cycle rate in the SAS. For example, when the cycle rate in the SAS was increased from 60 to 120 cpm, the number of os-

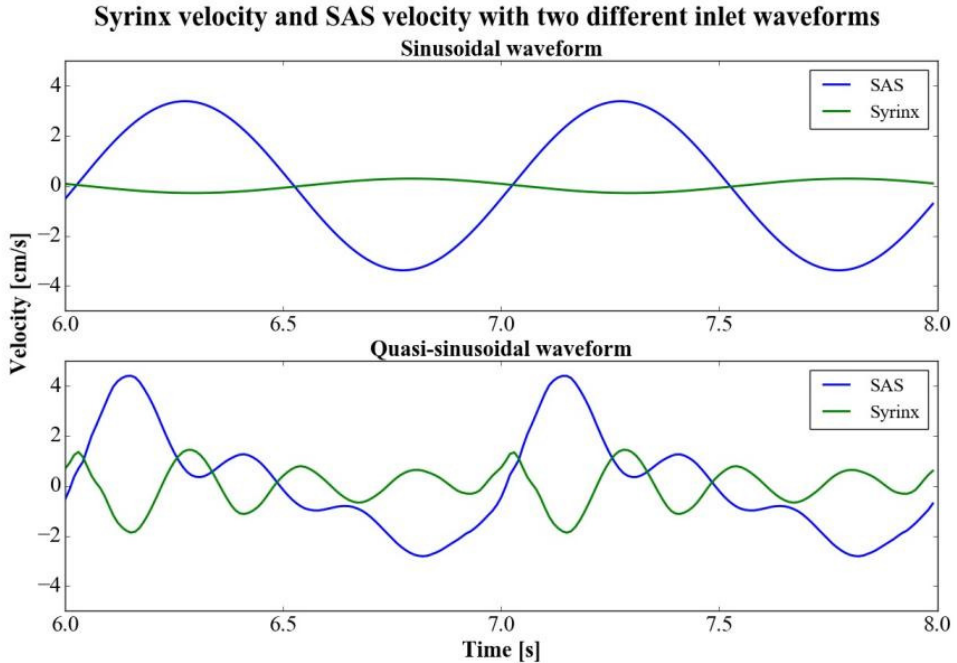


Figure 6: Plot of velocities centrally in the subarachnoid space (SAS) and the syring over two cycles (from six seconds to eight seconds in the simulation) for the sinusoidal inlet waveform (upper plot) and quasi-sinusoidal velocity waveform that was measured in a Chiari I patient (lower plot). The flow conditions for these plots were: inlet velocity 3.13 cm per second, cycle rate 60 cycles per minute and a 6 mm diameter syring (the same parameter setting as Figure 5). For the sinusoidal flow condition, fluid movement is unimodal both in the SAS and the cyst. For the quasi-sinusoidal velocity waveform, cerebrospinal fluid flow is unimodal and syring fluid flow is multimodal (four oscillations). Peak syring fluid velocities are greater in the cranial direction than in the caudal direction for quasi-sinusoidal inlet flow. The pattern corresponds well to in vivo measurements that show during systole (caudal SAS flow) flow in the syring is cranial. Later in the cycle, syring velocities diminish.

oscillations in the syring per cycle in the SAS decreased from 4 to 2. Syring fluid velocities were greater when the inlet velocity was quasi-sinusoidal than when it was sinusoidal. Peak SAS and syring velocity for varying inlet velocities, syring diameters and cycle rates are reported in Table 1 for the quasi-sinusoidal waveform.

The effect of velocity at the inlet Peak syring velocity increased with increases in inlet velocity (from 1.56 to 3.13 and 4.69 cm/sec) at all three cycle rates in both syringes (Table 1, Figure 7). The change in syring fluid velocity appeared linear with change in inlet velocity for each of the three cycle rates (Figure 7), thus an increase in inlet velocity led to the same relative increase

in syringe velocity (i.e. a 50% increase in inlet velocity led to a 50% increase in syringe velocity). Increasing CSF inlet velocities from 1.56 to 4.69 cm/sec increased peak cyst fluid velocities for the three cycle rates in the 2 mm syringe by 151 to 200% and in the 6 mm syringe by 191 to 299%. A change in inlet velocity did not change the frequency of oscillations within the syringe. SAS peak fluid velocities were greater in the caudal direction and peak syringe fluid velocities greater in the cranial direction.

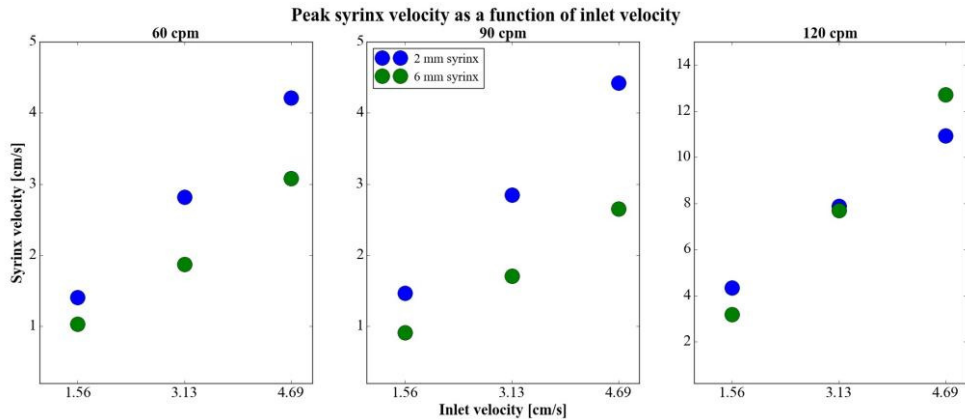


Figure 7: Peak syringe velocity as a function of inlet velocity, at 60 (left), 90 (middle) and 120 (right) cycles per minute (cpm). Syringe and cerebrospinal fluid velocities appear to increase linearly with inlet velocity for all cycle rates.

The effect of cycle rate The effect of cycle rate on peak syringe velocities was nonlinear. Syringe velocities changed little with an increase of cycle rate from 60 to 90 cpm and increased by more than 100% with a further increase of cycle rate to 120 cpm (Figure 8). For example, with an inlet velocity of 4.69 cm/sec, the peak syringe velocity in the 6 mm syringe decreased from 3.08 cm/sec to 2.65 cm/sec with increase in cycle rate from 60 to 90 cpm. When the cycle rate was increased to 120 cpm, peak syringe velocity increased to 12.70 cm/sec. For the 2 mm syringe an increase in cycle rate from 60 to 120 cpm increased peak syringe velocities by 160 to 209% for the three cycle rates. Similarly, peak velocities in the 6 mm syringe increased by 209 to 312% by an increase from 60 to 120 cpm (Table 1).

Effect of syringe diameter Syringe diameter had little effect on observed peak syringe velocities compared to the other parameters investigated. Peak syringe velocities over the 3 cycle rates and 3 inlet velocities averaged 4.5 cm/sec for the 2 mm syringe and 3.9 cm/sec for the 6 mm syringe (Table 1). Peak syringe velocity decreased with increased syringe size in 8 of the 9 test conditions (Figure 9, Table 1).

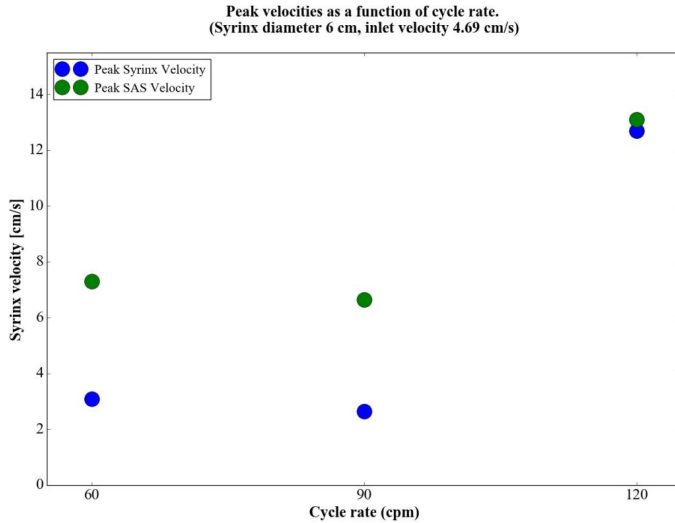


Figure 8: Peak syringe fluid velocity as a function of cycle rate for the 4.69 cm per second inlet velocity. Velocity diminished by less than 10% between 60 and 90 cycles per minute and increased by more than 100% between 90 and 120 cycles per minute. At the 1.56 and 3.13 cm per second inlet velocities, the same relative effect of cycle rate was noted (data not shown).

Discussion

Fluid in a spinal cord syrinx observed with PC MR or in a computational model displayed faster oscillations and sometimes greater velocities than in the CSF. In the patient, CSF and syrinx velocity decreased after craniovertebral decompression surgery. Similarly, in the model, changes in CSF velocities led to proportional changes in syrinx fluid velocities. Increasing cycle rates from 60 to 90 cpm had little effect on syrinx fluid velocities while increasing from 90 to 120 cpm increased syrinx velocities markedly. Fluid velocities tended to be slower in the larger syrinx. Peak syrinx fluid velocities, contrary to those in the SAS, tend to be greater in the cranial than in the caudal direction.

Our finding of oscillatory flow in syrinx cavities is consistent with *in vivo* observations of syrinx fluid flow reported previously. Honey et al. [3], using dynamic MR imaging, observed oscillatory flow of fluid in a syrinx, but reported no velocity measurements. Similar to our findings, Lichtor et al. [4] found syrinx fluid velocity of comparable magnitude to flow in the SAS before surgery, but saw a greater decrease in syrinx velocity after surgery. In contrast to these two studies, we found peak syrinx fluid velocity to occur in the cranial direction before surgery. The syringes studied in these two reports differed from those in our patient in location and size (both width and length) of the syrinx, which may explain some of this difference. Incoherent movement of syrinx fluid has been documented previously [10], and variable syrinx fluid velocities have been observed depending on syrinx length [2]. We are not aware of additional experimental studies documenting fluid velocities in syrinx and SAS simultaneously. In a com-

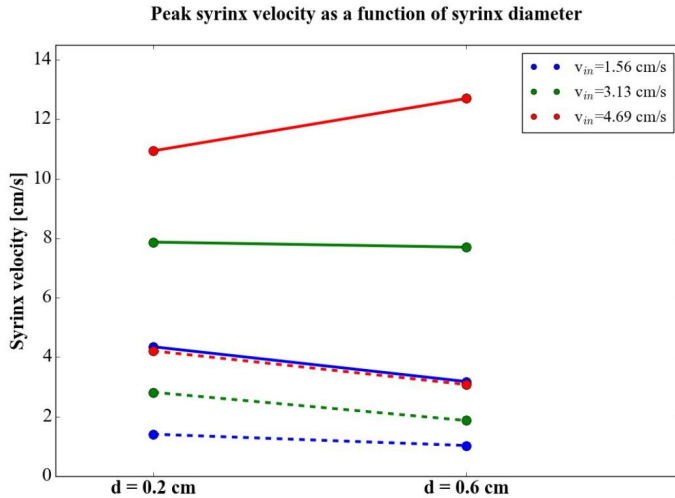


Figure 9: Peak syrnix fluid velocity as a function of syrnix size at 60 (dashed lines) and 120 (solid lines) cycles per minute with three different inlet velocities. The figure shows syrnix had lower velocities in five of six instances. In eight of the nine test cases in total, syrnix velocities decreased with increased syrnix size, and the average peak velocity decreased from 4.5 cm per second in the smaller syrnix to 3.9 cm per second in the larger.

putational model, Bertram has previously showed that pressure waves related to coughing can initiate rapid fluid movement up to 1 cm/sec in the syrnix cavity [1]. In contrast, cord movement in our model was initiated by movement of CSF during the cardiac cycle, which under some conditions caused syrnix velocity to exceed the value found by Bertram [1].

Our model has limitations. It lacks the variations in cross sectional area and longitudinal axis of the subarachnoid space, which characterize the human cervical subarachnoid space. Therefore the model lacks the acceleration of fluid velocities in the SAS that occur in the upper cervical spine [11]. For this reason, fluid velocities were applied constant in space at the inlet of our model. Also, the no displacement condition on the boundaries of our model could cause artificial wave reflections resulting in pressure waves traveling up and down the cord. It is not known whether these pressure waves are observed in-vivo, however such waves of fluid movement in the syrnix were observed in-vivo in our MR study as well as others [10]. In addition such waves were predicted in silico by Bertram et al. [1], when the length of the cord was extended. We observed a resonance frequency of approximately 120 cpm, at which syrnix velocities were vastly increased. The exact resonance frequency would possibly change with patient specific cord lengths and properties, which were not taken into account in our model. Modeling flow was limited to 2D because of the excessive computational times required for 3D simulations. We did not change the velocity waveform with increases in cycle rate but retained the same proportion of systolic and diastolic flow phases, since the changes in waveform with increasing heart rate are not known. We assumed that stroke volume decreased proportionally with increasing heart rate, although not all investigators make this assumption [5]. Our assumption

is reasonable if the cerebral blood flow is independent of heart rate, and the blood entering the brain pushes CSF caudally in accordance with the Monro-Kellie hypothesis. However, cerebral blood flow has been shown to increase with exercise and to decrease during heavier exercise [8]. If diastole shortens to a greater extent than systole with increasing heart rate, then our model may overestimate syrinx velocities at higher cycle rates.

Conclusions

Fluid in syrinx cavities moves during the cardiac cycle, affected by heart rate and CSF fluid velocity. Velocities in the cyst range over a wide range of values. The frequency of fluid oscillation in a syrinx does not vary with heart rate or CSF velocity.

Acknowledgements Part of the MR-study was presented (“Assessment of CSF Velocities and Cord Motion Before and After Chiari 1 Decompression”) by Dr. Justin Brucker at the 2015 ASNR meeting in Las Vegas, NV, United States.

References

- [1] C. Bertram. A numerical investigation of waves propagating in the spinal cord and subarachnoid space in the presence of a syrinx. *Journal of Fluids and Structures*, 25(7):1189–1205, 2009.
- [2] P. Brugières, I. Idy-Peretti, C. Iffenecker, F. Parker, O. Jolivet, M. Hurth, A. Gaston, and J. Bittoun. CSF flow measurement in syringomyelia. *American journal of neuroradiology*, 21(10):1785–1792, 2000.
- [3] C. Honey, K. Martin, and M. Heran. Syringomyelia fluid dynamics and cord motion revealed by serendipitous null point artifacts during Cine MRI. *American Journal of Neuro-radiology*, 38(9):1845–1847, 2017.
- [4] T. Lichtor, P. Egofské, and N. Alperin. Noncommunicating Cysts and Cerebrospinal Fluid Flow Dynamics in a Patient With a Chiari I Malformation and Syringomyelia—Part II. *Spine*, 30(12):1466–1472, 2005.
- [5] S. Linge, K.-A. Mardal, V. Haughton, and A. Helgeland. Simulating CSF flow dynamics in the normal and the Chiari I subarachnoid space during rest and exertion. *American Journal of Neuroradiology*, 34(1):41–45, 2013.
- [6] A. Logg, K.-A. Mardal, and G. Wells. *Automated solution of differential equations by the finite element method: The FEniCS book*, volume 84. Springer Science & Business Media, 2012.
- [7] B. A. Martin, R. Labuda, T. J. Royston, J. N. Oshinski, B. Iskandar, and F. Loth. Spinal subarachnoid space pressure measurements in an in vitro spinal stenosis model: implications on syringomyelia theories. *Journal of biomechanical engineering*, 132(11):111007, 2010.

- [8] S. Ogoh and P. N. Ainslie. Cerebral blood flow during exercise: mechanisms of regulation. *Journal of applied physiology*, 107(5):1370–1380, 2009.
- [9] H. Ozawa, T. Matsumoto, T. Ohashi, M. Sato, and S. Kokubun. Mechanical properties and function of the spinal pia mater. *Journal of Neurosurgery: Spine*, 1(1):122–127, 2004.
- [10] Pinna, Giampietro and Alessandrini, Franco and Alfieri, Alex and Rossi, Marcella and Bricolo, Albino. Cerebrospinal fluid flow dynamics study in chiari i malformation: implications for syrinx formation. *Neurosurgical focus*, 8(3):1–8, 2000.
- [11] S. Shah, V. Haughton, and A. M. del Río. CSF flow through the upper cervical spinal canal in Chiari I malformation. *American Journal of Neuroradiology*, 32(6):1149–1153, 2011.
- [12] J. H. Smith and J. A. Humphrey. Interstitial transport and transvascular fluid exchange during infusion into brain and tumor tissue. *Microvascular research*, 73(1):58–73, 2007.
- [13] V. Vinje. Simulating cerebrospinal fluid flow and spinal cord movement associated with syringomyelia. Master’s thesis, 2016.

Paper 2

**Respiratory influence on cerebrospinal
fluid flow – a computational study
based on long-term intracranial pres-
sure
measurements**

Respiratory influence on cerebrospinal fluid flow – a computational study based on long-term intracranial pressure measurements

Vegard Vinje^{1,*}, Geir Ringstad^{2,5}, Erika Kristina Lindstrøm⁴, Lars Magnus Valnes⁴, Marie E. Rognes¹, Per Kristian Eide^{2,3}, and Kent-Andre Mardal^{1,4}

¹Department of Scientific Computing and Numerical Analysis, Simula Research Laboratory, 1325 Lysaker, Norway.

²Institute of Clinical Medicine, Faculty of Medicine, University of Oslo, 0315 Oslo, Norway.

³Department of Neurosurgery, Oslo University Hospital - Rikshospitalet, 0372 Oslo, Norway.

⁴Department of Mathematics, University of Oslo, 0315 Oslo, Norway.

⁵Department of Radiology and Nuclear Medicine, Oslo University Hospital - Rikshospitalet, 0372 Oslo, Norway.

*vegard@simula.no

ABSTRACT

Current theories suggest that waste solutes are cleared from the brain via cerebrospinal fluid (CSF) flow, driven by pressure pulsations of possibly both cardiac and respiratory origin. In this study, we explored the importance of respiratory versus cardiac pressure gradients for CSF flow within one of the main conduits of the brain, the cerebral aqueduct. We obtained overnight intracranial pressure measurements from two different locations in 10 idiopathic normal pressure hydrocephalus (iNPH) patients. The resulting pressure gradients were analyzed with respect to cardiac and respiratory frequencies and amplitudes (182,000 cardiac and 48,000 respiratory cycles). Pressure gradients were used to compute CSF flow in simplified and patient-specific models of the aqueduct. The average ratio between cardiac over respiratory flow volume was 0.21 ± 0.09 , even though the corresponding ratio between the pressure gradient amplitudes was 2.85 ± 1.06 . The cardiac cycle was 0.25 ± 0.04 times the length of the respiratory cycle, allowing the respiratory pressure gradient to build considerable momentum despite its small magnitude. No significant differences in pressure gradient pulsations were found in the sleeping versus awake state. Pressure gradients underlying CSF flow in the cerebral aqueduct are dominated by cardiac pulsations, but induce CSF flow volumes dominated by respiration.

Introduction

The interplay between intracranial pressure (ICP) and cerebrospinal fluid (CSF) flow plays an important role in e.g. cerebral homeostasis¹, neurological conditions such as idiopathic normal pressure hydrocephalus (iNPH)², and cerebral metabolic waste clearance³. For instance, in the context of iNPH patients, ICP amplitudes, CSF flow quantities such as aqueductal stroke volumes (ASVs), and auxiliary quantities such as compliance, have all been considered for predicting clinical response to shunt surgery⁴. According to the traditional view (the *third circulation*) introduced by Cushing in 1925⁵, CSF is mainly produced in the choroid plexus of the four ventricles and is mainly absorbed into the venous system through the arachnoid granulations. Over the last century and to a great extent in the recent decades, the classical view has been challenged – in particular in terms of CSF production⁶, routes and modes of (re-)absorption^{3,7}, the drivers of CSF pulsatility⁴, and the effect of sleep^{8,9}.

Over the last 30 years, cranial CSF flow has been studied extensively and non-invasively via PC-MRI techniques¹⁰⁻¹⁵. Using cardiac-gated MRI, it was early shown that cardiac-induced CSF flow pulsations

vastly dominate the flow involved in the third circulation¹⁰. Later, respiration was also identified to influence CSF flow¹⁶. However, the relative importance of the cardiac and respiratory cycle is debated. Recent experimental studies have resulted in disparate findings: comparable contribution of respiration and cardiac pulsations to CSF velocities¹³, a significantly greater cardiac CSF velocity component¹⁷, and, conversely, inspiration as the most important driving force for CSF flow¹². On the subject of a potential net CSF flow (in contrast or rather in addition to the pulsatile behavior), the current understanding is also incomplete. Cardiac-gated PC-MRI investigations have indicated considerable net CSF flow (vastly larger than the 0.5 L/day supposedly involved in the classical third circulation view), and moreover shown considerable variations between iNPH patients and controls^{14,18}. On the other hand, there is evidence that net CSF flow in the cerebral aqueduct is confounded by the respiratory cycle^{15,19}, questioning the validity of net CSF flow measured with cardiac gated PC-MRI.

In contrast, it is well-established that the dominating component of the ICP is the pressure pulsation of the cardiac cycle while the respiratory pulsation is considerably smaller²⁰. In iNPH patients, the mean ICP wave amplitude related to the cardiac cycle has proved useful in predicting responders from surgery²¹. Static transmantle pressure gradients have not been demonstrated^{22,23}. However, the classical view of the third circulation as well as recent findings of net CSF flow within the cerebral aqueduct¹⁴ suggest the existence of a static transmantle pressure gradient in addition to a pulsatile component. The existence of pulsatile pressure gradients has been hypothesized – as indeed suggested by the cardiac and respiratory CSF flow cycles. ICP differences in the cerebral aqueduct have been estimated from PC-MRI flow measurements^{24,25}. However, very few have studied pulsatile ICP gradients clinically and directly²². Furthermore, the respiratory component in the ICP (gradient) signal has so far received very limited attention.

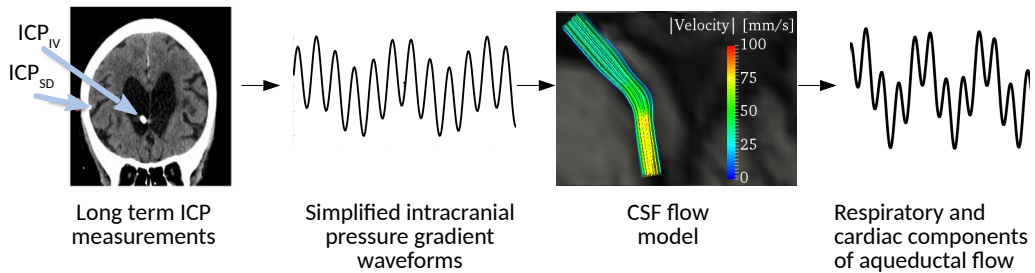


Figure 1. A schematic description of the steps involved in the present study. Subdural and ventricular long term ICP recordings were obtained in vivo and subtracted to find the ICP gradient. To compute aqueductal flow in both simplified and patient-specific geometries, a simplified ICP gradient consisting of two frequencies were constructed: one for the cardiac, and one for the respiratory component. The resulting flow rate was analyzed to compute peak volumetric flow rates as well as aqueductal stroke- and respiratory volumes.

As the conflicting evidence shows, the current understanding of cardiac and respiratory influences on CSF flow and ICP, and on the relationship between the ICP and PC-MRI modalities, is inadequate. However, from a biomechanical point of view, the relationship between CSF flow and ICP gradients is governed by the Navier–Stokes equations and the CSF flow induced by pulsating (cardiac and/or respiratory) or near steady (third circulation) pressure gradients can readily be computed. Indeed,

from computational studies it is well-known that the magnitude of CSF pressure gradients is only a small fraction of the ICP pulsation (typically >5 mmHg during a cardiac cycle)². For example, a 42 μL aqueductal stroke volume was estimated to correspond to an approximately 0.01 mmHg pressure drop in both a rigid and a deformable normally shaped patient-specific geometry²⁶, while other computational studies have estimated a transmante pressure difference of up to 0.03 mmHg^{24,27}. Severely stenosed aqueducts may however have pressure drops that are orders of magnitude higher²⁸.

On this background, the aim of this study was to investigate the relative importance of cardiac and respiratory contributions to ICP gradients, CSF flow rates and CSF flow volumes, and their interplay. An overview of the steps involved in the present study is shown in Figure 1. In particular, we aimed to characterize the CSF flow induced by pulsatile cardiac and respiratory ICP gradients. We used a unique set of long-term in-vivo ICP measurements from two different intracranial locations in a cohort of 10 iNPH patients, to compute intracranial pressure gradients (dICPs). The ICP recordings were obtained from overnight registrations of patients breathing freely, and by extracting multiple 6-minute windows, a typical acquisition time of a PC-MRI scan. The dICP was subsequently used as the driving force in fluid dynamics models of the cerebral aqueduct. To utilize all the input data from the dICP recordings, an analytical solution of the flow field in a simplified geometry was first used and finally some of the input data was used on patient-specific geometries as well. In both models, we measured the cardiac- and respiratory induced peak volumetric flow rate (PVF), as well as the aqueductal stroke volume (ASV) and the corresponding aqueductal respiratory volume (ARV). The dICP data of each patient was separated into different time-frames to assess the effect of sleep on dICP amplitude and frequency. Finally, we compared the pressure gradients involved in the cardiac and respiratory cycles with the static pressure gradients involved in the third circulation.

Results

Quantification of pulsatile intracranial pressure gradients

We analyzed the ICP measurements, as shown for patient 1 in Fig. 2a and b (and for all patients in Supplementary Fig. S1), by computing pulsatile ICP gradients (dICPs) as the difference between the two pressure sensor measurements divided by the distance between the sensors, and extracted sets of 6-minute windows of the resulting dICP waveforms (Fig. 2c). A total of 502 accepted 6-minute windows, consisting of approximately 182,000 cardiac cycles and 48,000 respiratory cycles were retrieved from the patients. For one patient (patient 10), the pressure window extraction resulted in only one accepted time window. This individual was excluded, leaving 9 patients for further study.

We subsequently computed the power spectra of the 6-minute window dICP waveforms to identify and quantify the dominant signal frequencies and amplitudes (Fig. 3, Table 1). The waveforms consistently displayed two main frequency peaks, one related to the cardiac cycle and one to the respiratory cycle (Fig. 3a). The average heart rate ranged from 50 to 78 beats/minute for the 9 patients, while the respiratory period ranged from 13 to 17 cycles/minute (Table 1). At the cohort level, the (average \pm standard deviation) heart rate was 62 ± 9 per minute and the respiratory rate was 15 ± 1 per minute. The average cardiac and respiratory periods plus/minus one standard deviation stayed well within the selected range defining the respiratory and heart rates (cf. Methods).

The signals persistently displayed pulsatile ICP gradients with both cardiac and respiratory contributions (Fig. 2d, Fig. 3a). The average dICP amplitudes showed variability between patients, ranging from 0.86 to 3.23 mmHg/m for the cardiac component, and from 0.30 to 0.88 mmHg/m for the respiratory cycle (Fig. 3b, Table 1). The average cardiac dICP amplitude dominated the respiratory dICP amplitude by a factor of 2.85, with patients having average factors between 1.91 and 5.11 and a cohort

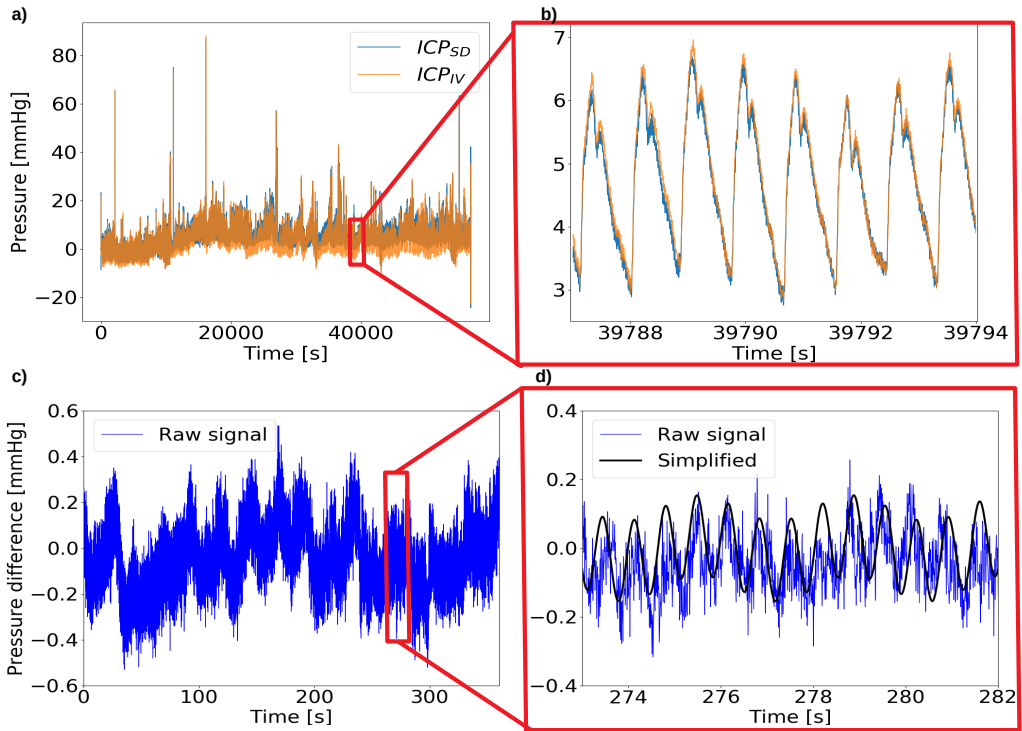


Figure 2. a) Raw subdural ICP (ICP_{SD} (blue)) and intraventricular ICP (ICP_{IV} (orange)) for patient 1 (PatID 1) over the entire measuring period, before window selection. b) A zoom of a), demonstrating the small difference between the subdural and intraventricular ICP relative to ICP amplitudes (the latter typically being 4-5 mmHg). c) An accepted 6-minute window for patient 1 after a shift to zero mean pressure difference. d) $dICP$ amplitudes are considerably smaller than the ICP amplitudes. d), a zoom of c), showing the pressure difference in blue (difference between the two raw signals) and the simplified pressure difference (black) $\frac{\partial p}{\partial z} L$ derived from equation (2)

standard deviation of 1.06.

Comparing intracranial pressure gradients between sleep and wakefulness

Sleep has been reported to affect multiple aspects of cerebral fluid dynamics including solute transport⁸ and blood flow⁹. We therefore analyzed the intracranial pressure gradients further to investigate whether the cardiac and respiratory contributions differ between the sleep and awake state. To this end, we categorized all 6-minute windows as belonging to either the sleeping or awake state, and computed the average cardiac and respiratory amplitude and frequency for each state in each patient. No statistical differences were found in the sleeping versus awake state in any of these parameters (Fig. 3c, paired t-test, $p > 0.5$ for all parameters).

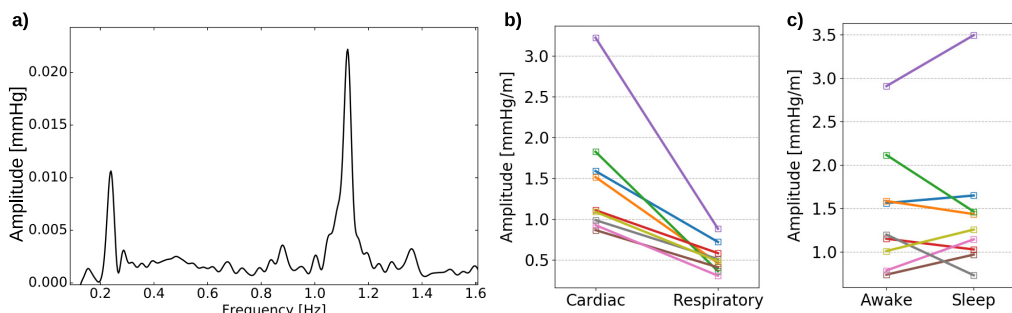


Figure 3. a) The power spectrum of the pressure difference in an accepted 6-minute window from patient 1 after noise removal. Two peaks are evident, one related to the cardiac cycle (~ 1.1 Hz) and one related to the respiratory cycle (~ 0.2 Hz). Low frequencies (< 0.1 Hz) are not shown. b) Average dICP amplitude for each patient, cardiac vs respiratory. All patients had lower respiratory amplitudes on average. c) Average cardiac dICP amplitude for each patient during the awake and sleeping state. Although some variations were found from patient to patient, no clear trend was evident.

Cardiac-dominated ICP gradients induce evenly distributed flow rates and peak velocities

In our data (Table 1), the cardiac contribution to the pulsatile ICP gradient dominates the respiratory component. On the other hand, other studies have reported that respiration is a substantial regulator of CSF flow^{12,13}. Aiming to reconcile these observations via computational modelling, we investigated the fluid flow that would be induced by pulsatile intracranial pressure gradients. In particular, we assessed the CSF flow that could be induced in a cerebral aqueduct as a result of cardiac and respiratory ICP gradients.

We first considered simplified, two-frequency dICP waveforms by combining the cardiac and respiratory components of the pulsatile ICP gradients – for all 6-minute time windows in all patients. Using the simplified waveform as a driving force, we estimated the CSF velocities in a cylindrical model of the cerebral aqueduct using the incompressible Navier–Stokes equations. We subsequently computed the cardiac- and respiratory-induced volumetric flow rates over time and cardiac and respiratory peak volumetric flow rates (PVFs).

Figure 4a shows the simplified dICP waveform and the induced volumetric flow rate for the average cardiac and respiratory ICP gradients for patient 2. In this example, the dICP waveform is dominated by the contribution from the cardiac cycle: the cardiac dICP amplitude was 3.31 times the respiratory dICP amplitude (Table 1, patient 2). However, the volumetric flow rate induced by the dICP waveform was close to evenly regulated by the two frequencies. The ratio between cardiac and respiratory PVF was 1.18, with a cardiac component of 0.38 mL/s and a respiratory component of 0.32 mL/s (Table 2, patient 2).

In the cohort in general, the cardiac-dominated ICP gradients induced cardiac and respiratory PVFs of comparable magnitudes (Table 2). The cohort had a cardiac PVF of 0.31 ± 0.16 mL/s and a respiratory PVF of 0.35 ± 0.13 mL/s. The individual average PVFs varied between 0.15 and 0.70 mL/s for the cardiac, and 0.19 and 0.62 mL/s for the respiratory cycle (Fig. 4c). The cohort ratio between cardiac and respiratory PVF was 0.90 ± 0.33 , ranging individually from 0.55 to 1.46. We also observed that the peak velocity (in any location of the cerebral aqueduct and at any time point) typically reached 5-6

PatID	N	L (cm)	Heart rate (Beats per minute)	Respiratory rate (Breaths per minute)	Cardiac pressure gradient, a_1 (mmHg/m)	Respiratory pressure gradient, a_0 (mmHg/m)	Pressure gradient ratio a_1/a_0
1	21	6.8	78 ± 9	17 ± 2	1.59 ± 0.47	0.72 ± 0.23	2.22
2	56	5.5	51 ± 9	15 ± 4	1.52 ± 0.85	0.46 ± 0.12	3.31
3	53	7.0	67 ± 2	15 ± 3	1.83 ± 0.74	0.36 ± 0.09	5.11
4	105	5.3	59 ± 4	13 ± 3	1.11 ± 0.47	0.58 ± 0.27	1.91
5	89	3.2	59 ± 4	14 ± 3	3.23 ± 1.12	0.88 ± 0.29	3.67
6	55	7.0	74 ± 7	17 ± 3	0.86 ± 0.23	0.41 ± 0.13	2.13
7	60	7.9	53 ± 7	17 ± 4	0.93 ± 0.52	0.30 ± 0.12	3.06
8	27	5.7	54 ± 3	15 ± 3	0.99 ± 0.61	0.51 ± 0.23	1.94
9	36	5.3	64 ± 4	16 ± 4	1.09 ± 0.43	0.48 ± 0.17	2.26
Avg.	55	6.0	62 ± 9	15 ± 1	1.46 ± 0.74	0.52 ± 0.18	2.85 ± 1.06

Table 1. Statistics from the dICP analysis. The last row shows average and standard deviation of average values from each individual patient. All values in the table have been rounded after as exact computations as possible. N: number of accepted 6-minute windows. L: distance between ICP sensors.

cm/s, with equal contribution from the cardiac and respiratory cycle. The cross-sectional average of the velocity reached only half of this value, approximately 3 cm/s.

Evenly distributed CSF flow rates induce respiratory-dominated aqueductal flow volumes

Aqueductal stroke volume (ASV) has been proposed as a non-invasive marker of shunt response in iNPH. However, a challenge for the use of ASV derived from cardiac-gated PC-MRI is the effect of respiration, as respiration is traditionally not controlled for. To evaluate the effect of respiration on aqueductal flow volumes, we also computed the cardiac aqueductal flow volume, corresponding to the aqueductal stroke volume (ASV), and respiratory aqueductal flow volume (ARV) in the simplified model for all 6-minute time windows in all patients.

Interestingly, the computed flow volumes demonstrated a clear dominance of the respiratory component (Table 2). At the cohort level, the computed ASV was $99.3 \pm 56.0 \mu\text{L}$. The average ASV in each patient ranged from 40.2 to 228.0 μL . In comparison, the cohort-average ARV was $482.3 \pm 212.9 \mu\text{L}$ and individual patient average values ranged from 255.2 to 929.6 μL . The ratio between ASV and ARV was 0.21 ± 0.09 and ranged from 0.11 to 0.33 between patients.

In addition to inter-individual variations, there was also variability in the computed flow volumes throughout the recording time within individuals (Table 2). At the patient level, the average standard deviation of ASV between different 6-minute windows was 46.7 μL and ranged from 13.7 to 80.8 μL , while the average ARV standard deviation was 239.2 μL and ranged from 124.2 to 438.7 μL . Thus, the variability in aqueductal flow volumes within a patient and between patients was comparable: the ratio between the average standard deviation within a patient to the standard deviation between patients was 0.83 for the ASV and 1.12 for the ARV.

PatID	Cardiac PVF (mL/s)	Respiratory PVF (mL/s)	ASV (μL)	ARV (μL)	PVF ratio (A_1/A_0)	Ratio ASV/ARV
1	0.27 ± 0.09	0.44 ± 0.16	68.1 ± 27.8	523.3 ± 219.5	0.61	0.13
2	0.38 ± 0.21	0.32 ± 0.11	144.4 ± 80.8	464.2 ± 250.4	1.18	0.31
3	0.35 ± 0.15	0.24 ± 0.07	101.2 ± 46.7	330.1 ± 134.5	1.46	0.31
4	0.24 ± 0.11	0.43 ± 0.20	78.9 ± 38.7	695.6 ± 331.0	0.55	0.11
5	0.70 ± 0.23	0.62 ± 0.24	228.0 ± 79.2	929.6 ± 438.7	1.11	0.25
6	0.15 ± 0.04	0.25 ± 0.07	40.2 ± 13.7	303.7 ± 124.2	0.61	0.13
7	0.22 ± 0.13	0.19 ± 0.10	83.9 ± 52.5	255.2 ± 188.1	1.16	0.33
8	0.23 ± 0.15	0.33 ± 0.15	83.2 ± 55.9	433.8 ± 203.6	0.70	0.19
9	0.22 ± 0.08	0.31 ± 0.13	65.6 ± 25.0	404.9 ± 262.6	0.71	0.16
Avg.	0.31 ± 0.16	0.35 ± 0.13	99.3 ± 56.0	482.3 ± 212.9	0.90 ± 0.33	0.21 ± 0.09

Table 2. Statistics from the flow computations in the simplified cerebral aqueduct. The last row shows average and standard deviation of average values from each individual patient. All values in the table have been rounded after as exact computations as possible. PVF: peak volumetric flow rate. ASV: aqueductal stroke volume. ARV: aqueductal respiratory volume.

Evaluation of pulsatile ICP gradient induced flow for patient-specific geometries

To evaluate our findings for more complicated geometries, we next considered representations of the cerebral aqueduct of three patients diagnosed with iNPH. For each of the three patient-specific 3D geometries, we first simulated the CSF flow and pressure using aqueductal flow rates obtained from PC-MRI as boundary conditions for the incompressible Navier–Stokes equations, and computed the wave characteristics (amplitude and frequency) of the resulting simulated (cardiac) pressure gradients. Next, we added a custom respiratory pressure gradient to each of these simulated cardiac pressure gradients (cf. Methods and below). Finally, we simulated the total (cardiac and respiratory) pressure driven CSF flow in the three patient-specific aqueducts, and computed cardiac and respiratory PVFs, ASVs and ARVs.

Table 3 lists data obtained from PC-MRI for the three patients. The ASVs were measured to be 30.9, 94.7 and 110.4 μL , and the heart rates were 103, 77 and 74 beats per minute. The first simulations, using flow obtained with PC-MRI as input data, gave (cardiac) pressure gradients with pulse amplitudes of 1.65, 4.51 and 2.92 mmHg/m, respectively. Based on the average cardiac-to-respiratory pressure gradient amplitude and frequency ratios (Table 1), respiratory amplitudes were assumed to be 2.85 times smaller, and rates 4.11 times lower. The respiratory pressure gradient amplitudes were thus estimated to be 0.58, 1.58 and 1.02 mmHg/m with rates of 25, 19 and 18 breaths per minute in the three patients.

The sum of these pressure gradients, applied as pressure boundary conditions, induced laminar flow in all three patient-specific geometries, but differing in magnitude and distribution (Fig. 5). The simulated cardiac and respiratory PVF were similar to the flow rates in the simplified model (0.31 ± 0.16 vs 0.29 ± 0.13 mL/s for the cardiac, and 0.32 ± 0.17 vs 0.35 ± 0.13 mL/s for the respiratory PVF (Table 4, Table 2)). Moreover, the simulated ASVs were again dominated by the ARVs: the ASV was 69.9 ± 36.6 μL , and ARV 308.1 ± 204.8 μL . On average, the ratio between cardiac and respiratory components were 0.92 ± 0.23 for cardiac PVF versus respiratory PVF, and 0.24 ± 0.06 for ASV versus ARV (Table 4). We note that the final simulated cardiac PVFs and ASVs were slightly lower than the original (cardiac) PVF and ASV PC-MRI measurements (Table 3 vs Table 4, also illustrated in Fig. 5c).

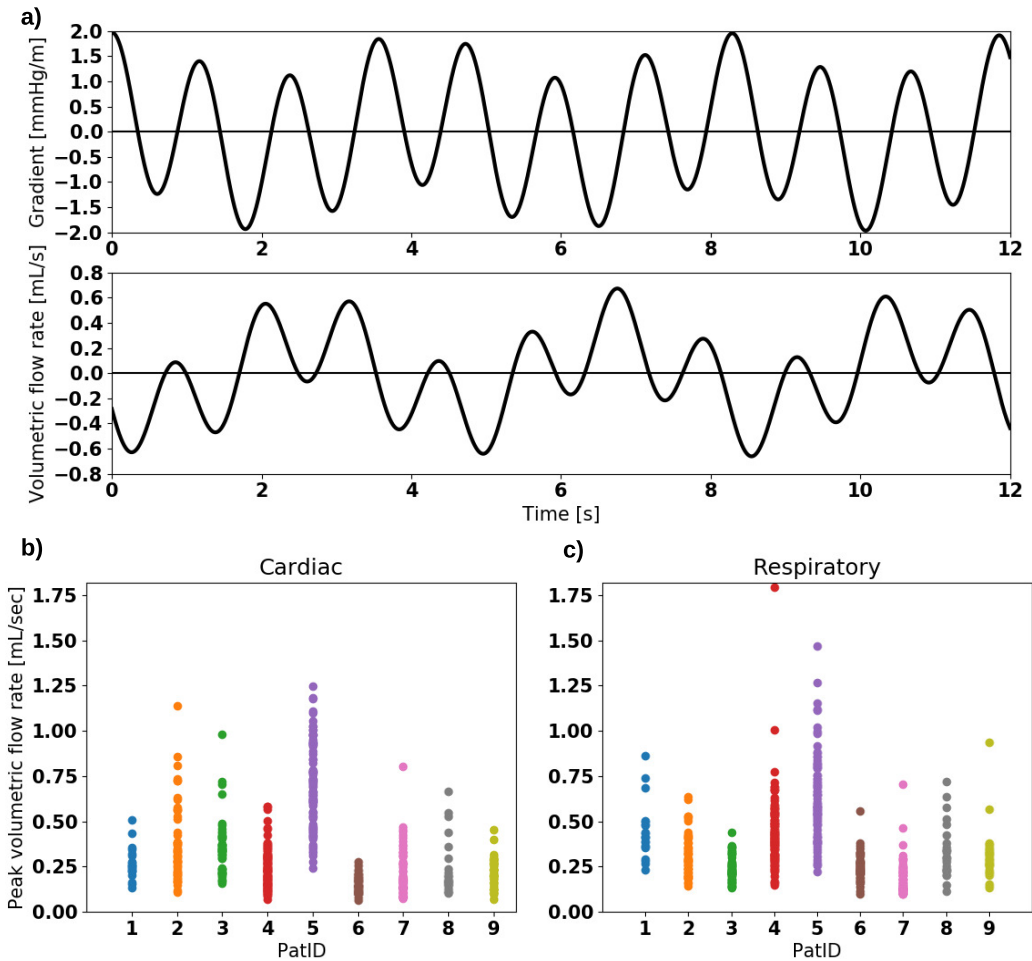


Figure 4. a) Curves demonstrating average simplified pressure gradient and the computed volumetric flow rate through the cerebral aqueduct versus time for patient 2. The respiratory component is more prominent in the flow rate curve. For this patient, the ratio between cardiac and respiratory amplitude was 3.31 for the pressure gradient and 1.27 for the volumetric flow rate. b) Cardiac peak volumetric flow rate for all patients over all time windows. c) Respiratory peak volumetric flow rate for all patients over all time windows.

Comparison of pulsatile and potential static ICP gradient magnitudes

When hydrostatic effects due to body position have been included, some authors have dismissed the idea of a transmante pressure gradient²³. If a net flow according to the third circulation exist, such a transmante pressure gradient need to be present along the aqueduct. To investigate the magnitude of this potential static pressure gradient, we computed the pressure gradient needed to drive flow according to the third circulation.

PatID	Heart rate (beats per minute)	Respiratory rate [#] (breaths per minute)	Cardiac PVF (mL/s)	ASV (μ L)	Cardiac gradient* (mmHg/m)	Respiratory gradient [#] (mmHg/m)	Static gradient* (mmHg/m)
11	103	25	0.16	30.9	1.65	0.58	0.006
13	77	19	0.35	94.7	4.51	1.58	0.015
21	74	18	0.39	110.4	2.92	1.02	0.005
Avg.	85 \pm 16	21 \pm 4	0.30 \pm 0.13	78.7 \pm 42.1	3.03 \pm 1.43	1.06 \pm 0.50	0.009 \pm 0.006

Table 3. Heart rate, cardiac PVF and ASV obtained with data from the previous PC-MRI study. The cardiac induced pressure gradient was computed with computational fluid dynamics. The respiratory rate and gradient were estimated on the assumption that the three patients in the PC-MRI study had the same ratio between the cardiac and respiratory components as the 9 patients included in the dICP analysis. The last row shows average and standard deviation of average values from each individual patient. All values in the table have been rounded after as exact computations as possible. PVF: peak volumetric flow rate. ASV: aqueductal stroke volume. *: estimated from computational fluid dynamics. #: Estimated from average ratios between cardiac and respiratory frequency or gradients from ICP recordings.

PatID	Cardiac PVF (mL/s)	Respiratory PVF (mL/s)	ASV (μ L)	ARV (μ L)	PVF ratio (A_1/A_0)	Ratio ASV/ARV
11	0.14	0.18	28.8	127.1	0.81	0.23
13	0.32	0.27	82.4	266.8	1.17	0.31
21	0.39	0.51	98.6	530.4	0.76	0.19
Avg.	0.29 \pm 0.13	0.32 \pm 0.17	69.9 \pm 36.6	308.1 \pm 204.8	0.92 \pm 0.23	0.24 \pm 0.06

Table 4. Statistics from pulsatile flow computations in the patient-specific geometries. The last row shows average and standard deviation of average values from each individual geometry. All values in the table have been rounded after as exact computations as possible. PVF: peak volumetric flow rate. ASV: aqueductal stroke volume. ARV: aqueductal respiratory volume.

The static pressure gradients that would result in a net flow of 500 mL/day through the cerebral aqueduct, as stipulated by the third circulation, were computed to be 0.009 ± 0.006 mmHg/m for the patient specific geometries (Table 3) and 0.0045 mmHg/m for the simplified geometry, with the latter computed by Poiseuille's law. Thus, the measured pulsatile pressure gradients were approximately two orders of magnitude greater than these static pressure gradient estimates. We further remark that these estimates are five orders of magnitude lower than the pressure increase involved in infusion tests as described by Davson's equation^{29,30}.

Discussion

The relative importance of cardiac and respiratory contributions to ICP and CSF fluid dynamics is not yet well understood. This computational study gives a mechanistic explanation for seemingly disparate experimental findings. In particular, we demonstrate that small cardiac-dominated pulsatile ICP gradients yield CSF peak flow rates with comparable cardiac and respiratory components, and respiratory-dominated aqueductal flow volumes. Compared to the cardiac period, the longer respi-

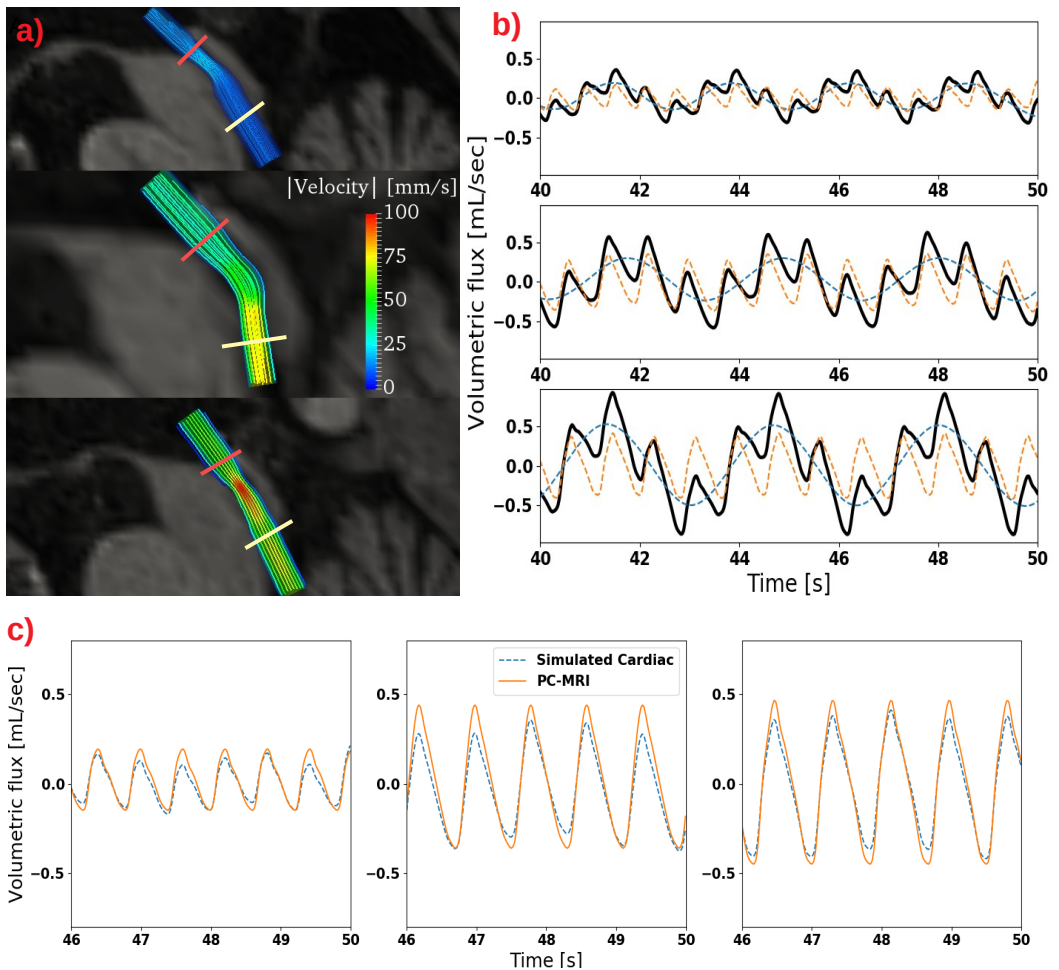


Figure 5. a) Velocity distribution in the patient-specific 3D geometries at the time of peak velocity in all three patients (PatID11, PatID13, PatID21 from top to bottom). Peak velocity, flow rate, and spatial distribution of the flow field differed between the three geometries. Pressure gradients listed in Table 3 were computed in the physical part of the aqueduct, i.e. as a linear approximation between the two slices depicted in red and yellow. b) Volumetric flow rate (black curve) as a function of time also decomposed into its cardiac (orange) and respiratory (blue) component. A prominent respiratory component of the flow pattern is present. c) Comparison of flow rates obtained with PC-MRI with the cardiac component of the flow rate computed from pressure driven flow in the patient-specific geometries. The good agreement is as expected, however in contrast to the simplified model, respiratory pressure gradients may slightly affect cardiac flow due to nonlinearities in Navier-Stokes equations.

ratory period allows momentum from the small respiratory pressure gradient to build up over time. These findings are consistent across both simplified and patient-specific geometries, and based on measurement data from more than 180,000 cardiac cycles and 48,000 respiratory cycles in 9 iNPH patients.

ICP has long been known to be pulsatile, and dominated by the cardiac component³¹. On the other hand, the existence of transmantle and/or intracranial pressure gradients has been much discussed. A transmantle pressure gradient has been proposed to be the mechanism behind enlarged ventricles in iNPH^{22,32}. Stephensen et al.²³ reported that no static transmantle pressure difference exists in iNPH, suggesting alterations in pulsatile rather than static pressure to explain ventricular enlargement. In a fluid-structure interaction model, Linninger et al.³³ argued that pulsatile pressure gradients do not need to be large to produce ventricular enlargement. Our findings are consistent with these reports: our analysis revealed small pulsations also in the ICP difference between the ventricular CSF and subdural compartment, of both cardiac and respiratory origin, and dominated by the cardiac cycle.

The pulsatile ICP gradients were of comparable magnitude as previous analyses of pulsatile ICP measurements^{22,34}. Except for one data point (Table 1, patient 5), pulsatile ICP gradients in our study were well within values (less than 3 mmHg/m) estimated non-invasively with PC-MRI^{25,35}. The recorded pressure differences in our study were slightly higher than what was estimated in a computational model by Sweetman et al (0.03 mmHg vs 0.1 mmHg in our study)²⁷. The ICP gradients computed from the pressure difference signal were of similar magnitude as have been reported from simulations of CSF flow in the foramen magnum: Martin et al.³⁶ used flow data to estimate a pulsatile gradient with a maximum value of 0.67 mmHg/m, while Rutkowska et al.³⁷ used a pulsatile gradient of approximately 3.1 mmHg/m to compute pulsatile CSF flow. In our data, collected from a total of 502 6-minute windows in iNPH patients, ICP gradient variation over time was high compared to a recent MRI-study of healthy controls over four 6-minute windows²⁵. The difference in cohort (iNPH patients vs healthy) and possibly difference in modality (long-term ICP monitoring vs MRI at the craniocervical region) and the total number of observations may explain this discrepancy. It is worth noting that the patient with the highest dICP also had the lowest distance between the two sensors. The distance between the two sensors affects the measured pressure difference, however no clear relationship between the distance between sensors and the computed pressure gradient was found.

In our study, we found the static pressure gradient needed to drive net CSF flow according to the traditional third circulation hypothesis⁵ (corresponding to a CSF production of 500 mL/day) to be extremely small (less than 0.01 mmHg/m), approximately two orders of magnitude lower than the measured pulsatile ICP gradients. Therefore, a transmantle pressure difference close to zero (of the order 0.01 mmHg) as found by Stephensen et al.²³ is sufficient to drive flow of comparable magnitude to CSF production. Accurate measurements of static ICP gradients of this size are hard to obtain in the clinical setting.

That respiration plays a significant role for the CSF flow compares well with recent studies, although the ratio between cardiac and respiration influence varies. Dreha-Kulaczewski et al.¹² previously concluded that inspiration is the major regulator of CSF flow, and later proposed that inspiration-induced downward flow of venous blood is counterbalanced by an upward CSF movement with a respiratory volume of 300 - 600 μL ³⁸. We find ARVs of comparable size, but in contrast to the latter study, we estimated flow during free breathing and not during a breathing protocol. For CSF velocities in the cerebral aqueduct, Takizawa et al.¹⁷ found the cardiac component to be approximately two times greater than the respiratory contribution. Similarly, Yildiz et al.¹³ found a factor two between the cardiac and respiratory components of the velocity in the foramen magnum.

MRI-studies have found CSF displacement to be dominated by respiration: the respiratory compo-

ment has been found to be two to three¹⁷ and three to four³⁹ times greater than the cardiac component. The displacement in these two studies is defined as the time integral of the measured velocity. Therefore, we would expect the ratio between velocity and displacement as measured in these two studies, to compare to the ratio between volumetric flux and volume as analyzed in our study. The computed ratio between ARV and ASV in our study aligns well with the aforementioned findings on CSF displacement.

Our findings on the variation and effect of respiration on aqueductal flow volumes are also interesting in a clinical perspective. The range of average ASVs in our study (in both simplified and patient-specific geometries) is in agreement with earlier findings^{40–42}. We note that, in the simplified model, we found the average standard deviation within a patient over one day to be 39 μL . This is a substantial variation, especially viewed in the context of the potential use of ASV as an indicator for selecting NPH patients for surgical shunting⁴⁰. Intra-patient standard variation of 34 μL in ASV has earlier been shown on the timescale of months⁴², but not on the short timescales provided in our study. A fundamental challenge to the use of ASV derived from cardiac gated PC-MRI may also be the effect of respiration, as respiration is traditionally not controlled for. Our findings show that selecting patients for shunt surgery based on the ASV alone may be inadequate if the pulsatile CSF volume through the cerebral aqueduct is the determining factor for shunt response. If this is the case, the ARV is a factor (at least) as important to consider as the ASV in selection of shunt responders.

ICP gradients of the (small) magnitude reported in this study are in general little studied, difficult to measure reliably, and subject to several potential sources of error. First, the raw data collected from the ICP sensors contained some high frequency noise of magnitude comparable to the physiological pulsation in the pressure gradient. Second, even though the sensors used in this study have been validated with respect to sampling rate⁴³, the pressure differences measured (0.1–0.2 mmHg) are small compared to the amplitudes for which the validation took place (approximately 5 mmHg). Finally, we can not exclude the possibility that systematic differences between pairs of sensors (e.g. differences in sensor sensitivity) could introduce artificial oscillating pressure gradients of comparable magnitude to those reported here. That said, since new sensors are used each time, the systematic difference would only apply to individual investigations and not the group of patients as a whole. Further, these potential errors would directly affect the flow patterns. Clearly, an overestimation (resp. underestimation) of the actual ICP gradients would overestimate (resp. underestimate) flow rates and flow volumes, and likely shift the relative importance of cardiac and respiratory contributions. On the other hand, we argue that the following considerations add confidence to the reported ICP gradients. Our analysis compared 502 6-minute windows with approximately 182,000 cardiac cycles and 48,000 respiratory cycles in total. The large amount of observations gives confidence in the cardiac and respiratory pulsations observed in the pressure difference signal. In addition, we note that the measured pressure gradients are of the same frequency, and of similar amplitude to what has already been found or estimated in the literature in both PC-MR and simulation studies c.f. e.g.^{25,27,28,35–37}. Finally, with regard to potential systematic sensor differences, we find such a difference unlikely to occur consistently in 9 patients over several hours for each patient.

The original data collection did not record body position, thus providing no information on possible hydrostatic transmante pressure gradients. To remedy the lack of information, we applied a shift of the pressure difference, giving it a zero mean value, which has been reported to be the case when body position is taken into account²³. This shift removes any constant-in-time pressure gradients, and in particular hydrostatic transmante pressure gradients. Thus our simulations had no bulk flow, which otherwise would be superimposed on the pulsatile flow, not affecting the outputs measured or computed in this study. Similarly, in this study, we did not analyze other low frequency patterns (of frequency < 0.1 Hz). Small head movements during measurements will cause sudden increase

in the hydrostatic gradient between the two sensors, resulting in energy in the low-frequency region of the Fourier-spectrum. Low frequency components were removed using a fitted exponential function, therefore the respiratory magnitude may be slightly underestimated. As such, our respiratory amplitudes were conservatively estimated.

For the CSF flow simulations, we have assumed that the gradient in the cerebral aqueduct is equal to the measured pulsatile ICP gradient; i.e., the difference in the measured pressure divided by the distance between the sensors. We have thus assumed that the ICP varies linearly throughout the intracranial compartment and is equal in all directions. This stipulation clearly ignores existing heterogeneity in the parenchymal tissue and CSF compartments. On the other hand, pressure gradients in the two patients with sensors placed in the parenchyma instead of in the subdural space (PatID4 and PatID5) did not show any clear discrepancy between gradients from the rest of the cohort. In addition, we note that, under this assumption, the cardiac-induced pressure gradients found from the ICP measurements were similar to the pressure gradients found with CFD in the patient-specific 3D geometries using CSF flow measured with PC-MRI as input (1.46 vs 3.03 mmHg/m). To drive the same amount of flow, the pressure gradients in the narrow part of the aqueduct would be expected to be higher than in the straight tube representing the simplified aqueduct. In addition, we note that the heart rate was higher in the cohort that underwent PC-MRI, possibly affecting the cardiac induced pulsatile gradient amplitude as well. However, on cohort average, the ratio between cardiac and respiratory PVF as well as the ratio between ASV and ARV were almost identical in the simplified and in the patient-specific models

In terms of other limitations, in the simplified flow simulations, the cerebral aqueduct was assumed to be a rigid cylinder, equal in all patients. We note however, that the aqueduct radius differs between individuals, and is typically 1 - 3 mm in healthy⁴⁴, while the median and range were approximately 2 mm, and 1.7 - 3.5 mm, respectively, in a cohort of 21 iNPH patients⁴¹. In earlier computer models, a radius below 1 mm has been used²⁸. An increased radius would directly affect resistance and thus flow rate, ASV and ARV in our model. On the other hand, the relative importance of cardiac versus respiratory effects would be less affected as the Womersley number for both components will be linearly shifted with a change in radius. Possible effects of narrowing, curvature, or other geometrical differences were ignored in the simplified model. However, our findings were robust with regard to changes in geometry: a given ratio between cardiac and respiratory ICP gradients resulted in a similar ratio between cardiac and respiratory-induced flow rates and volumes in all (simplified and patient-specific) geometries. Also, the input pressure gradient was simplified as the sum of two sinusoidal waves representing the cardiac and respiratory cycle in the simplified model. Moreover, geometries and pressure recordings were obtained from iNPH patients only, where aqueductal flow may be hyperdynamic⁴⁰.

In the patient-specific geometries, the time varying inlet boundary condition was assumed to be a function constant in space. However, the flow extensions ensured that flow had developed before reaching the narrow parts of the aqueduct. In the simulations, we also verified that the solutions were independent of the stabilization parameter, time-step and element size in the mesh: a 50 % reduction in either of these parameters resulted in less than 2 % change in peak volumetric flow rate.

For the categorization of sleeping versus awake states, we did not monitor whether the patients were actually sleeping at nighttime, but rather assumed a sleeping state at night hours. Thus, our quantification of differences between sleeping and awake states likely combined the effects of sleep and the sleep-independent circadian rhythm.

In conclusion, we have demonstrated, via fundamental mechanics and computational modelling, how a relatively small respiratory-induced ICP gradient pulsation induced flow volumes that dominated the cardiac component in the cerebral aqueduct. Our study supports the notion that respiration

contributes substantially to CSF flow, and suggests that respiration should be investigated as a potential driver of other forms of intracranial fluid flow such as e.g. paravascular flow or potential lymphatic circulation^{45,46}.

Methods

Approvals

The simultaneous ICP measurements were performed in a study approved by The Regional Committee for Medical and Health Research Ethics (REK) of Health Region South-East, Norway (approval no. S-08670b) and the Institutional Review Board of Oslo University Hospital – Rikshospitalet (no. 08/6827). Patients were included after written and oral informed consent.

For acquisitions of PC-MRI and patient specific geometries (T1-weighted volume scans), approval was retrieved by the Regional Committee for Medical and Health Research Ethics (REK) of Health Region South-East, Norway (2015/96) and the Institutional Review Board of Oslo University Hospital (2015/1868) and the National Medicines Agency (15/04932-7).

All methods were performed in accordance with the relevant guidelines and regulations.

Intracranial pressure monitoring and acquisition

In the Department of Neurosurgery at Oslo University Hospital – Rikshospitalet, overnight ICP monitoring is part of a standardized pre-operative protocol for iNPH patients. The results of ICP monitoring are among the criteria deciding which patients that are offered shunt surgery². Measurements from two ICP sensors were part of a research protocol. In 10 iNPH patients, simultaneous ICP measurements were obtained overnight from two ICP sensors (Codman ICP microsensor, Raynham, MA, USA) within the intracranial compartment. In all patients, one sensor was placed within the lateral ventricle (ICP_{IV}). In eight patients, the other sensor was placed in the subdural compartment (ICP_{SD}) while in two patients (PatID4 and PatID5) it was placed in the parenchyma (ICP_{PAR}). For further information on sensor placement, see the previous description²². The pressure sensors were placed in local anesthesia with the patient in the operating room. Following a small straight incision in the right frontal region of the head, a burr hole about 1 to 1.5 cm was made. Thereafter, a minor incision was made in the dura. An external ventricular drain (EVD) with a built-in Codman ICP MicroSensor (Codman external drainage with ICP sensor; Codman/Johnson & Johnson, Raynham, MA, USA) was placed within the frontal horn of the cerebral ventricles. The distal end of the EVD was placed at the level of foramen Monroi. Through the same burr hole, another Codman ICP MicroSensor (Codman, Johnson & Johnson, Raynham, MA, USA) was also placed between the arachnoidea and the dura. Both sensors were zeroed before implantation. The burr hole opening was closed with bone wax in order to avoid CSF leakage. When the patient had returned to the neurosurgical ward, the Codman ICP sensors were connected to Codman ICP Express (Codman/Johnson & Johnson, Raynham, MA, USA) and the continuous analogue ICP signals provided by Codman ICP Express were digitalized using the analogue-digital converter (Sensometrics Pressure Logger, Sensometrics software, dPCom, Oslo, Norway). Both continuous digital ICP signals were sampled simultaneously with identical time reference at a sampling rate of 200 Hz, and stored as rawdata files, using Sensometrics software. The sampling rate is sufficient for accurate assessment of ICP waveforms⁴⁷. All patients undergoing ICP monitoring were breathing freely and not on artificial respiration.

MRI acquisition

The MRI study consisted of three iNPH patients (PatID11, PatID13, PatID21) and was obtained for study purposes during the pre-operative protocol. From the three patients, we obtained T1-weighted

images (used for mesh-construction) and PC-MRI to obtain cardiac-gated CSF flow. Details on the T1-weighted image and the PC-MRI acquisitions, the segmentation and mesh generation based on the T1-weighted images, and the post-processing of the PC-MRI images to obtain the time-varying flux are given in the Supplementary Material. The PC-MRI post-processing has also previously been described in detail¹⁴.

Differential intracranial pressure analysis

We computed the ICP gradient (dICP) waveform as a function over time by the difference between the two pressure signals divided by the distance L between the sensors: $dICP = (ICP_{SD} - ICP_{IV})/L$. In the two patients with sensor placement in the parenchyma, the dICP was defined as $dICP = (ICP_{PAR} - ICP_{IV})/L$. To assess time variability within each patient, we extracted sets of 6-minute windows of the dICP waveforms. Six minutes is the typical duration of a cardiac-gated PC-MRI scan. A 6-minute window was accepted if the maximal variability in the pressure difference was less than 2 mmHg over the 6-minute window. As body position was not recorded, hydrostatic pressure may contribute to static pressure differences between the two sensors. To compensate, the dICP waveform was shifted to have zero mean within each 6-minute window.

For each dICP waveform 6-minute window, we computed its power spectrum using the fast Fourier transform to identify and quantify the dominant frequencies and amplitudes. A low-pass filter with cutoff frequency 15 Hz was applied to the power spectrum of the dICP waveform. The cardiac amplitude was defined as the peak between 0.7 and 1.6 Hz (42-96 beats per minute), while the respiratory amplitude was defined as the peak between 0.15 and 0.4 Hz (9-24 breaths per minute). For each patient, we extracted cardiac and respiratory amplitudes and the corresponding frequencies for all 6-minute windows associated with the given patient.

The power spectrum of the 6-minute windows of the dICP waveform also revealed low frequency (less than 0.1 Hz) patterns. We modeled the low frequency patterns as a decreasing exponential function fitted to the power spectrum function and subtracted this function from the original power spectrum for all 6-minute windows.

Categorization of sleeping versus awake state

All 6-minute time windows were categorized as belonging to either the sleeping or awake state based on the time of recording: all windows between midnight and 06:00 am as sleeping, and all others as awake.

Pulsatile CSF flow in a cylindrical geometry

To model CSF flow induced by the dICP in a simplified model of the cerebral aqueduct, we solved the incompressible Navier-Stokes equations with the dICP as a driving force. We modelled a simplified cerebral aqueduct as a rigid cylinder with radius $R = 2$ mm, with radial size motivated by a median cerebral aqueduct area of 14 mm^2 in iNPH patients⁴¹. Under these assumptions, the incompressible Navier-Stokes equations reduce to a one-dimensional differential equation⁴⁸:

$$\rho \frac{\partial v}{\partial t}(r, t) - \frac{\mu}{r} \frac{\partial v}{\partial r}(r, t) - \mu \frac{\partial^2 v}{\partial r^2}(r, t) = -\frac{dp}{dz}(t). \quad (1)$$

Here, v is the radially-varying velocity in the z -direction along the cerebral aqueduct for $0 \leq r \leq R$, and time $0 \leq t \leq T$ for some final simulation time T , $\frac{dp}{dz}$ is the pressure gradient along the cerebral aqueduct (Pa/m), and ρ and μ are CSF density and viscosity, respectively.

For each 6-minute time window, we expressed the simplified pressure gradient as

$$\frac{dp}{dz}(t) = a_0 \sin(2\pi t f_0) + a_1 \sin(2\pi t f_1). \quad (2)$$

with frequencies f_0 and f_1 and amplitudes a_0 and a_1 . We identified f_0 and f_1 as the frequency of the cardiac and respiratory peak in the dICP frequency spectrum, respectively. It has previously been shown that ICP amplitudes extracted directly from peak values in the frequency domain would underestimate amplitudes in the time domain⁴⁷. To compensate, we multiplied the amplitudes extracted from the power spectrum by a factor C to compute the amplitudes in equation (2). A factor $C = 7$ was chosen heuristically to obtain time domain amplitudes of comparable size as the original raw signal (see Fig. 2d). This scaling does not affect the ratio between the cardiac and respiratory component in the dICP signal. We labeled f_0 and a_0 as the cardiac frequency and cardiac dICP amplitude, and f_1 and a_1 as the respiratory frequency and respiratory dICP amplitude.

The solution to equation (1) with a sinusoidal pressure gradient of amplitude a and frequency f can be calculated analytically⁴⁹. The analytical flow rate is given by

$$Q(t) = Re \left\{ \pi r^2 \frac{i a}{\rho \omega} \left[1 - \frac{2 J_1(\Lambda)}{\Lambda J_0(\Lambda)} \right] e^{i\omega t} \right\} \quad (3)$$

where r is the radius of the cylinder, a is the pressure gradient amplitude, $\omega = 2\pi f$ is the angular frequency of the pressure gradient, and $\Lambda = \alpha i^{3/2}$, where $\alpha = r(\frac{\omega \rho}{\mu})^{1/2}$ is the Womersley number and $i = \sqrt{-1}$. J_0 and J_1 are Bessel Functions of the first kind with order zero and one, respectively. The corresponding peak volumetric flux (PVF), is thus given by the amplitude of the signal:

$$A = \left| \pi r^2 \frac{i a}{\rho \omega} \left[1 - \frac{2 J_1(\Lambda)}{\Lambda J_0(\Lambda)} \right] \right|. \quad (4)$$

By the linearity of equation (1), the pressure gradient from equation (2) will result in a sum of two flow rate functions with frequencies f_0 and f_1 , and corresponding PVFs, A_0 and A_1 , each given by equation (4).

For all 6-minute time windows in all patients, we used equation (4), with cardiac frequency f_0 and respiratory frequency f_1 as separate inputs, to compute the cardiac (A_0) and respiratory PVF (A_1). We further defined the cardiac component of the aqueductal flow volume - the aqueductal stroke volume (ASV), and the aqueductal respiratory flow volume (ARV) as V_0 and V_1 respectively, where

$$V_i = \int_0^{\frac{1}{2f_i}} A_i \sin(2\pi t f_i) dt = \frac{A_i}{\pi f_i}. \quad (5)$$

for $i = 0, 1$.

PC-MRI guided CSF flow in patient-specific 3D geometries

Three patient-specific geometries were constructed using the software VMTK (1.4.0)⁵⁰ together with MR images of patients diagnosed with iNPH (see also Section on MRI acquisition above). The process is described in the Supplementary Material, and visualized in Supplementary Fig. S2. Flow extensions were added to each end of the aqueduct geometry to minimize the effect of the choice of spatial inlet velocity profile, such that the flow was developed when it reached the narrow part of the aqueduct. The flow extensions were constructed by computing the center-lines from the inlet to the outlet, and adding cylinder extensions in the direction of the center-lines.

The following steps were then carried out for each of the three patient-specific geometries. To first estimate patient-specific pulsatile pressure gradients, given the PC-MRI flow rate measurements, we computed an inlet velocity by dividing the volumetric flow rates obtained from the PC-MRI by the inlet area of the patient-specific geometry. The PC-MRI flow data also revealed the cardiac frequency f_0 in each case. We subsequently solved the 3D incompressible Navier-Stokes equations (in Cartesian coordinates) over the geometry with this time-varying velocity prescribed at the inlet, no-slip conditions at the rigid outer walls, and a zero pressure (pseudo-traction) condition at the outlet. The system started at rest, and the end time was $T = 50$ s with a time step of $\Delta t = 0.01$ s. The equations were solved simultaneously for the CSF velocity and pressure with linear finite elements with a stabilization term on the mass conservation equation, using the FEniCS finite element software⁵¹. Results from the last 10 seconds of the simulations were used for post-processing, allowing for at least one full respiratory period.

From the first set of simulations, pressure gradients in the patient specific geometries were computed in the physical aqueduct, excluding the flow extensions as shown in Fig. 5 (and Supplementary Fig. S2). The resulting pressure difference between the two slices defining the physical part of the aqueduct was divided by the length of the aqueduct (center-line) L , $dp_0(t) = \frac{1}{L}(p_{in}(t) - p_{out}(t))$ to compute the cardiac induced pressure gradient. The amplitude of the cardiac pressure gradient was then computed as $a_0 = \frac{1}{2}(\max(dp_0(t)) - \min(dp_0(t)))$. Given the pulsatile cardiac-induced pressure gradient, we computed a representative sinusoidal respiratory component $dp_1(t) = a_1 \sin(2\pi f_1 t)$ with frequency $f_1 = \beta f_0$ and amplitude $a_1 = \alpha a_0$. We let $\beta = 1/4.11$ and $\alpha = 1/2.85$ based on cardiac versus respiratory analysis of the ICP measurement cohort (cf. Table 1).

To investigate whether a given ratio between cardiac and respiratory pressure gradients would result in a given ratio between cardiac and respiratory flow, regardless of small changes in the geometry, we next computed pressure driven flow in the patient-specific models. To simulate pressure driven flow, the pressure difference between the inlet and outlet of the geometry, including flow extensions, are needed. Therefore, in addition to the pressure gradient in the physical aqueduct, we also computed the pressure difference between the inlet and outlet of the full geometry in the first set of simulations. Next, we again assumed the corresponding respiratory pressure difference to be a sinusoidal curve with 2.85 times smaller amplitude and frequency 4.11 times lower than the cardiac pressure difference. Finally, in the second set of simulations we prescribed the sum of the cardiac and respiratory pressure difference between the inlet and outlet as boundary conditions.

For the patient-specific geometries and simulations, we obtained the patients' heart rate, PVF and ASV from the relevant PC-MRI (Table 3). When pressure driven flow was simulated, the volumetric flow rate Q , as a function of time, was calculated by integrating the velocity over the cross-section of the cerebral aqueduct at the outlet. To separate the respiratory and cardiac components of the flow rate curve, we defined the following procedure. We first defined all peaks and valleys of the flow rate curve $Q(t)$ for the last 10 seconds of the simulation. For each pair (Q_p, Q_v) of peak and valley, we defined points $(Q_p + Q_v)/2$, and defined the respiratory volumetric flow rate function $Q_r(t)$ as a continuous interpolant of these points (see e.g. blue curves in Fig. 5). The cardiac component was then defined as the difference between the volumetric flow rate and its respiratory component, $Q_c(t) = Q(t) - Q_r(t)$. The cardiac and respiratory PVFs were then defined as $(\max(Q_i(t)) - \min(Q_i(t)))/2$ for $i=c,r$. The ASV and ARV were computed by solving

$$[ASV, ARV] = \frac{1}{N^i} \int_{t_0^i}^{t_1^i} \frac{|Q_i(t)|}{2} dt \quad \text{for } i=c,r \quad (6)$$

where t_0^c is the time of the first cardiac peak during the last 10 seconds, t_1^c is the time of the last cardiac

peak, and N_c is the number of full cardiac cycles over the last 10 seconds. t_0^r , t_1^r and N^r are defined analogously for the respiratory cycle. We used the trapezoidal rule for numerical integration in time to compute the ARV and ASV given by equation (6).

Static pressure gradients

In all geometries, we also computed the static pressure gradient involved in the third circulation⁵; i.e., the pressure gradient required to drive a net CSF flow of 500 mL/day⁵² through the cerebral aqueduct. In the simplified model, the pressure gradient was calculated by Poiseuille's law. In the patient-specific models, we computed the pressure gradient in the aqueduct by solving Stokes equation with a constant inlet velocity corresponding to a net flow of 500 mL/day. The static pressure gradient for each geometry was computed in the physical part of the aqueduct, not including flow extensions, as described in the previous subsection.

Data availability statement

The datasets analyzed in the current study are available from the corresponding author upon request.

References

1. Matsumae, M. *et al.* Research into the physiology of cerebrospinal fluid reaches a new horizon: intimate exchange between cerebrospinal fluid and interstitial fluid may contribute to maintenance of homeostasis in the central nervous system. *Neurol. medico-chirurgica* **56**, 416–441 (2016).
2. Eide, P. K. & Sorteberg, W. Diagnostic intracranial pressure monitoring and surgical management in idiopathic normal pressure hydrocephalus: A 6-year review of 214 patients. *Neurosurgery* **66**, 80–91 (2010).
3. Jessen, N. A., Munk, A. S. F., Lundgaard, I. & Nedergaard, M. The glymphatic system: a beginner's guide. *Neurochem. research* **40**, 2583–2599 (2015).
4. Wagshul, M. E., Eide, P. K. & Madsen, J. R. The pulsating brain: a review of experimental and clinical studies of intracranial pulsatility. *Fluids Barriers CNS* **8**, 5 (2011).
5. Cushing, H. *et al.* The third circulation and its channels. *Lancet* **2**, 851–857 (1925).
6. Orešković, D., Radoš, M. & Klarica, M. Role of choroid plexus in cerebrospinal fluid hydrodynamics. *Neuroscience* **354**, 69–87 (2017).
7. Kapoor, K. G., Katz, S. E., Grzybowski, D. M. & Lubow, M. Cerebrospinal fluid outflow: an evolving perspective. *Brain research bulletin* **77**, 327–334 (2008).
8. Xie, L. *et al.* Sleep drives metabolite clearance from the adult brain. *science* **342**, 373–377 (2013).
9. Elvsåshagen, T. *et al.* Cerebral blood flow changes after a day of wake, sleep, and sleep deprivation. *NeuroImage* **186**, 497–509 (2019).
10. Greitz, D., Franck, A. & Nordell, B. On the pulsatile nature of intracranial and spinal CSF-circulation demonstrated by MR imaging. *Acta radiologica* **34**, 321–328 (1993).
11. Enzmann, D. & Pelc, N. Normal flow patterns of intracranial and spinal cerebrospinal fluid defined with phase-contrast cine MR imaging. *Radiology* **178**, 467–474 (1991).
12. Dreha-Kulaczewski, S. *et al.* Inspiration is the major regulator of human CSF flow. *J. Neurosci.* **35**, 2485–2491 (2015).

13. Yildiz, S. *et al.* Quantifying the influence of respiration and cardiac pulsations on cerebrospinal fluid dynamics using real-time phase-contrast MRI. *J. Magn. Reson. Imaging* **46**, 431–439 (2017).
14. Lindstrøm, E. K., Ringstad, G., Mardal, K.-A. & Eide, P. K. Cerebrospinal fluid volumetric net flow rate and direction in idiopathic normal pressure hydrocephalus. *NeuroImage: Clin.* **20**, 731–741 (2018).
15. Spijkerman, J. M. *et al.* Phase contrast MRI measurements of net cerebrospinal fluid flow through the cerebral aqueduct are confounded by respiration. *J. Magn. Reson. Imaging* (2018).
16. Klose, U., Strik, C., Kiefer, C. & Grodd, W. Detection of a relation between respiration and CSF pulsation with an echoplanar technique. *J. Magn. Reson. Imaging* **11**, 438–444 (2000).
17. Takizawa, K., Matsumae, M., Sunohara, S., Yatsushiro, S. & Kuroda, K. Characterization of cardiac- and respiratory-driven cerebrospinal fluid motion based on asynchronous phase-contrast magnetic resonance imaging in volunteers. *Fluids Barriers CNS* **14**, 25 (2017).
18. Lindstrøm, E. K. *et al.* Magnitude and direction of aqueductal cerebrospinal fluid flow: large variations in patients with intracranial aneurysms with or without a previous subarachnoid hemorrhage. *Acta neurochirurgica* **161**, 247–256 (2019).
19. Balédent, O., Czosnyka, Z. & Czosnyka, M. “bucket” cerebrospinal fluid bulk flow—is it a fact or a fiction? *Acta neurochirurgica* **161**, 257–258 (2019).
20. Czosnyka, M. & Pickard, J. D. Monitoring and interpretation of intracranial pressure. *J. Neurol. Neurosurg. & Psychiatry* **75**, 813–821 (2004).
21. Eide, P. K. & Sorteberg, W. Outcome of surgery for idiopathic normal pressure hydrocephalus: role of preoperative static and pulsatile intracranial pressure. *World neurosurgery* **86**, 186–193 (2016).
22. Eide, P. K. & Sæhle, T. Is ventriculomegaly in idiopathic normal pressure hydrocephalus associated with a transmantle gradient in pulsatile intracranial pressure? *Acta neurochirurgica* **152**, 989–995 (2010).
23. Stephensen, H., Tisell, M. & Wikkelsö, C. There is no transmantle pressure gradient in communicating or noncommunicating hydrocephalus. *Neurosurgery* **50**, 763–773 (2002).
24. Bardan, G., Plouraboué, F., Zagzoule, M. & Baledent, O. Simple patient-based transmantle pressure and shear estimate from cine phase-contrast MRI in cerebral aqueduct. *IEEE Transactions on Biomed. Eng.* **59**, 2874–2883 (2012).
25. Ringstad, G. *et al.* Non-invasive assessment of pulsatile intracranial pressure with phase-contrast magnetic resonance imaging. *PloS one* **12**, e0188896 (2017).
26. Fin, L. & Grebe, R. Three dimensional modeling of the cerebrospinal fluid dynamics and brain interactions in the aqueduct of sylvius. *Comput. methods biomechanics biomedical engineering* **6**, 163–170 (2003).
27. Sweetman, B., Xenos, M., Zitella, L. & Linninger, A. A. Three-dimensional computational prediction of cerebrospinal fluid flow in the human brain. *Comput. biology medicine* **41**, 67–75 (2011).
28. Jacobson, E., Fletcher, D., Morgan, M. K. & Johnston, I. Computer modelling of the cerebrospinal fluid flow dynamics of aqueduct stenosis. *Med. & biological engineering & computing* **37**, 59–63 (1999).

29. Andersson, N., Malm, J., Bäcklund, T. & Eklund, A. Assessment of cerebrospinal fluid outflow conductance using constant-pressure infusion—a method with real time estimation of reliability. *Physiol. measurement* **26**, 1137 (2005).
30. McComb, J., Davson, H. & Hollingsworth, J. Further studies on the difference between ventricular and subarachnoid perfusion. *Brain research* **89**, 81–91 (1975).
31. Avezaat, C., Van Eijndhoven, J. & Wyper, D. Cerebrospinal fluid pulse pressure and intracranial volume-pressure relationships. *J. Neurol. Neurosurg. & Psychiatry* **42**, 687–700 (1979).
32. Greitz, D. Radiological assessment of hydrocephalus: new theories and implications for therapy. *The neuroradiology journal* **19**, 475–495 (2006).
33. Linninger, A. A. *et al.* Pulsatile cerebrospinal fluid dynamics in the human brain. *IEEE Transactions on Biomed. Eng.* **52**, 557–565 (2005).
34. Eide, P. K. Demonstration of uneven distribution of intracranial pulsatility in hydrocephalus patients. *J. neurosurgery* **109**, 912–917 (2008).
35. Matsumae, M., Hirayama, A., Atsumi, H., Yatsushiro, S. & Kuroda, K. Velocity and pressure gradients of cerebrospinal fluid assessed with magnetic resonance imaging. *J. neurosurgery* **120**, 218–227 (2014).
36. Martin, B. A. *et al.* Hydrodynamic and longitudinal impedance analysis of cerebrospinal fluid dynamics at the craniovertebral junction in type I Chiari malformation. *PLoS one* **8**, e75335 (2013).
37. Rutkowska, G., Haughton, V., Linge, S. & Mardal, K.-A. Patient-specific 3d simulation of cyclic csf flow at the craniocervical region. *Am. J. Neuroradiol.* (2012).
38. Dreha-Kulaczewski, S. *et al.* Identification of the upward movement of human CSF in vivo and its relation to the brain venous system. *J. Neurosci.* **37**, 2395–2402 (2017).
39. Yamada, S. *et al.* Influence of respiration on cerebrospinal fluid movement using magnetic resonance spin labeling. *Fluids barriers CNS* **10**, 36 (2013).
40. Bradley Jr, W. G. *et al.* Normal-pressure hydrocephalus: evaluation with cerebrospinal fluid flow measurements at MR imaging. *Radiology* **198**, 523–529 (1996).
41. Ringstad, G., Emblem, K., Geier, O., Alperin, N. & Eide, P. Aqueductal stroke volume: comparisons with intracranial pressure scores in idiopathic normal pressure hydrocephalus. *Am. J. Neuroradiol.* **36**, 1623–1630 (2015).
42. Scollato, A. *et al.* Changes in aqueductal CSF stroke volume in shunted patients with idiopathic normal-pressure hydrocephalus. *Am. J. Neuroradiol.* **30**, 1580–1586 (2009).
43. Holm, S. & Eide, P. K. Impact of sampling rate for time domain analysis of continuous intracranial pressure (ICP) signals. *Med. engineering & physics* **31**, 601–606 (2009).
44. Haines, D. & Mihailoff, G. An overview of the brainstem. *Fundamental Neurosci. for Basic Clin. Appl. Fourth Ed. Elsevier, Philadelphia, PA* 140–143 (2012).
45. Mestre, H., Kostrikov, S., Mehta, R. I. & Nedergaard, M. Perivascular spaces, glymphatic dysfunction, and small vessel disease. *Clin. Sci.* **131**, 2257–2274 (2017).
46. Kiviniemi, V. *et al.* Ultra-fast magnetic resonance encephalography of physiological brain activity-glymphatic pulsation mechanisms? *J. Cereb. Blood Flow & Metab.* **36**, 1033–1045 (2016).

47. Holm, S. & Eide, P. K. The frequency domain versus time domain methods for processing of intracranial pressure (ICP) signals. *Med. engineering & physics* **30**, 164–170 (2008).
48. Langlois, W. E. & Deville, M. O. *Slow Viscous Flow*, vol. 105 (Springer, 1964).
49. Womersley, J. R. Method for the calculation of velocity, rate of flow and viscous drag in arteries when the pressure gradient is known. *The J. physiology* **127**, 553–563 (1955).
50. Antiga, L. *et al.* An image-based modeling framework for patient-specific computational hemodynamics. *Med. & biological engineering & computing* **46**, 1097 (2008).
51. Logg, A., Mardal, K.-A. & Wells, G. *Automated solution of differential equations by the finite element method: The FEniCS book*, vol. 84 (Springer Science & Business Media, 2012).
52. Sakka, L., Coll, G. & Chazal, J. Anatomy and physiology of cerebrospinal fluid. *Eur. annals otorhinolaryngology, head neck diseases* **128**, 309–316 (2011).

Acknowledgements

This work was supported by the Research Council of Norway under the FRINATEK Young Research Talents Programme through project #250731/F20 (Waterscape)

Author contributions statement

V.V., M.E.R., K.A.M., P.K.E, G.R. conceived the experiments. V.V. conducted the experiments and analyzed the results. L.M.V. created patient-specific geometries. E.L. performed PC-MRI flow analysis. V.V., G.R. K.A.M., M.E.R. and P.K.E. wrote the paper. V.V., M.E.R. and L.M.V. created the figures. All authors reviewed the manuscript.

Additional information

Competing interests The authors declare no competing interest.

Supplementary Material

Respiratory influence on cerebrospinal fluid flow – A computational study based on long-term intracranial pressure measurements

Vegard Vinje^{1,*}, Geir Ringstad^{2,5}, Erika Kristina Lindstrøm⁴, Lars Magnus Valnes⁴, Marie E. Rognes¹,

Per Kristian Eide^{2,3}, and Kent-Andre Mardal^{1,4}

¹Department of Scientific Computing and Numerical Analysis, Simula Research Laboratory, 1325 Lysaker, Norway.

²Institute of Clinical Medicine, Faculty of Medicine, University of Oslo, 0315 Oslo, Norway.

³Department of Neurosurgery, Oslo University Hospital - Rikshospitalet, 0372 Oslo, Norway.

⁴Department of Mathematics, University of Oslo, 0315 Oslo, Norway.

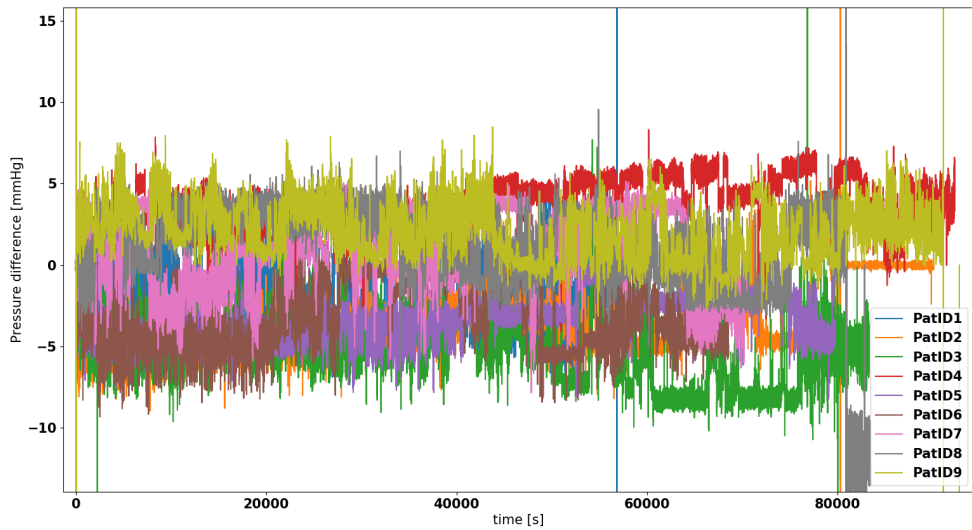
⁵Department of Radiology and Nuclear Medicine, Oslo University Hospital - Rikshospitalet, 0372 Oslo, Norway.

*vegard@simula.no

Results:

Raw data

Supplementary Figure S1 shows the difference between subdural and ventricular pressure in all 9 patients. Whether the transmante pressure difference is negative or positive varies from patient to patient, and in some patients over time.

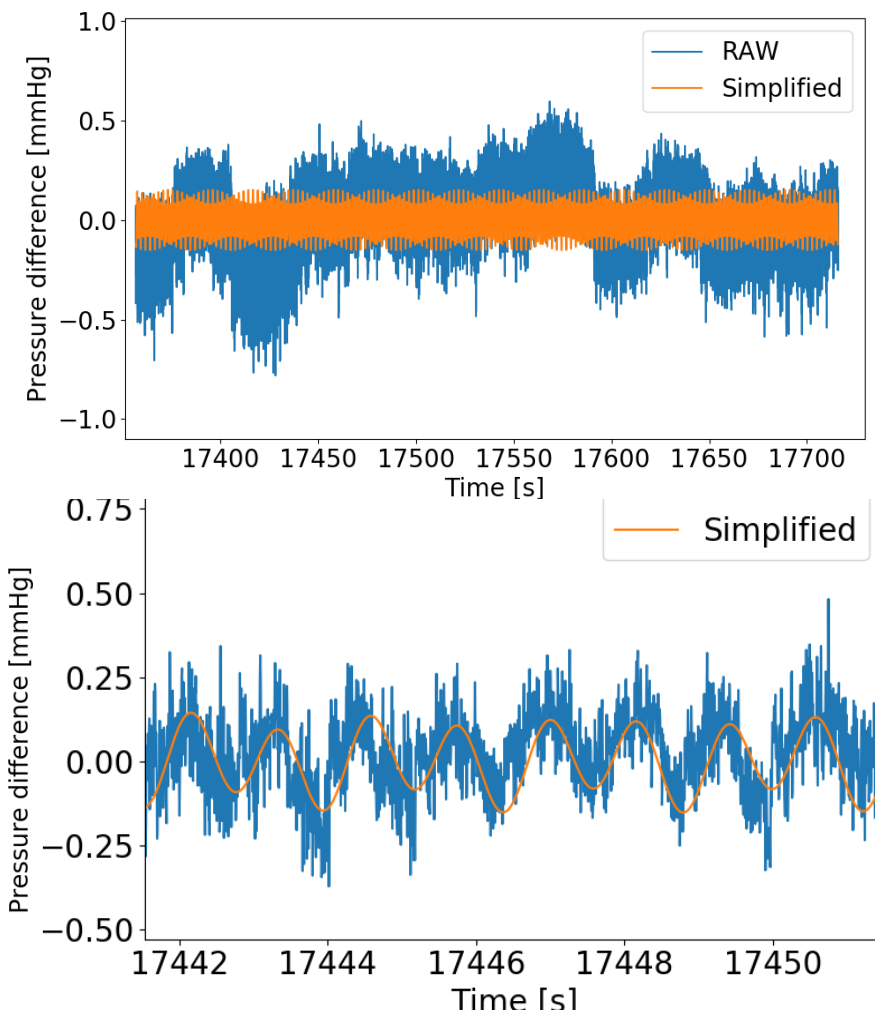


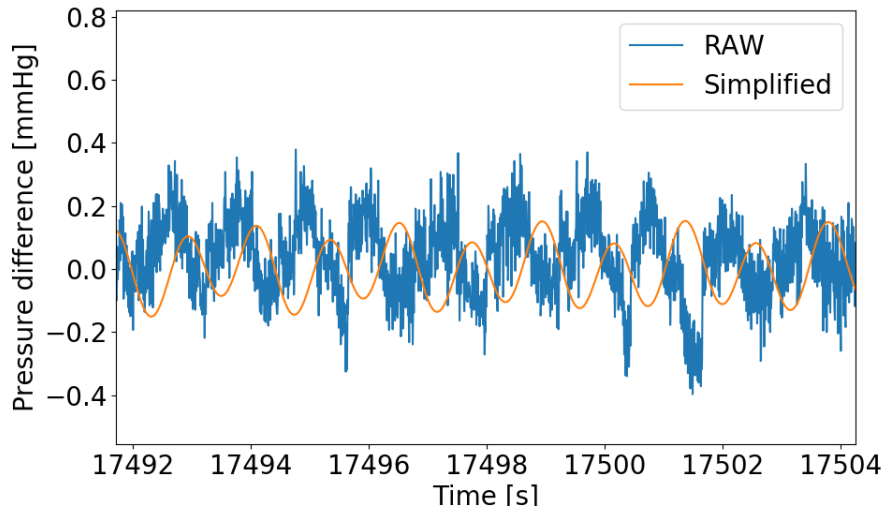
Supplementary Figure S1: Pressure differences for all patients over the entire period of ICP monitoring. Pressure difference curves do sudden shifts in time, possible due to head movements, shifting the relative hydrostatic pressure between the two sensors. This shift should not affect the pressure difference amplitude.

Examples of Extracted 6-minute windows (time series)

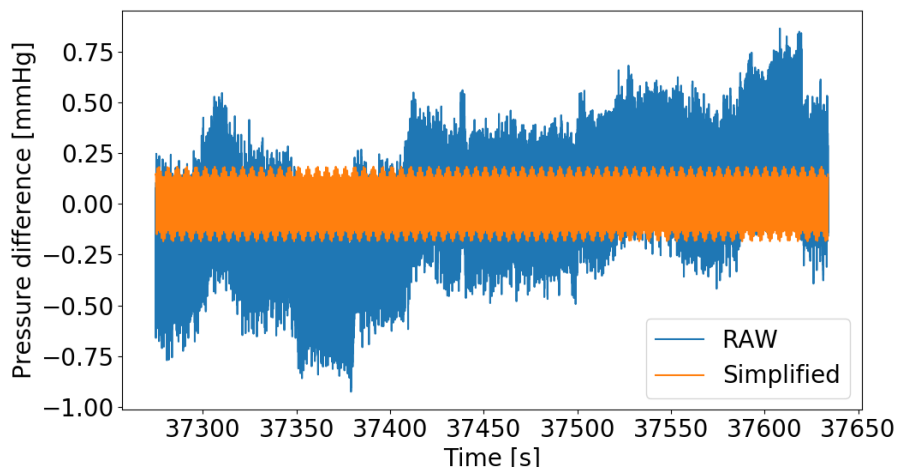
In the paper, an example was provided for patient 1. In the following, we provide examples from 6 minute-windows of raw data compared with the simplified curve from all other patients. Windows were chosen such that there were periods of both good and bad fit within the 6-minute window. Amplitudes and frequencies of the simplified curve will not match exactly with the raw data at each point in time, as the simplified curve is generated by taking the average amplitudes and frequencies over the 6-minute window. We show here three figures for each patient. The first figure for each patient is an overview of a 6 minute window. The second figure zooms in at a shorter period where the simplified curve is a good approximation to the raw data, both in frequencies, phase, and amplitudes. The third figure shows short periods where the pressure difference is out of phase (e.g. Patient 2), overestimated (e.g. Patient 3), underestimated (e.g. Patient 4) or a problem occurs due to a small jump in pressure difference (e.g. Patient 8). It should be noted that amplitude and frequency are the only parameters used to compute flow, and are thus the most important to accurately model with the simplified curves.

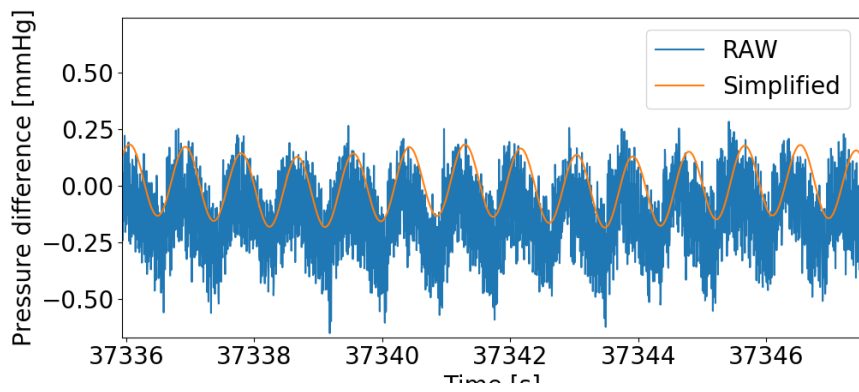
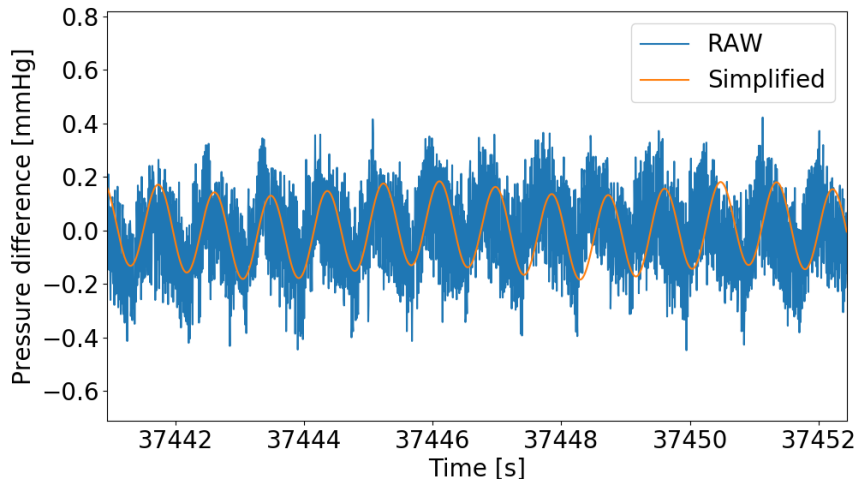
Patient 2



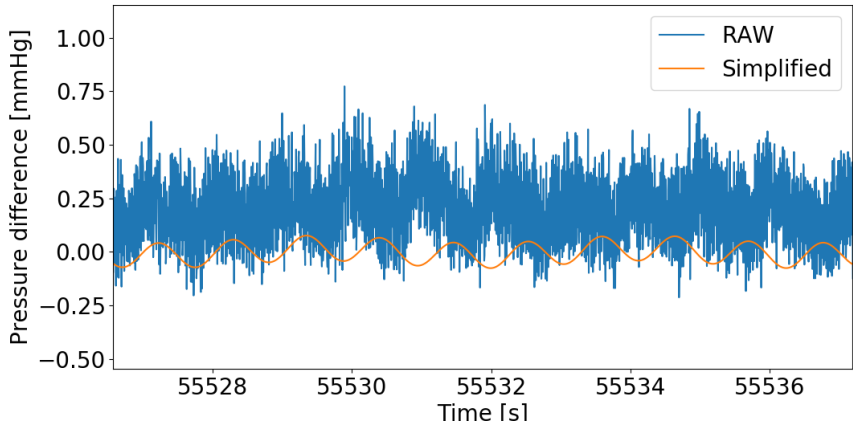
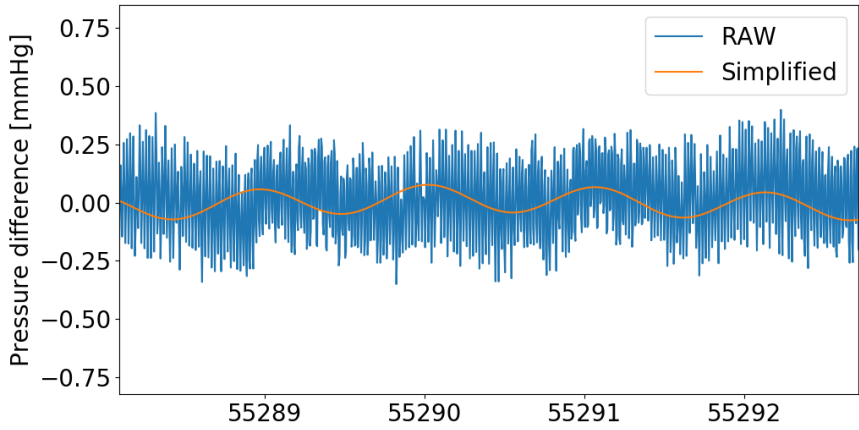
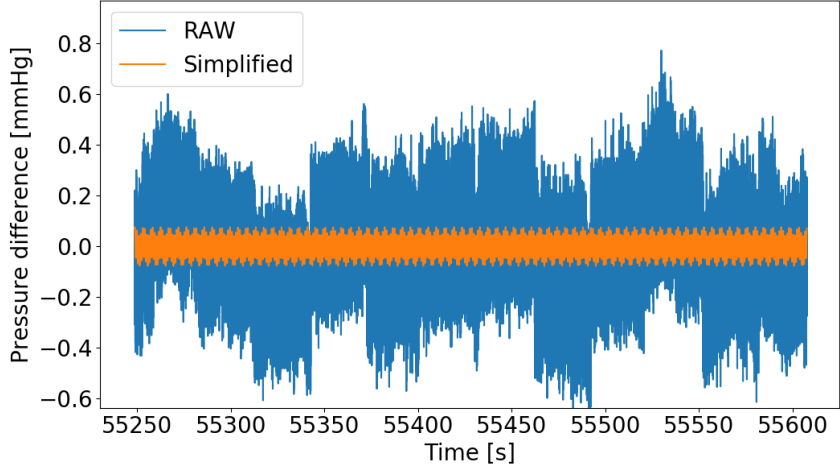


Patient 3

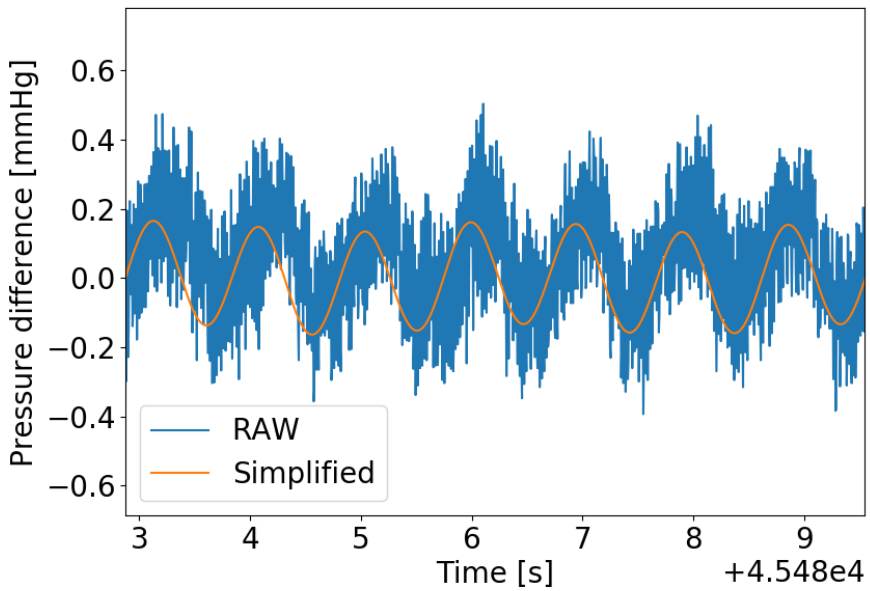
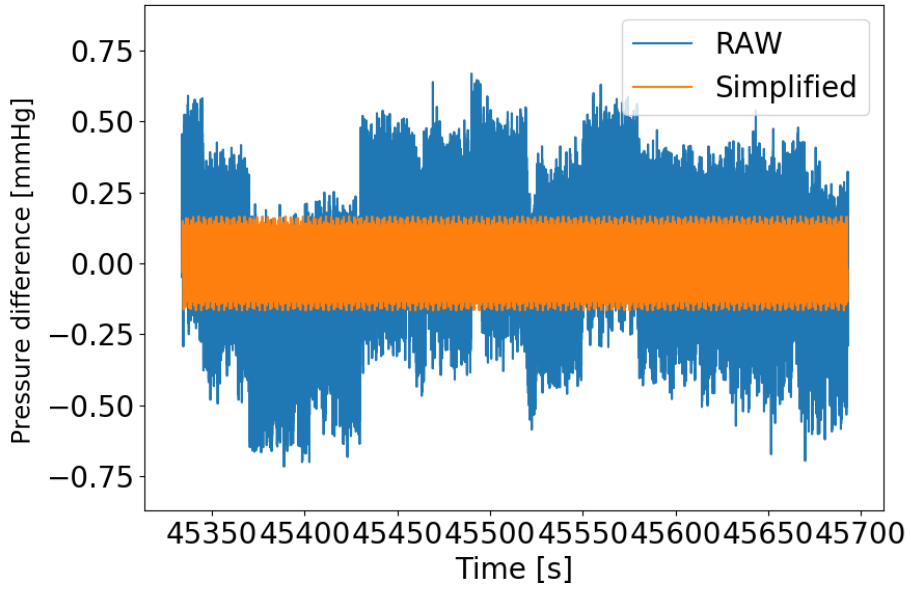


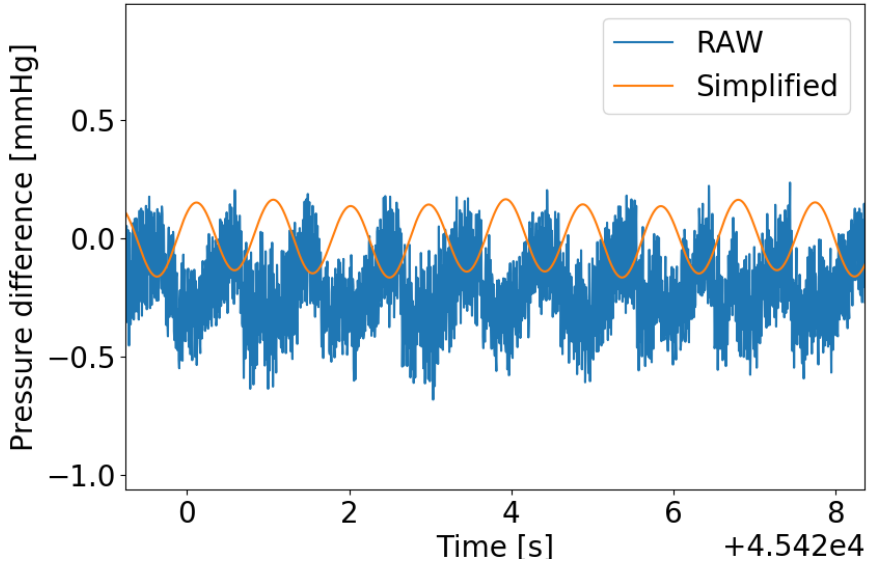


Patient 4

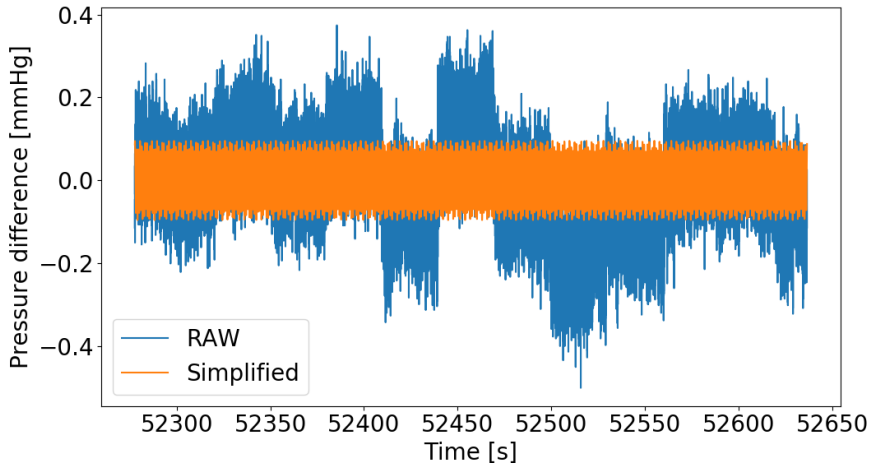


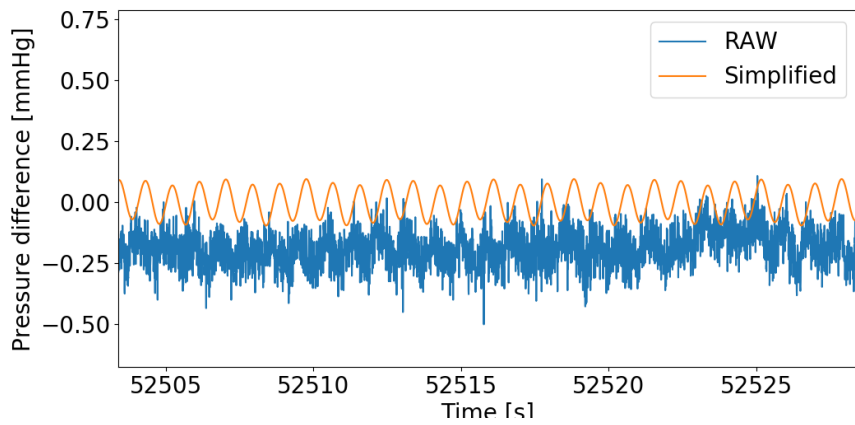
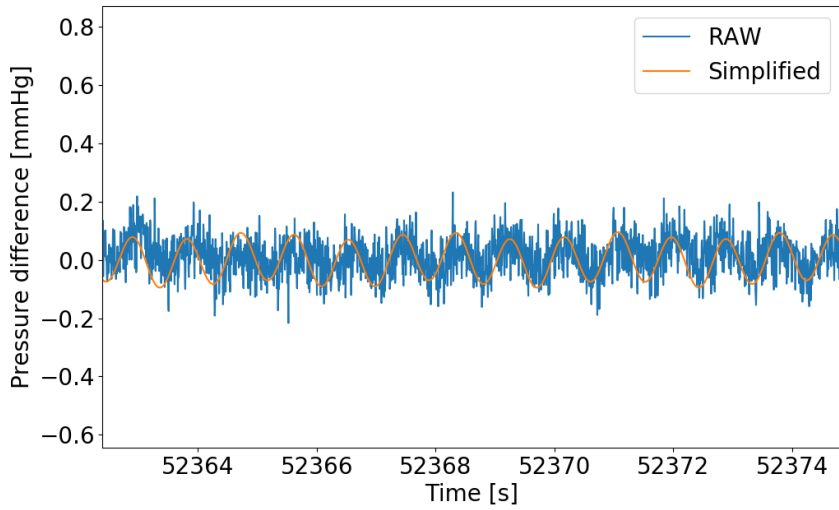
Patient 5



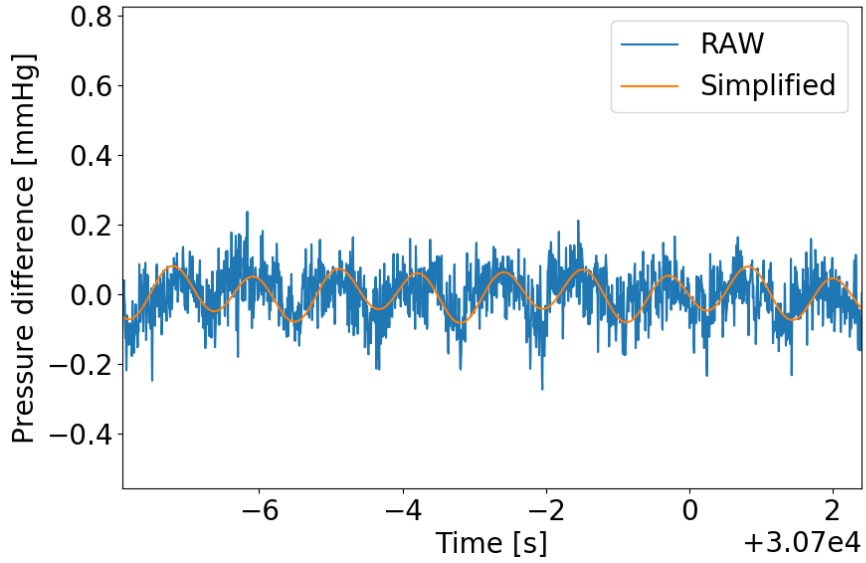
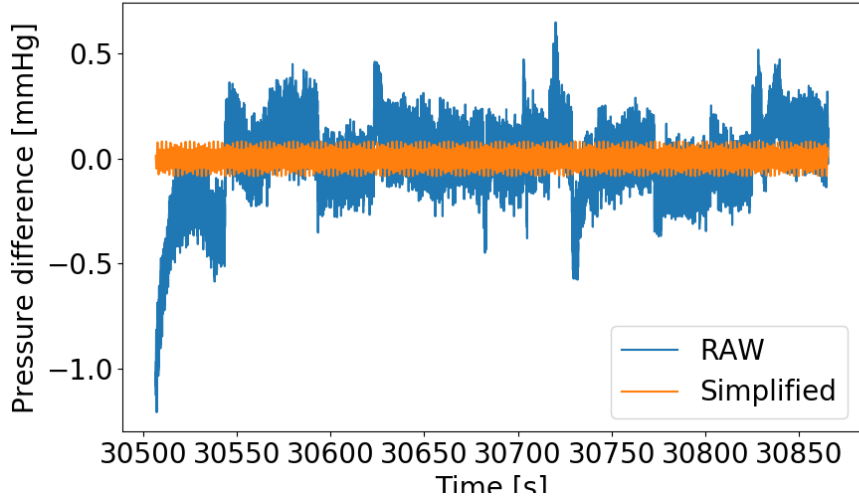


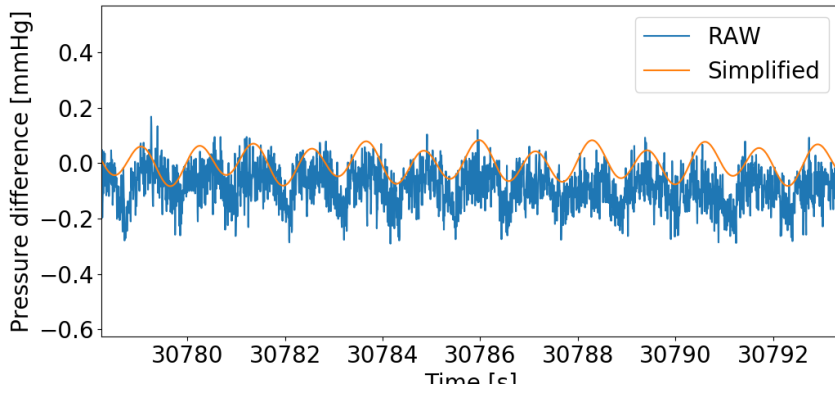
Patient 6



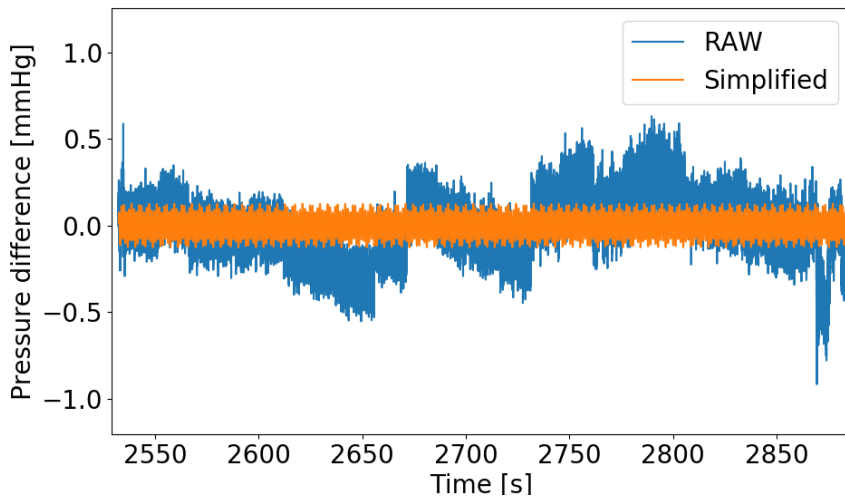


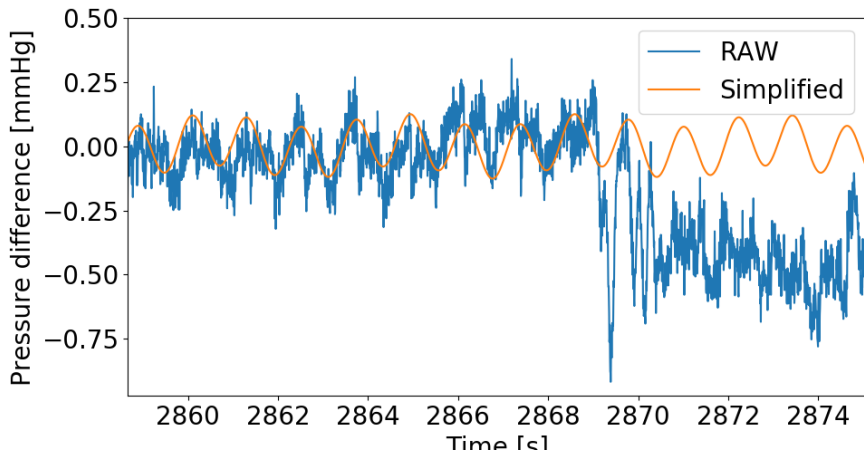
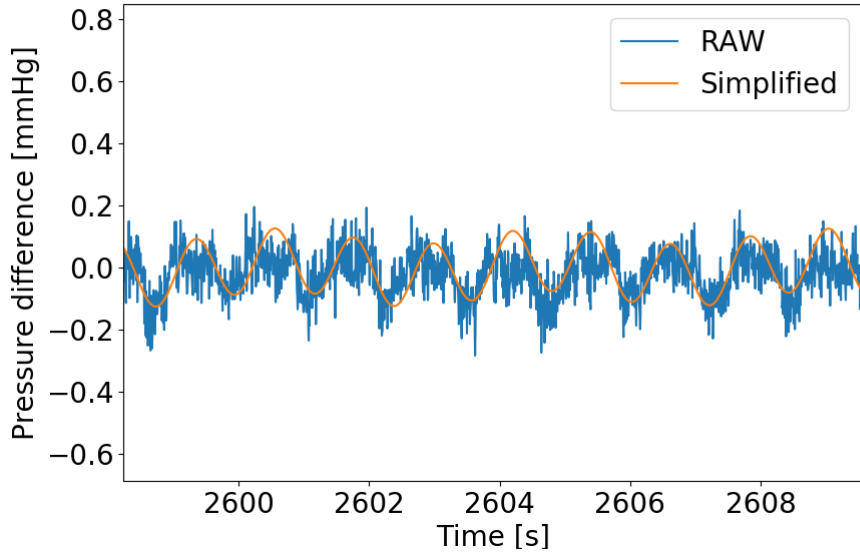
Patient 7



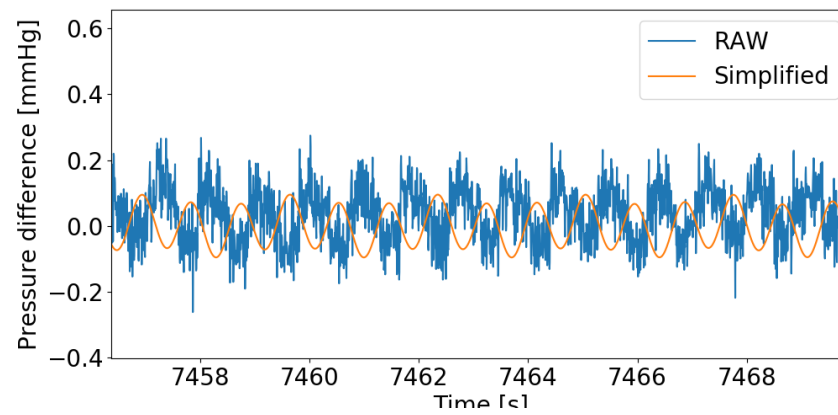
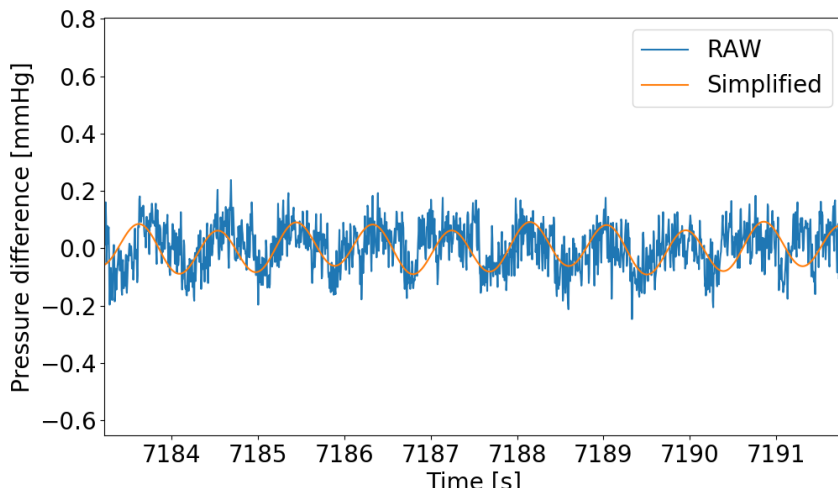
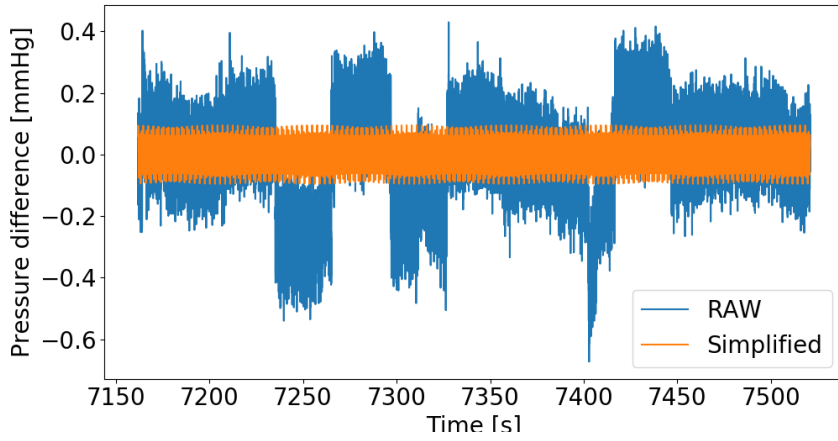


Patient 8



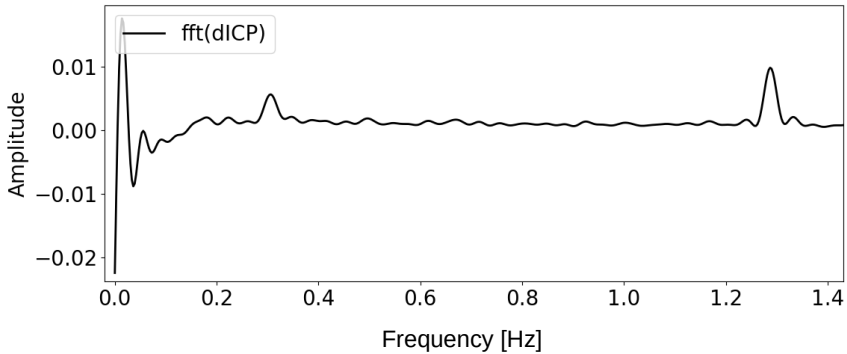


Patient 9



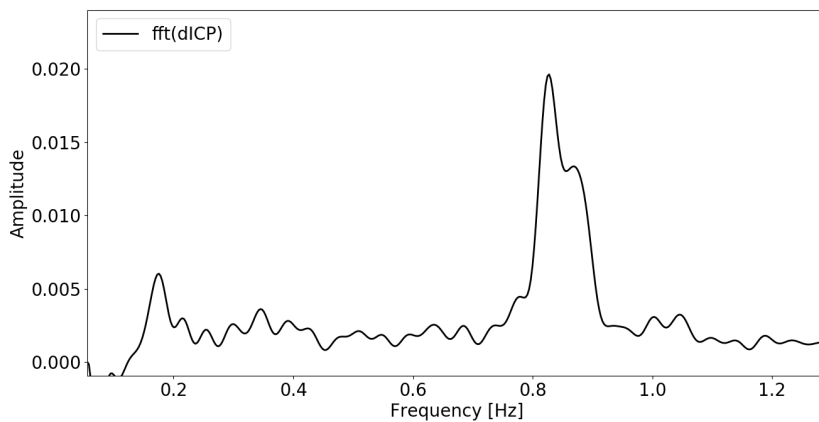
Examples of Extracted 6-minute windows (Fourier series)

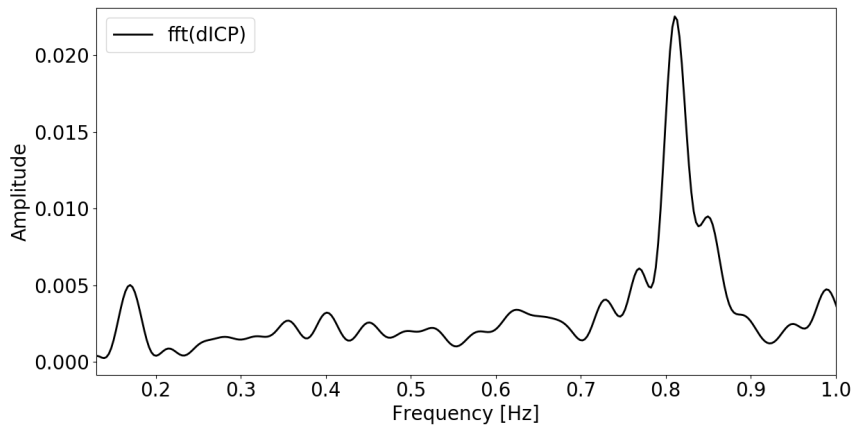
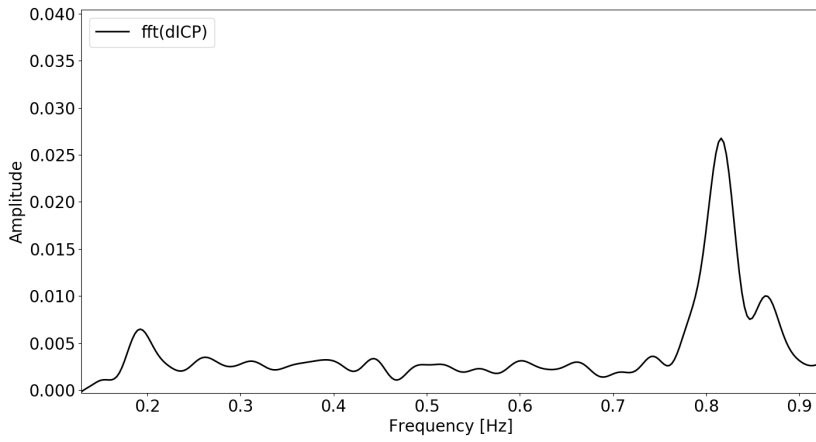
In this section we provide three examples of extracted 6-minute windows, again for patient 2 through 9 (as patient 1 is already shown in the paper). In most of the shown windows there is a clear cardiac and a clear respiratory component. In some patients (e.g. typically for patient 3), the effect of respiration is not that evident in some of the windows. This is reflected in a low pressure gradient ratio between cardiac and respiratory amplitude (cf. Table 1). We do not show the low frequencies to the jumps causing high energy at these frequencies. The first figure shown is an example a 6-minute window without zooming into the respiratory and cardiac frequency range.



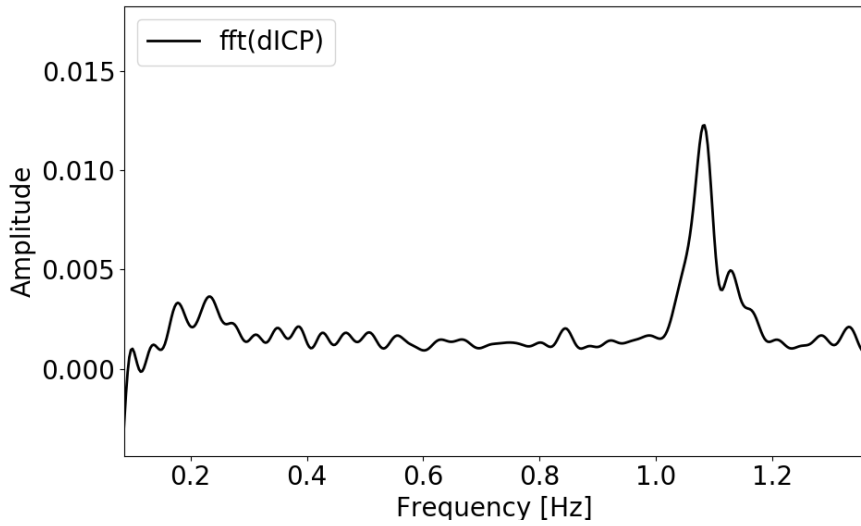
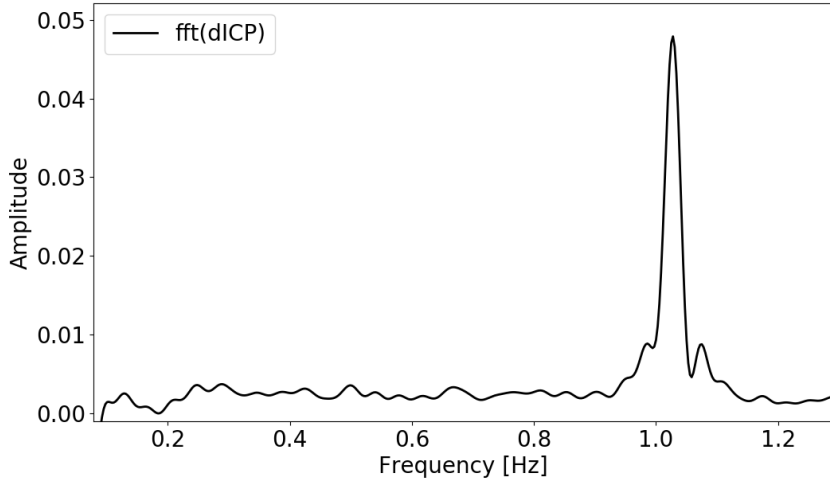
An example of a 6-minute window before focusing into the cardiac and respiratory components.

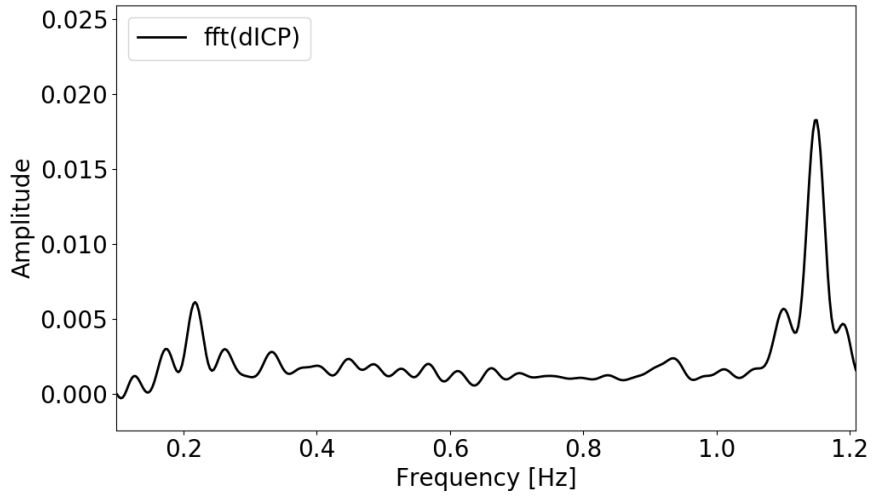
Patient 2



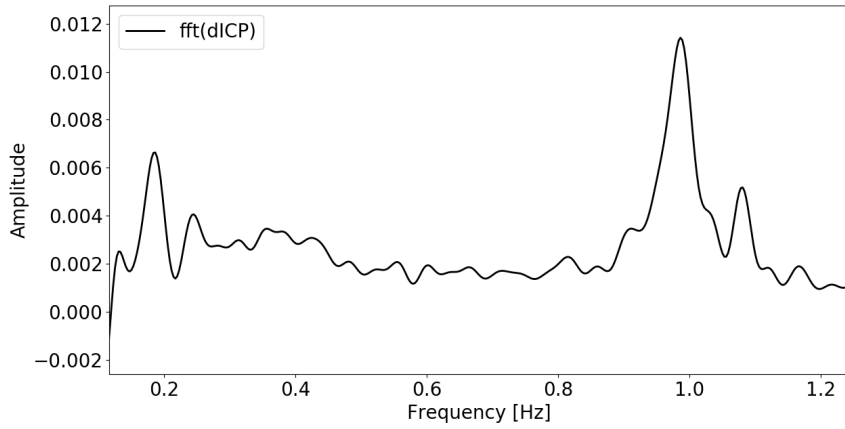


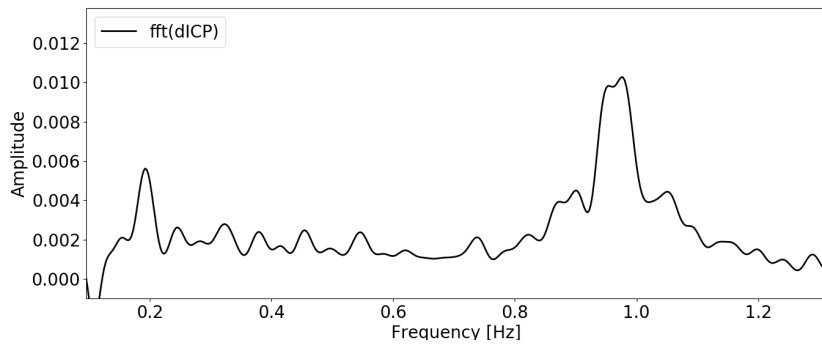
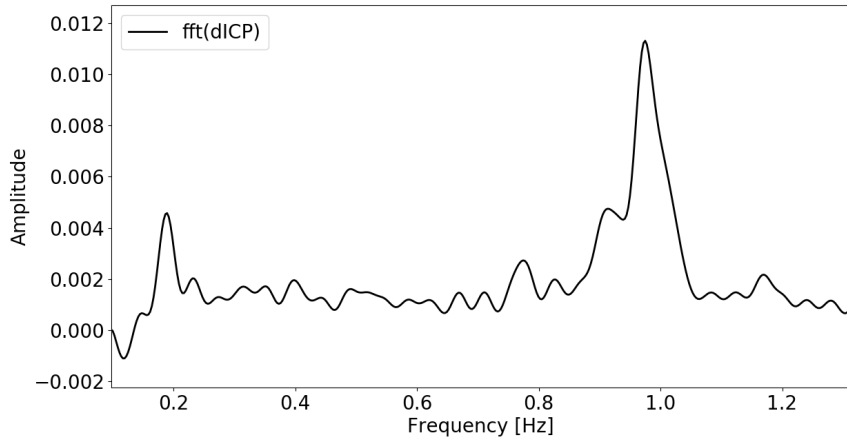
Patient 3



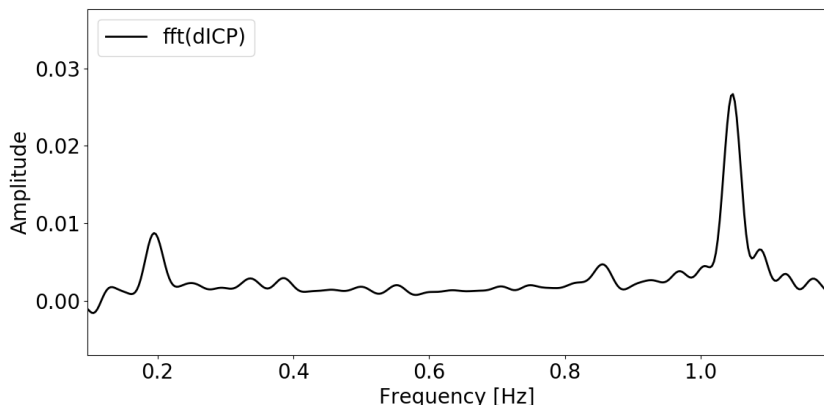
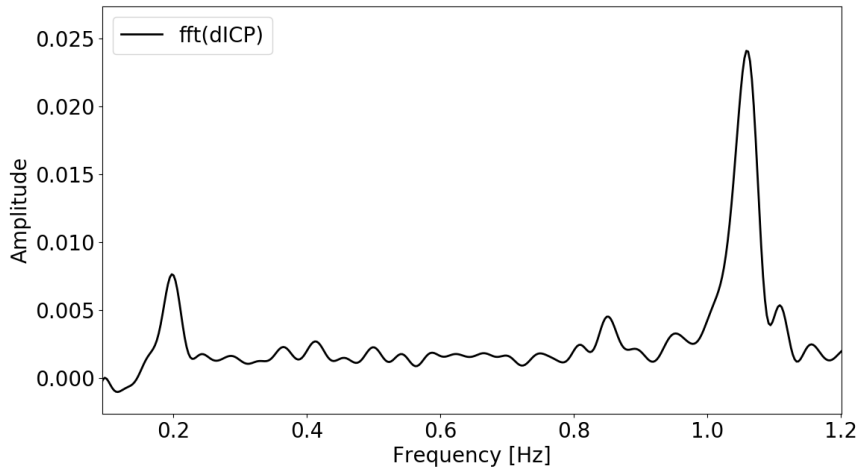


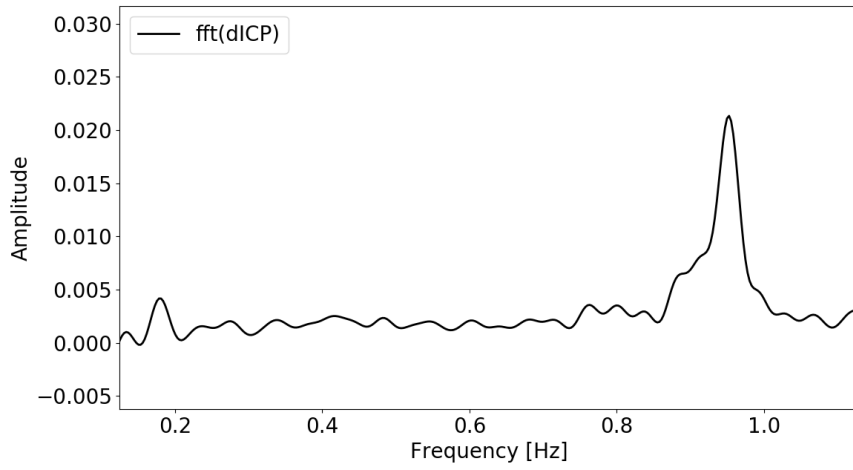
Patient 4



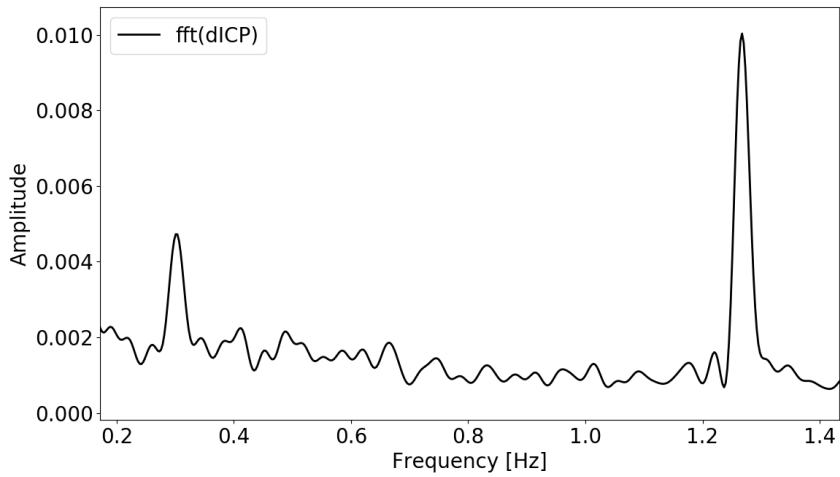


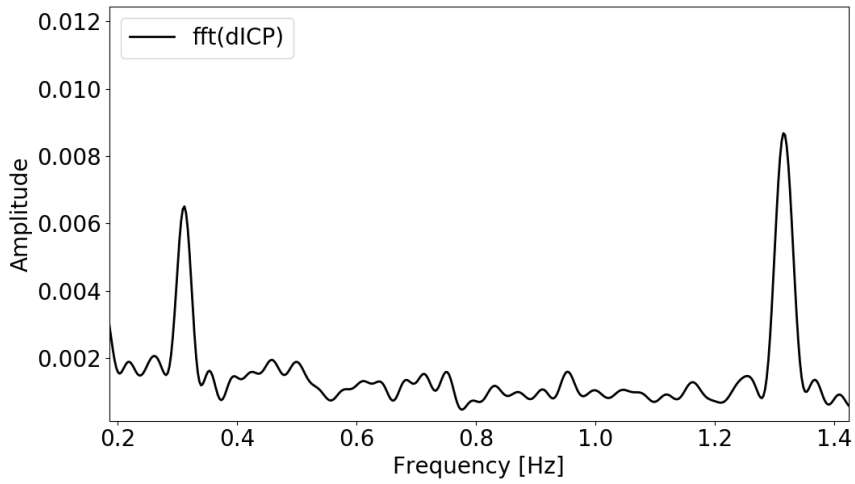
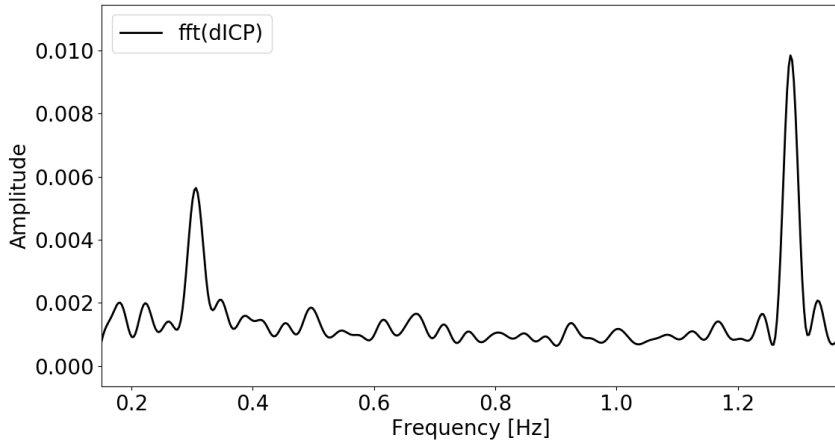
Patient 5



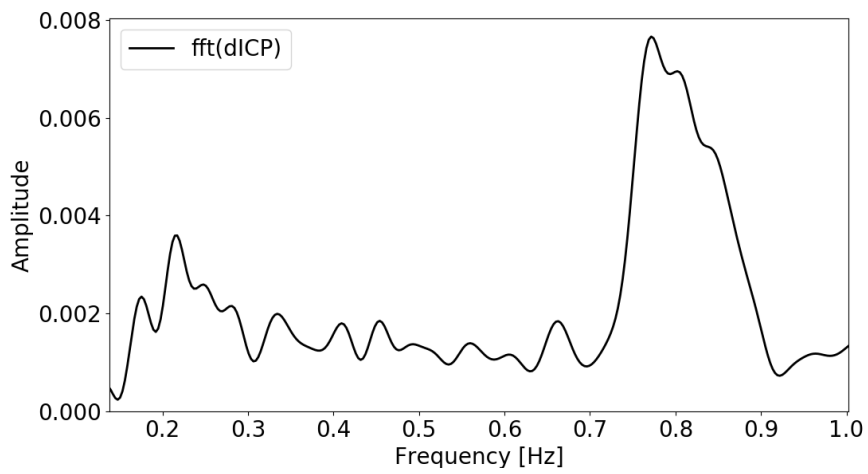
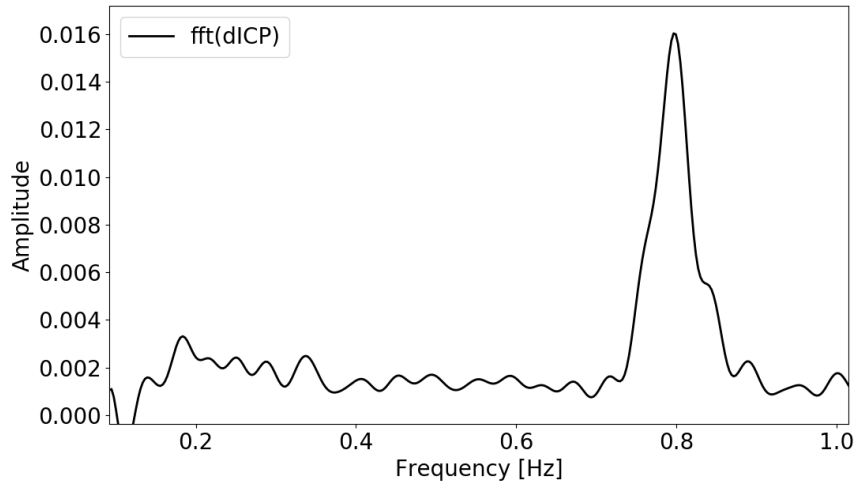


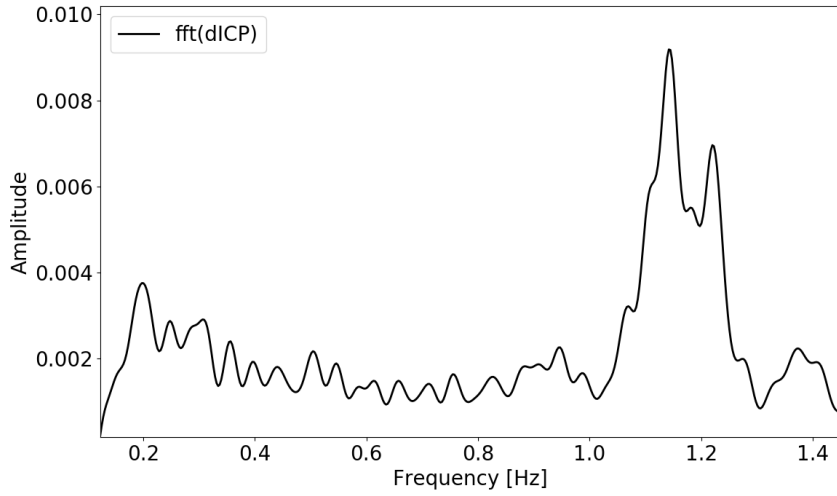
Patient 6



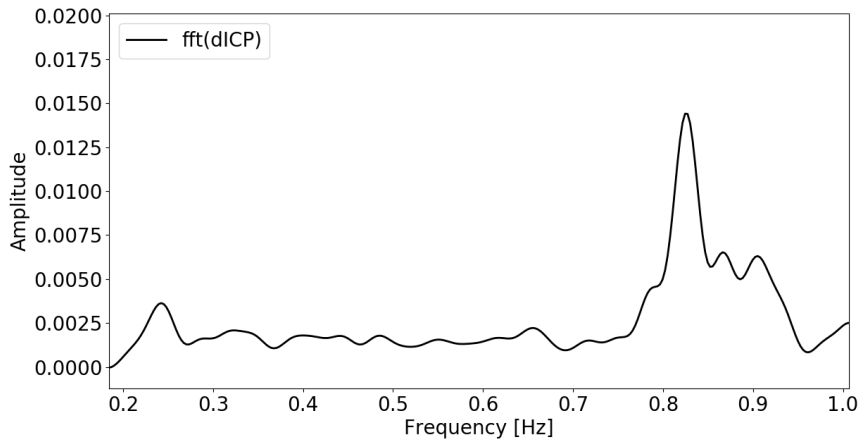


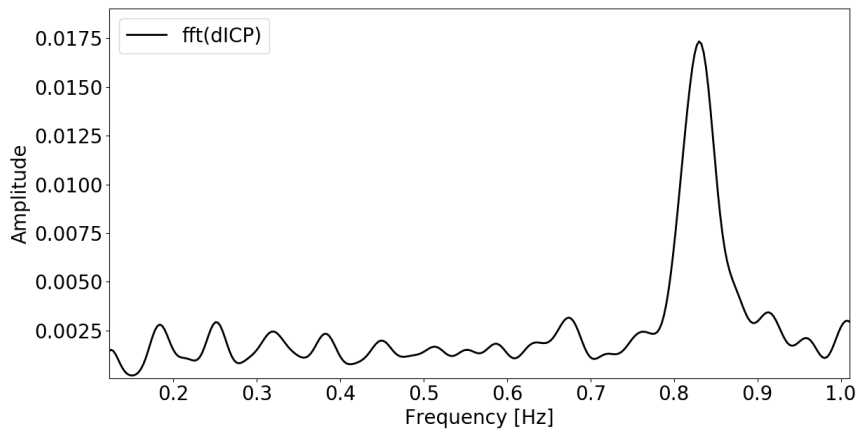
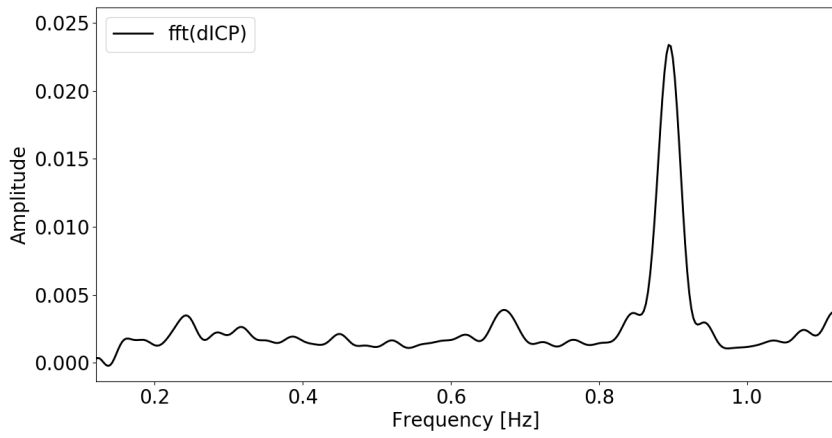
Patient 7



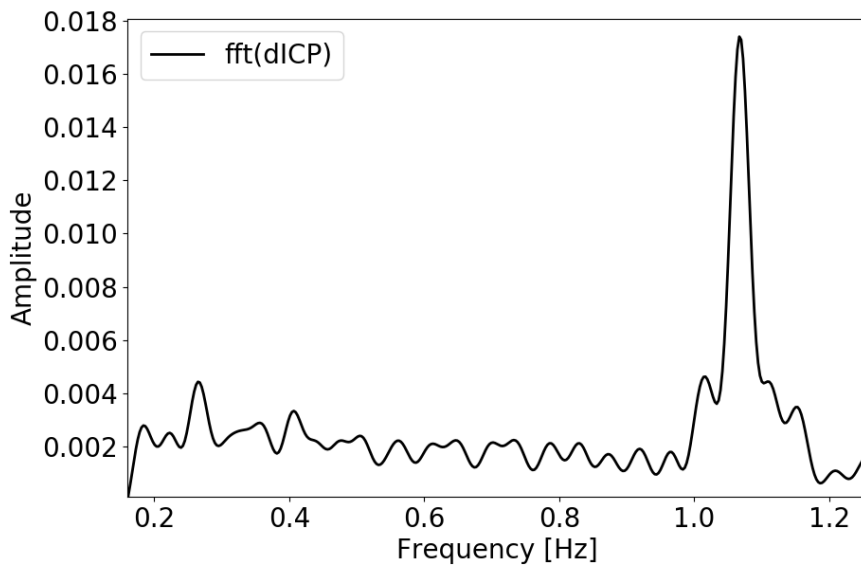
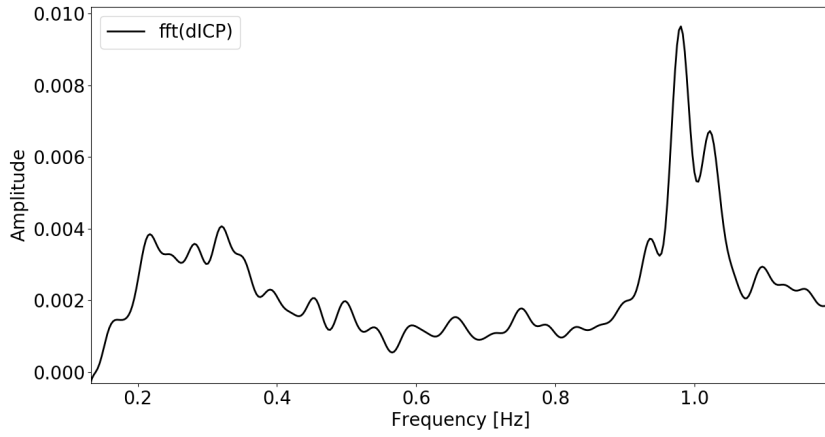


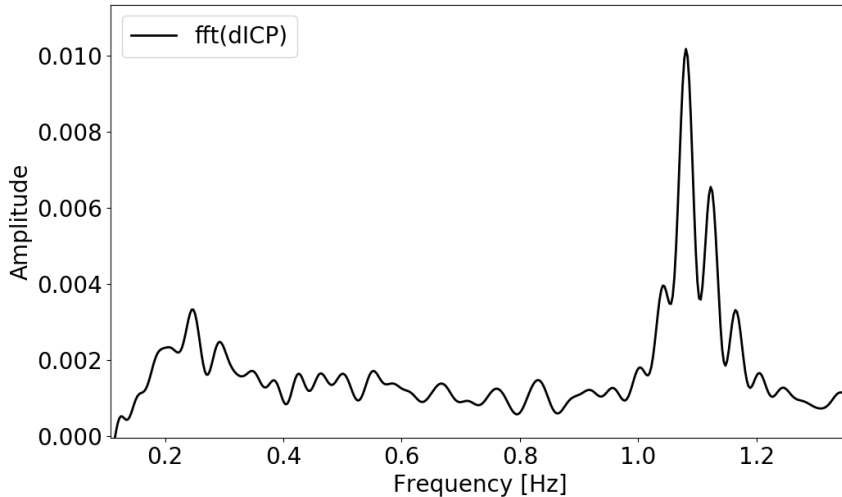
Patient 8





Patient 9





Methods:

Experimental design

To obtain T1-weighted images, MRI was performed in a 3 Tesla (T) Philips Ingenia scanner (Philips Medical Systems®, Best, The Netherlands). The main acquisition parameters for the T1-weighted gradient echo volume scan were: TR/TE = shortest (typically 5.1/2.3 ms), FA = 8 degrees, and sampled 184 over-contiguous (overlapping) slices with 1 mm thickness, automatically reconstructed to 368 slices with 0.5 mm thickness.

To obtain PC-MRI of CSF flow in the cerebral aqueduct of the three patients, a region of interest (ROI) was manually defined using the software MATLAB and thereafter approved by a neuroradiologist (G.R.). In the surrounding tissue, a reference ROI was defined to compensate for potential biasing in the data set. Recorded velocities were transformed from pixels to centimeters per second by applying linear transformation on the velocity encoding and the range of pixels values. All pixel velocities in the ROI were summed for each time step and multiplied by the pixel size to achieve the volumetric flow rate. The main acquisition parameters for PC-MRI were: Repetition time (TR) = 25 ms, echo time (TE) = 15 ms, slice thickness = 4 mm, pixel size = 0.48 x 0.48 mm², flip angle (FA) = 15 degrees, and velocity encoding gradient (VENC) = 10 cm/s with retrospective peripheral cardiac gating.

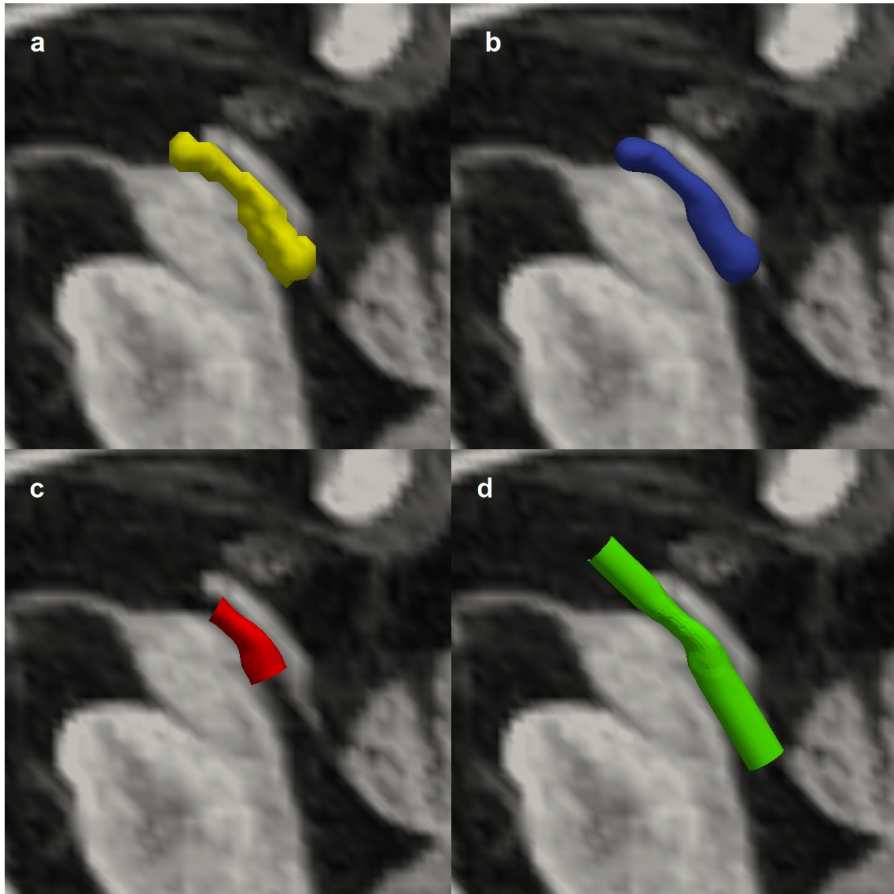
Sensor Validation

Our methodology relies on the exact reproduction of the ICP waveform. Even though amplitudes often are on the order of 5 mmHg, a 50 Hz frequency is adequate to capture the ICP waveform

within errors of ~ 0.2 mmHg, while 100 Hz frequency is adequate to capture the ICP waveform within errors of ~ 0.1 mmHg [43]. In our study, we used a sampling rate of 200 Hz. The Codman sensor used has been extensively tested and have adequate sensitivity to measure differences on the order of 0.1 mmHg. Differences on this order has also been published in previous analyses of the same data set [22].

Construction of patient-specific 3D-geometries

The process started by manual interaction with the colliding fronts option in VMTK to segment the CSF in the cerebral aqueduct. Then, the marching cubes algorithm was used to generate the surface of the segmented volume (Supplementary Fig. S2a), and the surface was subsequently smoothed (Supplementary Fig. S2b). The inlet and outlet of the cerebral aqueduct surface was constructed by plane clipping (Supplementary Fig. S2c) and cylindric extensions were added to the inlet and outlet to avoid boundary effects (Supplementary Fig. S2d). Finally, the geometric model was created with the mesh generator in VMTK.



Supplementary Figure S2: The steps in constructing the patient-specific computational geometries. (a) The surface obtained using the marching cube algorithm on the cerebrospinal fluid segmentation of the cerebral aqueduct. (b) The surface after being smoothed. (c) The surface after plane cutting. (d) The surface after cylindrical extension were added.

PatID	G	Diag.	Age (yrs)	Duration of symptoms	Location ICP sensor	^a Clinical severity (NPH score)	^b Treatment	Clinical response
1	F	iNPH	66	3 months	Intraventricular + subdural	9	Conservative	
2	F	iNPH	70	4 years	Intraventricular + subdural	11	VP shunt	R
3	F	iNPH	71	2 years	Intraventricular + subdural	13	VP shunt	R
4	F	iNPH	54	7 months	Intraventricular + parenchymal	14	Conservative	
5	F	iNPH	74	2 years	Intraventricular + parenchymal	11	VP shunt	R
6	M	iNPH	65	12 months	Intraventricular + subdural	10	Conservative	
7	M	iNPH	76	4 years	Intraventricular + subdural	8	VP shunt	R
8	M	iNPH	80	1 year	Intraventricular + subdural	9	VP shunt	NR
9	F	iNPH	76	2 years	Intraventricular + subdural	9	VP shunt	R

Supplementary Table S1: Demographic and clinical data of the patient cohort. G: gender. Diag: diagnosis. F: female. M: male. ^aClinical severity (NPH score) ^bTreatment: VP shunts were of type Codman-Hakim programmable 12 cm H₂O opening pressure. R: Responder. NR: Non-responder

Paper 3

Uncertainty quantification of parenchymal tracer distribution using random diffusion and convective velocity fields

Uncertainty quantification of parenchymal tracer distribution using random diffusion and convective velocity fields

Vegard Vinje¹, Matteo Croci^{1,2}, and Marie E. Rognes¹

¹Department of Scientific Computing and Numerical Analysis, Simula Research Laboratory, Lysaker, Norway.

²Mathematical Institute, University of Oxford, Oxford, United Kingdom.
*meg@simula.no

May 2019

Abstract

Background: Influx and clearance of substances in the brain parenchyma occur by a combination of diffusion and convection, but the relative importance of these mechanisms is unclear. Accurate modeling of tracer distributions in the brain relies on parameters that are partially unknown and with literature values varying up to 7 orders of magnitude. In this work, we rigorously quantified the variability of tracer enhancement in the brain resulting from uncertainty in diffusion and convection model parameters.

Methods: In a mesh of a human brain, using the convection-diffusion-reaction equation, we simulated tracer enhancement in the brain parenchyma after intrathecal injection. Several models were tested to assess the uncertainty both in type of diffusion and velocity fields and also the importance of their magnitude. Our results were compared with experimental results of tracer enhancement from MRI .

Results: In models of pure diffusion, the expected amount of tracer in the gray matter reached peak value after 15 hours, while the white matter does not reach peak within 24 hours with high likelihood. Models of the glymphatic system behave qualitatively similar as the models of pure diffusion with respect to expected time to peak but display less variability. However, the expected time to peak was reduced to 11 hours when an additional directionality was prescribed for the glymphatic circulation. In a model including drainage directly from the brain parenchyma, time to peak occurred after 6-8 hours for the gray matter.

Conclusion: Even when uncertainties are taken into account, we find that diffusion alone is not sufficient to explain transport of tracer deep into the white matter as seen in experimental data. Adding a glymphatic velocity field may increase transport, but only if a directional structure is added to the glymphatic circulation.

1 Introduction

Over the last decade, there has been a significant renewed interest in the waterscape of the brain; that is, the physiological mechanisms governing cerebrospinal fluid (CSF) and interstitial fluid (ISF) flow in (and around) the brain parenchyma. A number of new theories have emerged including the glymphatic system [37, 39], the intramural periarterial drainage (IPAD) theory [18, 5], and the Bulat-Klarica-Oreskovic hypothesis [53], along with critical evaluations [34, 11, 68]. A great deal of uncertainty and a number of open questions relating to the roles of diffusion, convection and clearance within the brain parenchyma remain.

Exchange between CSF and ISF is hypothesized to occur along small fluid-filled spaces surrounding large penetrating arteries in the brain parenchyma known as paravascular spaces (PVS) [61, 37]. Tracer has been observed to move faster in paravascular spaces in response to increased arterial pulsations, and arterial pulsation has thus been proposed as the main driver of paraarterial flow [30, 38, 48]. After entering the extracellular space (ECS), a bulk flow of ISF from paraarterial to the paravenous spaces has been proposed to occur before re-entry to the subarachnoid space (SAS) [39]. This concept of CSF/ISF fluid circulation has been named the glymphatic system, with bulk flow as a mechanism for effective waste clearance from the brain parenchyma. Xie et al. [75] showed glymphatic influx to increase in sleeping mice, linking the importance of sleep to clearance of waste products. Sleep was also associated with an increased interstitial space volume fraction, a possible explanation for increased flow through the interstitial space. MRI investigations have also found evidence for glymphatic function in human brains [64, 63].

While several studies demonstrate CSF influx along paraarterial spaces [60, 37, 16, 48], the efflux route is more debated. Carare et al. [18] found evidence of solutes draining from the brain parenchyma along basement membranes of capillaries and arteries, going in the opposite direction of blood flow and possible PVS fluid movement. This flow is however not facilitated by arterial pulsations [23], but by the movement of smooth muscle cells [6]. Bedussi et al. [15] observed tracers move towards the ventricular system, ultimately leaving the brain via the cribriform plate and the nose. A continuous pathway alongside capillaries to the paravenous space has been suggested [31], and capillaries continuously filtrate and absorb water inside the brain parenchyma [53]. In addition, substances may leave the parenchyma crossing the blood-brain barrier, or possibly directly to lymph nodes [35].

In a recent review, Abbott and colleagues [2] concluded that bulk flow within the parenchyma is likely to be restricted to the PVS and possibly white matter tracts, and not present in the neuropil of gray matter. Earlier studies have reported a bulk flow velocity of less than $1 \mu\text{m/s}$ [51], while recent evidence suggests average net bulk flow of around $20 \mu\text{m/sec}$, restricted to the PVS [14, 48]. Nevertheless, since tracer movement in in-vivo studies does not necessarily directly reflect underlying fluid flow [8], the exact velocity field governing ISF flow in the brain remains unknown.

All of the aforementioned in-vivo studies have used tracers or micro-spheres to track the movement of fluid within the intracranial space. Injection of fluid at rates as low as $1 \mu\text{L/min}$ can cause a significant increase of local intracranial pressure (ICP) [73], which may lead to pressure gradients driving bulk flow. On the other hand, non-invasive methods such as diffusion tensor imaging may serve as a promising tool due to its sensitivity to dispersion and bulk flow. This method has been applied successfully to demonstrate increased diffusivity with vascular pulsation compared to diastole [32]. The diffusion coefficient was found to be anisotropic and highest parallel to PVS, however a value of the bulk fluid velocity could not be reported from these measurements. In addition to both invasive and non-invasive experiments, computational models have been used to assess the possibility and plausibility of bulk flow within the parenchyma. Tracer movement in the extracellular space has been found to be dominated by diffusion [36], a conclusion similar to that of Smith et al. [68] in experimental studies with very low infusion rates.

Even though computational models can distinguish between diffusion and bulk flow, a major chal-

lenge remains with regard to the unknown material parameters, boundary conditions and other model configurations needed to accurately predict the movement of ISF in the brain parenchyma. For instance, the permeability of brain tissue used in computational models varies from 10^{-10} to 10^{-17} m^2 [28, 36]. Because the permeability is directly linked to the Darcy fluid velocity in these models, this parameter choice could result in a difference of 7 orders of magnitude in predicted ISF flow. In addition, CSF dynamics vary between subjects [13] and human CSF production has been reported to increase in the sleeping state [52] which may alter ISF flow. Recently it has been pointed out that there is an overarching need to reduce uncertainty when characterizing the anatomy and fluid dynamics parameters in models considering the glymphatic circulation[66].

Replacing partial differential equation (PDE) parameters subject to uncertainty with spatially correlated random fields is a common modelling choice in the uncertainty quantification (UQ) literature [21, 19, 70] and Monte Carlo methods have been successfully used in biology to quantify how uncertainty in model input propagates to uncertainty in model output. However, these methods have mainly been applied to simulations of the cardiovascular system [57, 17] and, to our knowledge, there has only been one study in which Monte Carlo methods have been used for UQ in brain modelling [33]. To the authors' knowledge, there has been no previous work on stochastic forward uncertainty quantification for simulations of tracer transport with the brain parenchyma.

With this study, we aim to rigorously quantify how the aforementioned uncertainties in the physiological parameters and in ISF flow affect the spread of a tracer from the SAS into the brain parenchyma. We assume movement of tracer in the brain parenchyma to occur by diffusion and/or convection. To account for uncertainty and variability, we circumvent the lack of precise parameter values by modelling velocity and diffusivity as Matérn stochastic fields. We then set up a PDE model with these stochastic (random) fields as coefficients and quantify the uncertainty in the model prediction via the Monte Carlo (MC) method.

More specifically, we model the contrast MRI study performed by Ringstad et al. [64] assessing glymphatic function in the human brain and derive a baseline convection-diffusion-reaction PDE. The model coefficients are designed to represent different hypotheses on CSF flow and clearance, including diffusion, the glymphatic system and possible capillary absorption, and uncertainty within each hypothesis. A total of five different models were investigated, each with stochastic model coefficients. For each model, we compute the expected values and 99.73% confidence intervals for different functionals of interest of the tracer concentration. The results reported in the study by Ringstad et al. are compared with the range of uncertainty in our model. We find that although the uncertainty associated with diffusion yields great variability in tracer distribution, diffusion alone is not sufficient to explain transport of tracer deep into the white matter as seen in experimental data. A glymphatic velocity field may increase tracer enhancement, but only when adding a directional structure to the glymphatic circulation.

2 Methods

We model the MRI-study of Ringstad et al. [64]. In their experiments, 0.5 mL of 1.0 mmol/mL of the radioactive tracer gadobutrol was injected intrathecally in 15 hydrocephalus patients and eight reference subjects. The localization of the tracer was found with MRI at 4 different time periods, at 1, 3, 4.5, and 24 hours following the injection. After 3 hours, tracer was localized in the lower region of the cranial SAS, and had started to penetrate into the brain parenchyma of the reference subjects. The following day it had spread throughout the brain tissue. Tracer was found to penetrate along large leptomeningeal arteries in all study subjects, and a low proportion of tracer was found at the upper convexities of the brain.

2.1 Gaussian and Matérn fields

Let $(\Omega, \mathcal{A}, \mathbb{P})$ be a probability space, let $\mathcal{D} \subset \mathbb{R}^3$ be an open domain (representing the brain parenchyma) with coordinates $x \in \mathcal{D}$, and let $t \geq 0$ denote time. A random field $X = X(x, \omega)$, $\omega \in \Omega$, $x \in \mathbb{R}^d$ is a function whose values are random variables for each $x \in \mathbb{R}^d$. The field is Gaussian if these random variables are all joint Gaussian [3]. A Gaussian field is uniquely determined by providing a mean $\mu(x)$ and a symmetric positive definite covariance function $\mathcal{C}(x, y)$.

A Matérn field is a Gaussian field with covariance of the Matérn class, i.e. of the form

$$\mathcal{C}(x, y) = \mathbb{E}[(X(x, \omega) - \mu(x))(X(y, \omega) - \mu(y))] = \frac{\sigma^2}{2^{\nu-1}\Gamma(\nu)} (\kappa r)^\nu \mathcal{K}_\nu(\kappa r), \quad r = \|x - y\|_2, \quad \kappa = \frac{\sqrt{8\nu}}{\lambda}, \quad x, y \in \mathcal{D}, \quad (1)$$

where $\Gamma(x)$ is the Euler Gamma function and σ^2 , ν , $\lambda > 0$ are the variance, smoothness parameter and correlation length of the field respectively and \mathcal{K}_ν is the modified Bessel function of the second kind. Matérn fields are extensively used in spatial statistics, biology and oil reservoir modelling to represent uncertain or randomly-varying fields [55, 44]. The smoothness parameter ν regulates the field's spatial smoothness: field samples are almost surely continuous and $\lceil \nu \rceil - 1$ times differentiable [3]. For the two cases $\nu = 1/2$ and $\nu = \infty$, (1) reduces to the exponential and Gaussian covariance kernels, respectively.

The correlation length λ roughly represents the distance past which point values of the field are approximately uncorrelated. Informally, this means that in each realization of the Matérn field, there are regions of length proportional to λ within which the values of the field are similar.

2.2 Stochastic models for tracer movement in the brain parenchyma

We consider the following partial differential equation with random coefficients to model transport of tracer in the brain parenchyma under uncertainty: find the tracer concentration $c = c(t, x, \omega)$ for $x \in \mathcal{D}$, $\omega \in \Omega$ and $t \geq 0$ such that

$$\dot{c}(t, x, \omega) + \nabla \cdot (v(x, \omega)c(t, x, \omega)) - \nabla \cdot (D^*(x, \omega)\nabla c(t, x, \omega)) + rc(t, x, \omega) = 0. \quad (2)$$

Here, the superimposed dot represents the time derivative, D^* is the effective diffusion coefficient of the tracer in the tissue (depending on the tracer free diffusion coefficient and the tissue tortuosity) [51], v represents a convective fluid velocity and $r \leq 0$ is a drainage coefficient potentially representing e.g. capillary absorption[53] or direct outflow to lymph nodes[64]. We assume that the parenchymal domain contains no tracer initially: $c(0, x, \omega) = 0$.

To investigate and compare different hypotheses for parenchymal ISF flow and tracer transport, we consider 5 stochastic model variations of (2) including two models with stochastic (random) diffusion properties (Model D1 and D2) and three models with stochastic velocity fields (Models V1, V2, and V3). The diffusion-only Models D1 and D2 correspond to negligible ISF bulk flow in the parenchyma and the absence of capillary absorption or other direct outflow pathways. For the velocity models (V1, V2 and V3), we consider a fixed non-random diffusion coefficient in order to isolate the effects of the stochastic velocity fields. A summary of the models are presented in Table 1, while the mathematical modelling aspects are described in further detail in the following sections.

Domain and geometry We define the computational domain \mathcal{D} as the union of white and gray matter from the generic Colin27 human adult brain atlas FEM mesh[26] version 2 (Figure 1). This domain includes the cerebellum. The levels of the foramen magnum, the sylvian fissure and the precentral sulcus are well represented by z-coordinates -0.1, 0 and 0.1 m, respectively. The plane $z = 0$ corresponds approximately to the level of the lateral ventricles.

Label	D^*	ν	r	Short descriptor
Model D1	Random variable	0	0	Homogeneous diffusion
Model D2	Random field	0	0	Heterogeneous diffusion
Model V1	Constant	Random influx and outflux field	0	Glymphatic circulation
Model V2	Constant	Model V1 + directional velocity field	0	Glymphatic directionality
Model V3	Constant	Random influx field	$r < 0$	Influx with drainage

Table 1: Overview of models considered in the study

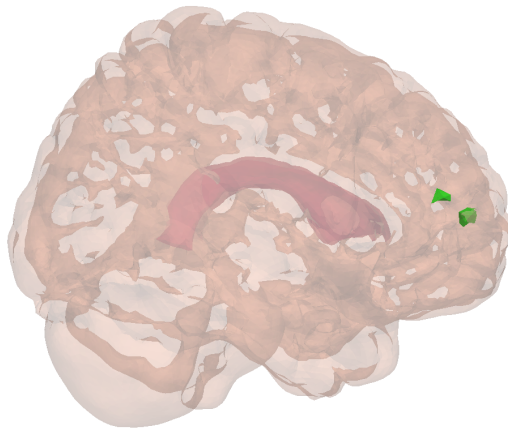


Figure 1: The computational domain representing the brain parenchyma including the cerebellum. The interior lateral ventricles are marked (dark pink) in the central region of the domain. Two smaller regions of interest S_g and S_w , in the gray and white matter respectively, are marked in green (leftmost region: S_w , rightmost region: S_g).

Boundary conditions modelling tracer movement in the SAS Let ∂D be the boundary of \mathcal{D} and let $\partial \mathcal{D} = \partial \mathcal{D}_S \cup \partial \mathcal{D}_V$, with $\partial \mathcal{D}_S$ representing the interface between the brain parenchyma and the subarachnoid space (SAS), and $\partial \mathcal{D}_V$ representing the interface between the brain parenchyma and cerebral ventricles, respectively. We consider the following boundary conditions for (2):

$$c = g(c) \text{ on } \partial \mathcal{D}_S, \quad (3)$$

$$D^* \nabla c \cdot n = 0 \text{ on } \partial \mathcal{D}_V. \quad (4)$$

In particular, we assume that a tracer concentration is given at the SAS interface (3) and no ventricular outflux (4). The dependence of g on c in (3) is detailed below.

The boundary condition (3) models the movement of tracer starting from the lower cranial SAS and traveling upward in the CSF surrounding the brain as observed in the study by Ringstad et al [64]. In particular, we let

$$g(c)(t, x, \omega) = c_{\text{CSF}}(t, \omega) h(t, x), \quad h(t, x) = \left(0.5 + \frac{1}{\pi} \arctan(-a(x_3 - z_0 - u_z t)) \right), \quad x = (x_1, x_2, x_3). \quad (5)$$

Here, at time t , $c_{\text{CSF}}(t)$ is the average tracer concentration in the SAS, while $h(t, x)$ represents its spatial distribution.

The expression for h is based on the following considerations. We assume that the diffusive and/or convective movement of tracer from the spinal to the cranial SAS over time is known, and we thus model $h(t, x)$ as a smooth step function upwards (in the x_3 - or z -direction). In (5), u_z represents the speed of tracer movement upwards in the SAS, and a reflects the gradient of tracer concentration from the lower to the upper cranial SAS. Finally, we assume that at time $t = 0$, the tracer has spread up to a relative distance of z_0 from the lateral ventricles. This specific expression for $h(t, x)$ and the values of parameters a , z_0 and u_z are based on the spread of tracer seen in the MR-images in the study by Ringstad et al. [64]. In particular, we use $a = 20 \text{ m}^{-1}$, $u_z = 1.5 \times 10^{-5} \text{ m/sec}$ and $z_0 = -0.2 \text{ m}$. These parameters were chosen to match time to peak in three different regions in the CSF space in reference individuals[64].

To derive an expression for c_{CSF} in (5), we consider the conservation of tracer mass. We model the spread of $n_0 = 0.5 \text{ mmol}$ tracer in the CSF, assuming a volume of $V_{\text{CSF}} = 140 \text{ mL}$ CSF in the human SAS and ventricles[74]. The average concentration in the SAS right after injection is thus $c_{\text{CSF}}(0) = 0.5 \text{ mmol}/140 \text{ mL} = 3.57 \text{ mol/m}^3$. At any given time, we assume that the total amount of tracer in the brain and in the SAS plus or minus the tracer absorbed or produced stays constant in time, and is equal to the initial amount $n_0 = 0.5 \text{ mmol}$ (almost surely):

$$\int_{\mathcal{D}} c(t, x, \omega) dx + c_{\text{CSF}}(t, \omega) V_{\text{CSF}} + \int_0^t \int_{\mathcal{D}} r c(\tau, x, \omega) dx d\tau = n_0. \quad (6)$$

Solving for c_{CSF} , we thus obtain

$$c_{\text{CSF}}(t, \omega) = \frac{1}{V_{\text{CSF}}} \left(n_0 - \int_{\mathcal{D}} c(t, x, \omega) dx - \int_0^t \int_{\mathcal{D}} r c(\tau, x, \omega) dx d\tau \right). \quad (7)$$

Quantities of interest To evaluate the speed and characteristics of tracer movement into and in the brain parenchyma, we consider a set of functionals describing different output quantities of interest. To quantify the overall spread of tracer in the gray and white matter, we consider the (integrated) amount of tracer in the gray matter Q_g and in the white matter Q_w at time points τ :

$$Q_g(\omega) = \int_{D_g} c(\tau, x, \omega) dx, \quad Q_w(\omega) = \int_{D_w} c(\tau, x, \omega) dx. \quad (8)$$

We pay particular attention to the times $\tau \in \{3, 5, 8, 24\}$. To further differentiate, we also defined two localized functionals at each time τ : the average tracer concentration q_g in a small subregion of the gray matter S_g and analogously q_w for a small subregion of the white matter q_w :

$$q_g = \frac{1}{V_g} \int_{S_g} c(\tau, x, \omega) dx, \quad q_w = \frac{1}{V_w} \int_{S_w} c(\tau, x, \omega) dx, \quad (9)$$

where V_g and V_w is the volume of the gray and white matter subregions, respectively. The size and relative location of the subregions S_g and S_w within the computational domain are illustrated in Figure 1. To further quantify the speed of propagation, we define the white matter activation time F_w :

$$F_w(\omega) = \{\min t \mid \int_{\Omega_w} c(t, x, \omega) dx / n_0 > X\}, \quad (10)$$

where n_0 is the total amount of tracer injected into the SAS (0.5 mmol) and X is a given percentage. We here chose $X = 10\%$. Finally, we also define the analogous regional (white matter) activation time

$$f_w(\omega) = \{\min t \mid \frac{1}{V_w} \int_{S_w} c(t, x, \omega) dx > Y\}, \quad (11)$$

where $Y = 10^{-3} \text{ mol/m}^3$

For plotting the boundary tracer concentration over time, we define three axial planes along the z -axis ($z = -0.1, 0, 0.1 \text{ m}$) to represent the level of the foramen magnum, sylvian fissure and precentral sulcus, respectively.

2.3 Stochastic diffusion modelling

The parenchymal effective diffusion coefficient of a solute, such as e.g. gadobutrol, is heterogeneous [72] (varies in space) and individual-specific (varies from individual to individual). To investigate the effect of uncertainty in the diffusion coefficient, we consider two approaches: first, to model the diffusion coefficient as a random variable and second, to model the diffusion coefficient as a random field, thus allowing for tissue heterogeneity. Both approaches are described in further detail below.

Effective diffusion coefficient modelled as a random variable First, we consider the simplifying but common assumption that the effective diffusion coefficient is spatially homogeneous: $D^*(\omega) \in \mathbb{R}$. We account for the uncertainty in its value by modelling it as a random variable:

$$D^*(\omega) = 0.25 \times D_{\text{Gad}}^* + D_{\gamma}^*(\omega), \quad (12)$$

where $D_{\text{Gad}}^* = 1.2 \times 10^{-10} \text{ m/s}^2$ is a fixed parenchymal gadobutrol diffusivity [63] and where $D_{\gamma}^*(\omega)$ has a Gamma distribution with shape $k = 3$ and scale $\theta = 0.75 \times D_{\text{Gad}}^* / k$. The choice of shape and scaling parameters ensures that (i) the diffusion coefficient is positive, (ii) its expected value matches reported values of parenchymal gadobutrol diffusivity [63], and (iii) its variability allows for values up to 2–3 times larger or smaller than the average with low probability. The last modelling choice reflects diffusivity values in the range $1\text{-}10 \times 10^{-10} \text{ m/s}^2$ in agreement with previous reports[51]. The probability distribution of D^* is shown in Figure 2a.

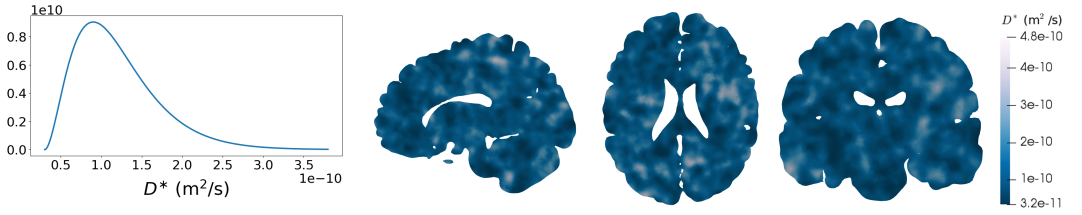


Figure 2: a): Assumed probability distribution of the homogeneous effective diffusion coefficient D^* modelled as a random variable and used in Model D1. The expected value $E[D^*] = 1.2 \times 10^{-10}$ (b) Sample of the heterogeneous effective diffusion coefficient (sagittal, axial and coronal slices ordered from left to right) modelled as a random field and used in Model D2.

Effective diffusion coefficient modelled as a random field In order to represent spatial heterogeneity in the diffusion coefficient, we next model D^* as a continuous random field. Again, we set

$$D^*(x, \omega) = 0.25 \times D_{\text{Gad}}^* + D_f^*(x, \omega), \quad (13)$$

where D_f^* now is a random field such that for each fixed $x \in \mathcal{D}$, $D_f^*(x, \omega)$ is a gamma-distributed random variable with the same parameters as $D^*(\omega)$ in (12). To enforce continuity and to easily sample the random field from its distribution, we draw samples of D_f^* by first sampling a Matérn field $X(x, \omega)$ and then transforming it into a gamma random field by using a copula[50]. This consists in setting $D_f^*(x, \omega) = F^{-1}(\Phi(X(x, \omega)))$, where F^{-1} is the inverse cumulative density function (CDF) of the target (gamma) distribution, Φ is the CDF of the standard normal distribution and $X(x, \omega)$ is a standard (zero mean, unit variance) Matérn field with smoothness parameter $\nu = 2.5$ and correlation length $\lambda = 0.01$ m, cf. (1). Note that spatial changes in the diffusivity occurs at a length scale corresponding to the correlation length, here 0.01 m.

2.4 Stochastic velocity modelling

In what follows we introduce three different models for the velocity field, each representing a different hypothesis regarding intraparenchymal ISF/CSF movement. We emphasize that each model represent a homogenized velocity field averaged over physiological structures.

Glymphatic velocity model: arterial influx and venous efflux To define a stochastic homogenized velocity model representing the glymphatic pathway, we assume that ISF follows separate inflow and outflow routes: entering the brain along paraarterial spaces and exiting along paravenous spaces[39]. We further suggest that

1. Substantial changes within the velocity field happen after a distance proportional to the mean distance between arterioles and venules.
2. The blood vessel structure is random and independent from the position within the parenchyma in the sense that the presence of paraarterial or paravenous spaces are equally likely at any point in space. Mathematically, this assumption requires the expected value of each of the velocity components to be zero.
3. The velocity field varies continuously in space and is divergence-free ($\nabla \cdot v = 0$), i.e. no CSF/ISF leaves the system e.g. through the bloodstream.

4. We set the expected velocity magnitude $\|v\| = \sqrt{v_x^2 + v_y^2 + v_z^2}$ to be $v_{\text{avg}} = 0.17 \mu\text{m/s}$ and we allow for up to 2-3 times larger and up to 10 times smaller values with low probability [51].

Although ISF/CSF velocities in paravascular regions may be higher [48] that what we propose, the velocity field here models an averaged bulk flow over a larger area (comprised of e.g. PVS and adjacent tissue). Bulk flow velocities in rats have been reported to be in the range of approximately $0.1\text{-}0.24 \mu\text{m/s}$ [1, 51].

To address these stipulations, we define the stochastic glymphatic circulation velocity field

$$v(x, \omega) = v_{\text{avg}} \cdot \eta(\lambda) 10^{-\mathcal{E}(\omega)} \left(\nabla \times \begin{bmatrix} X(x, \omega) \\ Y(x, \omega) \\ Z(x, \omega) \end{bmatrix} \right), \quad (14)$$

where $\eta(\lambda) = \lambda / \sqrt{(5 + 2\log(10))/200}$ is a scaling constant chosen such that the magnitude of v satisfies $\mathbb{E}[\|v\|^2]^{1/2} = v_{\text{avg}}$ (we omit the mathematical derivation of this constant), $\mathcal{E}(\omega)$ is an exponentially distributed random variable with mean 0.2 and $X(x, \omega)$, $Y(x, \omega)$ and $Z(x, \omega)$ are standard independent identically distributed (i.i.d) Matérn fields with $\nu = 2.5$ and correlation length $\lambda = 1020 \mu\text{m}$. A sample of the glymphatic circulation velocity field together with the velocity magnitude distribution is shown in Figure 3.

The factor $10^{-\mathcal{E}(\omega)}$ is an ad-hoc random term to enforce the variability requirement defined by point 4) above. The use of Matérn fields enforces spatial variability in a continuous manner and taking the curl operator ($\nabla \times$) ensures that the resulting velocity is divergence-free, hence addressing point 3). It can be proven (although we omit the details here) that the field within the brackets in (14) is still Gaussian, has zero mean (hence satisfies 2)) and has the same correlation length as the original Matérn fields, albeit it presents a slightly different covariance structure.

The choice of correlation length was guided by the following considerations. The mean distance between arterioles and venules was reported to be $280 \mu\text{m}$ in rhesus monkeys[4], although the value $250 \mu\text{m}$ has been used as a representative distance in humans in recent modeling papers [40, 59]. We estimated the mean distance in humans by considering differences in brain and artery size between monkey and human (Table 2). We find a factor close to 2 between CCA and arteriole diameter, while a similar ratio was found for the cube root of the brain mass. Thus, the correlation length should be greater than $250 - 560 \mu\text{m}$ to address point 1) above. Combining these physiological considerations with the corresponding requirements on the numerical resolution, we let $\lambda = 1020 \mu\text{m}$. It should be noted that this correlation length was used as a typical length between vessels of coherent PVS flow over the entire brain.

Species	Brain mass [g]	CCA diameter [mm]	Arteriole diameter [μm]	Dist. [μm]
Mouse	0.3 [65]	0.47 [43]	25 [38]	40*
Monkey	88 [65]	3.5[76]	35.5 [4]	280 [4]
Human	1350 [65]	6.3 [42]	40-250 [10]	1020*

Table 2: Brain-related parameters of three species. *: Estimated values. CCA: common carotid artery, Dist: distance between arteriole and venule

Glymphatic velocity model with additional directional velocity field Above we assumed that the blood vessel distribution was independent of the spatial position within the parenchyma and that bulk flow from arterial to venous PVS occurs on a small length scale proportional to the mean distance between arterioles and venules. However, transport of tracer might also happen on a larger length scale along

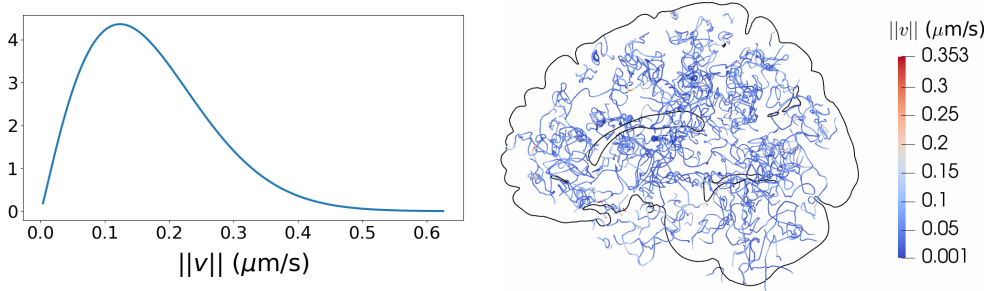


Figure 3: (a) Probability density of the glymphatic circulation velocity magnitude $\|v\|$ cf. (14). (b) Streamlines of a corresponding velocity field sample.

larger vascular structures present in given physical regions such as e.g. circle of Willis). AS CSF is hypothesized to enter the brain along penetrating arteries, the direction of cardiac pulse propagation may induce a directionality of the glymphatic circulation as well. The cardiac pulse follows the vessel paths of larger arteries entering the brain from below, and from there spreads out almost uniformly [41, 58]. The pulses also seem to traverse deep gray matter structures on the way up towards the ventricles.

To model such behavior, we introduce a directional velocity field v_{dir} , with characteristics qualitatively similar to what is described in the literature[41, 58];

$$v_{\text{dir}}(x) = -v_f \left(\arctan(15x_1)(|x_1| - 0.1), \arctan(15x_2) * (|x_2| - 0.1), -0.9x_3 + 0.06 - \sqrt{x_1^2 + x_2^2} \right), \quad (15)$$

where $v_f = 2 \times 10^{-6}$ m/s. For a plot of v_{dir} , see Figure 4. The velocity field v_{dir} induces a net flow out of the parenchyma at the very low rate of 0.007 mL/min. We superimpose this deterministic directional velocity field by the stochastic glymphatic circulation velocity field to define the stochastic glymphatic directional velocity field:

$$v(x, \omega) = v_{V1}(x, \omega) + v_{\text{dir}}(x), \quad (16)$$

where v_{V1} is given by (14). This velocity model thus takes into account both the "randomness" of small arteries, but also the "deterministic" presence of large arteries and possibly other structures of blood flow propagation[41, 58].

Capillary filtration model V3: arterial inflow with a homogeneous sink throughout the brain Several independent studies demonstrate that CSF may enter the brain parenchyma along spaces surrounding penetrating arteries [48, 39, 5, 14]. However, the glymphatic efflux concept of a bulk flow of CSF through the ECS and recirculation into the SAS through paravenous spaces has been severely questioned [34, 36, 5, 67]. As a variation, we here therefore also consider a stochastic velocity model representing paraarterial influx without a direct return route to the CSF. Instead, we assume that ISF/CSF is drained inside the brain parenchyma along some alternative efflux pathway. This pathway may include the capillaries or separate spaces along the PVS directly into cervical lymph nodes.

In light of this, we consider the following alternative velocity assumptions. (1) There is a net flow of CSF into the brain and (2) ISF is cleared within the parenchyma via some, here unspecified, route. For instance, it has been proposed that production and absorption is present all over the CSF system and that capillaries and ISF continuously exchanges water molecules [54]. However, drainage of large molecules through this route is unlikely as capillaries and the basement membranes are connected through tight



Figure 4: Velocity magnitude and streamlines for the directional velocity field v_{dir} as given by (15). The flow field is assumed to follow cardiovascular pulses upwards along the brain stem. After entering the deeper parts of the brain, the bulk flow spreads out at reduced velocity. (a) Sagittal view. (b) Coronal view. (c) Transverse view.

junctions [34]. It has also been reported that lymph vessels may be capable of also draining larger molecules from brain tissue into deep cervical lymph nodes, possibly through paravenous spaces[9]. In addition, other outflow routes may exist, including degradation clearance and meningeal lymphatic vessel clearance[69].

To address these assumptions, we define a stochastic arterial inflow velocity field as a radially symmetric field pointing inwards from the SAS interface to the brain region around the lateral ventricle. This central region is modelled in what follows as a sphere of radius $R = 8$ cm and center given by x_c in the lateral ventricles. Mathematical experimentation lead to the following *ansatz* for such velocity:

$$v(x, \omega) = \bar{v}(\omega) \exp\left(-\frac{3(R - \|x - x_c\|)^2}{R^2 - (R - \|x - x_c\|)^2}\right)(x - x_c), \quad (17)$$

where $\bar{v}(\omega)$ is a gamma random variable chosen such that the probability distribution of the velocity magnitude is comparable to that of the glymphatic circulation velocity defined by (14). The shape parameter $k = 2$ and the scale parameter is set such that again $\mathbb{E}[\|v\|^2]^{1/2} = v_{\text{avg}}$. Note that in this case, the expected value of the velocity components are non-zero. To satisfy (2), we model the drainage of tracer by setting $r = -1 \times 10^{-5} \text{ s}^{-1}$, which typically results in 40% drainage of the injected tracer over 48 hours.

2.5 Random field sampling and uncertainty analysis

We considered six output functionals of interest: the amounts of tracer in gray and white matter at given times (8), the average tracer concentrations in subregions of gray and white matter (9), the white matter activation time (10), and the white regional activation time (11). Each functional $Q = Q(\omega)$ depends on the random parameter ω via $c(\cdot, \cdot, \omega)$ as defined by (2). To sample the functional from its distribution, we first compute a sample of each of the random coefficients in (2) from their distribution, second, solve (2) with the given coefficient sample, and third, evaluate the functional with the computed solution. For sampling the random diffusion and velocity coefficient fields, we adopted a white noise sampling technique using an auxiliary extended domain[22]. We used the standard Monte Carlo approximation

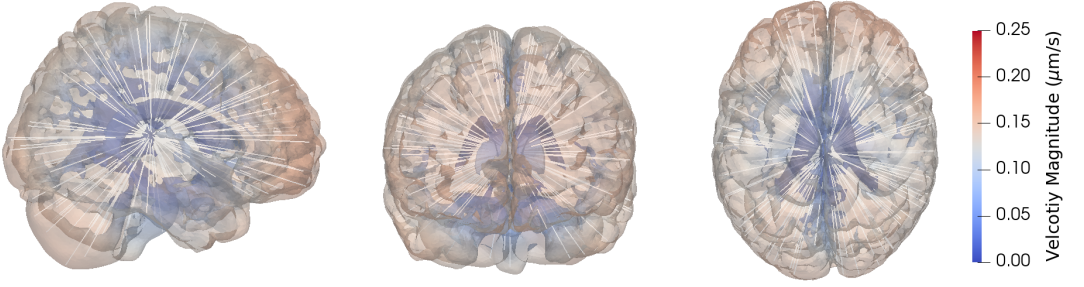


Figure 5: Velocity magnitude and streamlines for the velocity field as given by (17). Flow is assumed to occur from the cortex towards the ventricles with reduced velocity along the way due to clearance. (a) Sagittal view. (b) Coronal view. (c) Transverse view.

to estimate the expected functional value $\mathbb{E}[Q]$

$$\mathbb{E}[Q] \approx \hat{Q} = \frac{1}{N} \sum_{n=1}^N Q(\omega^n), \quad (18)$$

where N is the number of Monte Carlo samples. The statistical error introduced by approximating $\mathbb{E}[Q]$ with \hat{Q} decreases with $O(N^{-1/2})$. We let $N = 3200$ to ensure that $3(\hat{V}/N)^{1/2} < 0.01\hat{Q}$, where \hat{V} is the sample variance of \hat{Q} .

2.6 Numerical methods and implementation

The diffusion-convection equation (2) was solved numerically using a finite element method with continuous piecewise linear finite elements in space, and a second-order (implicit midpoint) finite difference discretization time with time step $\Delta t = 15$ min, combined with mass lumping[71]. The finite element mesh \mathcal{T}_h was an adaptively refined version of the gray and white matter of the Colin27 human adult brain atlas mesh [26] version 2 with 1875249 vertices and 9742384 cells. An outer box of dimensions $0.16 \times 0.21 \times 0.17$ (m^3) with mesh size 0.0023 m was used for the sampling of the Gaussian fields.

For the models with non-zero velocity (Models V1, V2, V3), (2) was typically mildly convection-dominated with an upper estimate of the Péclet number of

$$Pe \approx \frac{9Lv_{\text{avg}}}{D_{\text{Gad}}^*} \approx O(10^3), \quad (19)$$

where $L \approx 0.084$ m is half the diameter of the computational domain, $v_{\text{avg}} = 0.17 \mu\text{m/s}$, and $D_{\text{Gad}}^* = 1.2 \times 10^{-10} \text{ m}^2/\text{s}$. The boundary condition (7) was discretized explicitly in time using the trapezoidal rule; i.e. we let for each $n = 0, 1, \dots$:

$$c_{\text{CSF}}(t^{n+1}, \omega) = \frac{1}{V_{\text{CSF}}} \left(n_0 - \int_{\mathcal{D}} c(t^n, x, \omega) dx - \frac{\Delta t}{2} \left(2 \sum_{i=1}^{n-1} \int_{\mathcal{D}} rc(t^i, x, \omega) dx + \int_{\mathcal{D}} rc(t^n, x, \omega) dx \right) \right), \quad (20)$$

where $t^n = n\Delta t$ and the term in the inner bracket results from the numerical integration of the term $\int_0^{t^n} \int_D rc(t, x, \omega)$.

The numerical solver was verified using a convergence test comparing different mesh refinements, time steps, and stabilization techniques, including SUPG[24], for a set of deterministic worst-case models (with large velocities and small diffusion coefficients), see Figures 13 and 14.

The numerical solver was implemented in Python using the FEniCS finite element software [7] and previously verified in-house parallel Monte Carlo routines [22]. The extended box mesh was created using the Gmsh software [27]. The linear system was solved using the PETSc [12] implementation of the GMRES algorithm preconditioned with the BoomerAMG algebraic multigrid algorithm from Hypre [25]. We used Matplotlib (version 2.1.1) and Paraview (version 5.4.1) for visualization.

3 Results

3.1 Non-random diffusion as a baseline for parenchymal solute transport

To establish a baseline for parenchymal solute transport, we first simulated the evolution of a tracer spreading in the SAS and in the parenchyma via diffusion only, using a constant (i.e. non-random) effective diffusion coefficient for gadobutrol ($D^* = 1.2 \times 10^{-10} \text{ m}^2/\text{s}$). The resulting parenchymal tracer spread over 24 hours is shown in Figure 6. The tracer concentration increases first in inferior regions and in the gray matter. Tracer does not penetrate deep into white matter regions within this time frame. In the sagittal plane (top), tracer enhancement is more prominent than in the other two plane as the sagittal plane shown is close to the CSF-filled longitudinal fissure.

Figure 7a shows the boundary tracer concentration (concentration in the SAS) over time at the levels of the foramen magnum ($z = -0.1 \text{ m}$), sylvian fissure ($z = 0 \text{ m}$) and precentral sulcus ($z = 0.1 \text{ m}$). During the first few hours, boundary tracer concentration at the level of the foramen magnum increases rapidly, and peaks at 3 hours reaching approximately 2.0 mol/m^3 . Boundary tracer concentrations close to the sylvian fissure and precentral sulcus are lower, and the time to reach peak concentrations is longer. For the sylvian fissure, peak concentration in the CSF is 1.4 mol/m^3 , at 5 hours, while the precentral sulcus concentration reaches 1.1 mol/m^3 at 7 hours. We note that as the boundary condition depends on the parenchymal tracer concentration itself (cf. (7)), the boundary tracer concentration will differ slightly in subsequent simulation setups.

In Figure 7b, concentration profiles are shown for three interior points at different distances from the brain surface. The points were chosen along a line from the brain surface towards the ventricles at the height of the sylvian fissure ($z = 0$). The tracer concentration at these points stays low for the first few hours before steadily increasing. For the point closest to the SAS (x_2), the concentration rises faster than for the other two points, and is almost equal to the SAS concentration at 24 hours (0.4 vs 0.5 mol/m^3). In the middle point (x_1), tracer concentration starts increasing after 6-7 hours and reaches approximately 0.15 mol/m^3 after 24 hours. For the most interior point (x_0), tracer concentration starts and stays low throughout the 24 hour time span. At 24 hours, the tracer concentration in all three points is still increasing.

3.2 Quantifying the effect of uncertainty in effective diffusion magnitude

We first aimed to quantify the effect of uncertainty in the magnitude of the effective diffusion coefficient on the time evolution of tracer in the gray and white matter. In particular, we computed the tracer concentration, together with auxiliary output quantities, evolving via diffusion only with a gamma-distributed random variable diffusion coefficient (Model D1).

The amount of tracer found in the gray and white matter differ both in magnitude and variation (Figure 8a-c). The expected amount of tracer in the gray matter increases rapidly, and doubles from

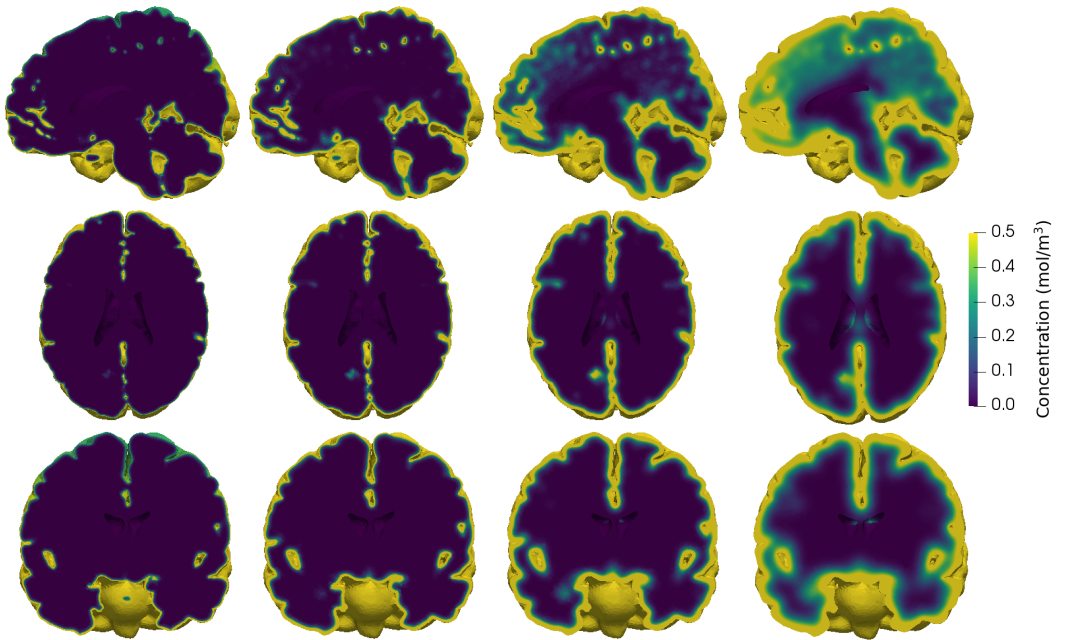


Figure 6: Parenchymal tracer concentration after (from left to right) 1, 3, 8 and 24 hours of diffusion in (from top to bottom) sagittal, transverse and coronal planes. Initially, most of the tracer is found in inferior regions. At 24 hours, tracer has penetrated substantially into the gray matter, but not into the deep, central regions.

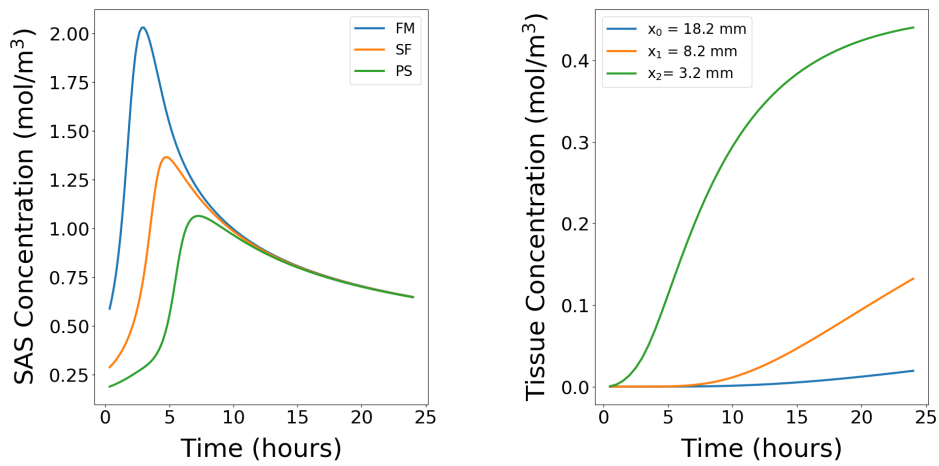


Figure 7: (a) Tracer concentration in the SAS (c_{CSF}) used as boundary conditions at the brain surface at the level of the foramen magnum (FM), sylvian fissure (SF) and the precentral sulcus (PS). At the lower level of the SAS, tracer concentration peaks at around 3 hours, while at the upper levels, peak concentration occurs later. Following peak values, the concentration in the SAS decreases as tracer enters the parenchyma. The SAS concentration is modeled by (5) (b) Tracer concentration over time in three different points at a given distance from the brain surface. The points were chosen along a line directly from the cortex towards the ventricles at the level of the sylvian fissure.

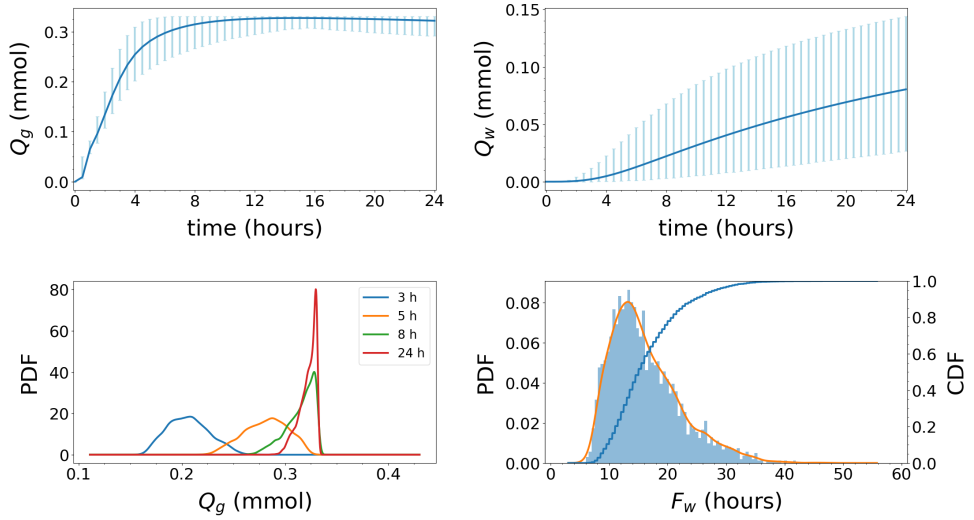


Figure 8: Model D1. The integrated amount of tracer in the (a) gray matter Q_g and (b) white matter Q_w over time; Q_g and Q_w as defined by (8). The blue curves show the expected value. The light blue vertical bars indicate the variability: 99.73% of the samples fall within the plotted range (with 0.135% of the samples above and 0.135% below). (c) The probability density functions (PDFs) corresponding to Q_g at 3, 5, 8 and 24 hours after tracer injection. (d) Histogram of white matter activation time F_w as defined by (10) (bars), corresponding estimated PDF (orange curve), and corresponding cumulative density function (CDF). Uncertainty in the magnitude of the effective diffusion coefficients substantially impact the amount of tracer found in the gray and white matter and the white matter activation time.

1 to 2 hours (0.065 to 0.13 mmol), and again from 2 to 4 hours (0.13 mmol to 0.25 mmol). The gray matter reaches a peak after approximately 15 hours, while the white matter did not reach steady state within 24 hours. There is substantial variation in the amount of tracer in gray matter throughout the 24 hour time span. The variation is at its largest between 2 and 8 hours where the length of the 99.73%-intervals range from 0.064 mmol to 0.11 mmol corresponding to 13-22% of the total tracer injection of 0.5 mmol. Ultimately, the amount of tracer will reach a steady-state solution, constant in space and time, independently of the diffusion coefficient. Therefore, after a certain point in time, variation decreases as all solutions converge towards the same steady state. The changes in variation of tracer found in the gray matter over the 24 hours are also illustrated by the change in the PDF of the total amount of tracer at a given time (Figure 8c). After 3 and 5 hours (blue and orange curve) the PDFs are symmetric, and with more spread for the later time point. As time evolves, the PDFs become more left skewed (green and red curve), as in almost all cases, the concentration approaches but never surpasses the steady state value.

The amount of tracer in the white matter changes slowly for the first two hours, before starting to increase after 3-4 hours (Figure 8b). After 4 hours, the expected amount of tracer in the white matter is only 0.0048 mmol, increasing to 0.022 mmol after 8 hours, and 0.056 mmol after 16 hours. The variation is substantial and increasing with time: the length of the 99.73%-interval is 0.022 mmol at 4 hours, 0.065 mmol at 8 hours and 0.10 at 16 hours. At 24 hours, the uncertainty in diffusion coefficient may explain a factor of approximately 5 in deviation from the lowest (0.027 mmol) to the highest (0.14 mmol) predicted amount of tracer in the white matter.

The estimated probability density function (PDF) and cumulative density function (CDF) for the white matter activation time (i.e. time for 10% of tracer to reach the white matter) is shown in Figure 8d. We observe that the most likely white matter activation time is approximately 14 hours. The white matter activation time is less (than 10%) likely to be less than 9.5 hours, but (more than 90%) likely to be less than 24.5 hours. The activation time may exceed 24 hours, but is highly unlikely to go beyond 40 hours (CDF > 0.998). The white matter activation threshold was reached in all samples within the simulation time span.

3.3 Quantifying the effect of uncertainty in diffusion heterogeneity

Brain tissue is heterogeneous [72], varies from individual to individual, and is clearly not accurately represented by a single diffusion constant. To further investigate the effect of uncertainty in the diffusion coefficient and in particular to study the effect of spatial heterogeneity, we modelled the diffusion coefficient as a spatially-varying random field (Model D2).

The amounts of tracer found in gray and white matter for Model D2 are nearly identical to those resulting from Model D1 in terms of expected value (data shown later cf. Figure 11), but with substantially less variability. The length of the 99.73% confidence interval for amount of tracer in gray matter (Q_g) is less than 0.0071 mmol for all times after the first half hour, corresponding to a relative variability (compared to the expected value) of between 2.2 and 10.9% throughout the 24 hour time span. For white matter, the length of the 99.73% confidence interval is increasing with time, with the relative variability at 24 hours at 7.9%.

When considering the average concentration of tracer in two smaller regions of interest (cf. (9)), variability in model D2 increases drastically (Figure 9). In the gray matter region (Figure 9a), the expected average tracer concentration increases steadily to 0.11 mol/m³ after 4 hours, 0.23 mol/m³ after 8 hours, 0.35 mol/m³ after 16 hours and is still increasing after 24 hours. The variability is moderate after 3 hours (Figure 9c), but increases thereafter. The length of the 99.73% confidence interval peaks at 0.39 mol/m³ after 11 hours before decreasing moderately for later times.

The expected average tracer concentration in the white matter is low, lower than in the gray matter (Figure 9b) by a factor of at least 40, and starts increasing only after approximately 14 hours. For the

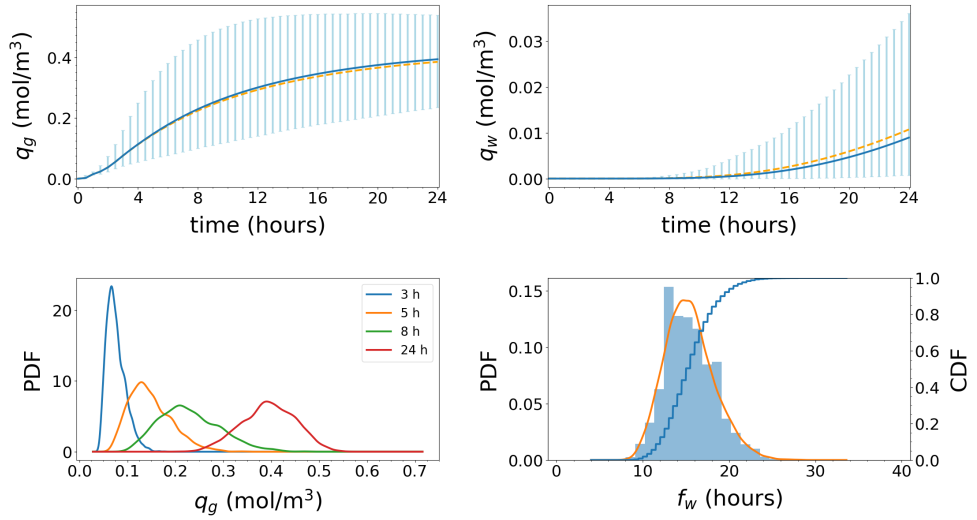


Figure 9: Model D2. The average tracer concentration in a subregion of (a) gray matter q_g and (b) white matter q_w as defined by (9). The blue curves show the expected value. The light blue vertical bars indicate the variability: 99.73% of the samples fall within the plotted range (with 0.135% of the samples above and 0.135% below). The dashed orange lines in (a) and (b) indicate the analogous expected value curve resulting from Model D1 (constant diffusion only), for comparison. (c) The probability density functions (PDFs) corresponding to q_g at 3, 5, 8 and 24 hours after tracer injection. (d) Histogram of white subregion activation time f_w as defined by (11) (bars), corresponding estimated PDF (orange curve), and corresponding cumulative density function (CDF). Uncertainty in the heterogeneity of the diffusion coefficient leads to a wide range of likely average tracer concentrations in the white matter throughout the time span.

samples in the lower range of the 99.73% interval (thus with the lower effective diffusivity), the concentration in the white matter region remains close to zero after 24 hours. For the white region activation time, we observe some variability (Figure 9d): the peak likelihood is after 14-15 hours, less (than 10%) likely to be less than 12 hours, and (more than 90%) likely to be less than 19 hours. The white subregion activation threshold was reached in all samples within the simulation time span.

3.4 Quantifying the effect of glymphatic circulation

In light of the substantial uncertainty surrounding ISF/CSF flow in paravascular/perivascular spaces and potential ISF flow in extracellular spaces, we now turn to study the effect of uncertain velocity fields. To investigate the effect of uncertainty in a glymphatic velocity model, we defined a random velocity field with correlation length corresponding to the typical distance between parenchymal arterioles and venules (Model V1).

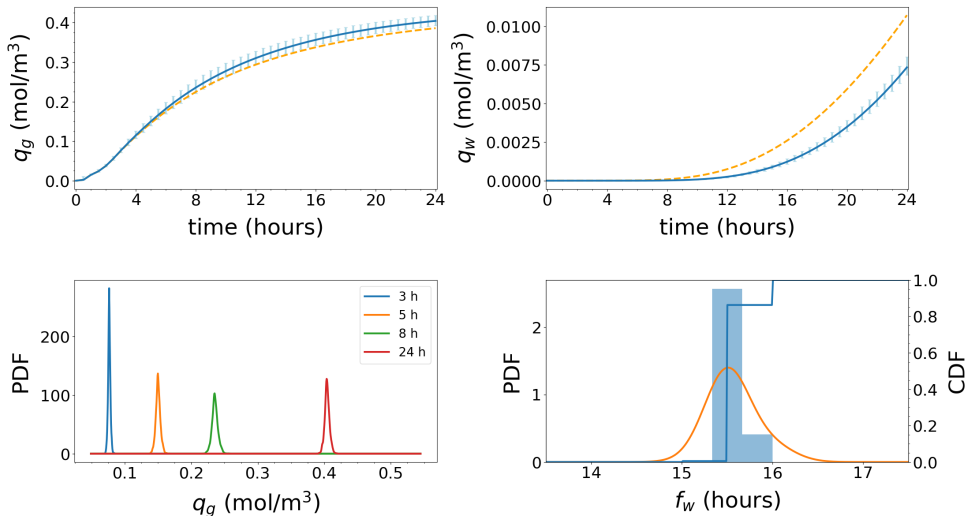


Figure 10: Model V1. The average tracer concentration in a subregion of (a) gray matter q_g and (b) white matter q_w as defined by (9). The blue curves show the expected value. The light blue vertical bars indicate the variability: 99.73% of the samples fall within the plotted range (with 0.135% of the samples above and 0.135% below). The dashed orange lines in (a) and (b) indicate the analogous expected value curve resulting from Model D1 (constant diffusion only), for comparison. Expected values for q_g are nearly identical as for Model D1 and D2, but variation is much lower. Expected values for q_w are lower than for Model D1 and variation is much lower (c) The probability density functions (PDFs) corresponding to q_g at 3, 5, 8 and 24 hours after tracer injection. The PDFs show very low variation. Variation increases slightly over time. (d) Histogram of white subregion activation time f_w as defined by (11) (bars), corresponding estimated PDF (orange curve), and corresponding cumulative density function (CDF).

The expected amounts of tracer found in the whole gray and whole white matter for Model V1 are nearly identical to those found for Model D2 and Model D1, while the variability is minimal (data shown

later cf. Figure 11). Thus, on average, small random variations in fluid velocity did not increase (or decrease) the tracer distribution into the parenchyma on a global scale. This observation can be interpreted in the light of the small correlation length of the velocity field compared to the size of the whole gray and white matter.

The expected average tracer concentration in the gray subregion q_g reaches 0.2 mol/m^3 in 7 hours (Figure 10a). This is a considerable amount of time, given that the initial average SAS concentration is 3.57 mol/m^3 . The expected average tracer concentration in the white subregion q_w is lower, and only reaches 7.3 mmol/m^3 in 24 hours (Figure 10b). We observe that the expected q_g increases marginally faster with the glymphatic velocity model than for pure diffusion: at 24 hours, q_g is 2.5% higher for V1 (0.40 mol/m^3) than for D1 (0.39 mol/m^3). On the other hand, the expected q_w increases faster with pure diffusion than with the glymphatic velocity model: at 24 hours, q_w is 34% lower for V1 (0.0073 mol/m^3) than for D1 (0.011 mol/m^3). The peak relative difference between pure diffusion and the upper limit of the 99.73% interval of model V1 is high after one hour, due to low tracer concentration overall. The next peak occurs after 8 hours where the relative difference is 13 % between the two.

However, the variation in both gray and white local average tracer concentration is small. For early time points (up to 3-4 hours), nearly no variation is evident in the average tracer concentration of the local regions (Figure 10a-c). The peak length of the 99.73% interval for q_g is 0.035 mol/m^3 (at 9 hours), and the relative variability ranges from 6-19% in the 24 hour time span. Moreover, the activation time f_w shows low variability: all simulations resulted in an activation time of 15.5-16 hours (Figure 10d). The substantially reduced variability for V1 compared to e.g. D2 combined with the comparable expected values yields much larger likely sample ranges for D2 than for V1.

3.5 Quantifying the effect of glymphatic directionality

The cardiovascular pulse propagates along the larger arteries entering the brain from below before spreading outwards[41, 58]. To assess whether and how such a directionality in the glymphatic system affects parenchymal tracer distribution, we added a net flow field to the random velocity field representing the glymphatic circulation (Model V2).

With more fluid entering the brain from below, as illustrated by the streamlines of Figure 4, the total parenchymal amount of tracer increases. For the expected amount of tracer in gray matter, however, Model V2 was in very good agreement with Models D1 and V1 (Figure 11a). After 13 hours, the amount of tracer found in the gray matter is higher for Model D1 than for Model V2. In Model V2, more of the tracer is found deeper in the gray matter and eventually moves to the white matter. We note that the uncertainty associated with the velocity fields barely affects the amount of tracer in the gray and white matter, as demonstrated by the nearly vanishing variation associated with Q_g and Q_w for Model V2 (and V1) (Figure 11a-b).

The expected amount of tracer in the white matter Q_w increases substantially by the introduction of the directional velocity field (Figure 11b). The expected value curve starts deviating from the other models after 4-5 hours, and the difference increases with time. At 24 hours, the expected amount of tracer found in the white matter Q_w is 50% larger for Model V1 (0.12 mmol) as for Model D1 (0.08 mmol). However, in view of the large variability associated with Q_w for Model D1 and the nearly vanishing variability associated with Model V2, the expected amount of white matter tracer for Model V2 falls well within the 99.73% confidence interval for Model D1.

The directional velocity field also induces an increase in the expected average tracer concentration in the gray subregion q_g (0.45 mol/m^3 vs 0.40 for V1 and 0.39 mmol/m^3 for D1 at 24 hours, Figure 11c). In contrast to for Q_g and Q_w , this functional also displays some variability, with a peak variability (0.031 mol/m^3 i.e. 10%) at 8-10 hours after injection. Notably, after 21-22 hours, the average tracer concentration in gray matter is larger than for pure diffusion (and for no net flow) also in terms of 99.73% con-

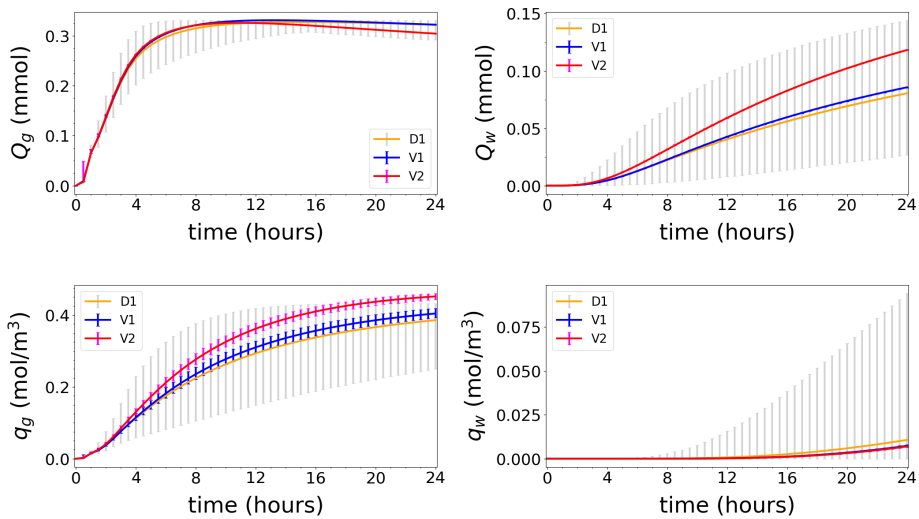


Figure 11: Model V2 (red) in comparison with Models D1 (orange) and V1 (blue). The integrated amount of tracer in the (a) gray matter Q_g and (b) white matter Q_w , as defined by (8), over time. The average tracer concentration in a subregion of (c) gray matter q_g and (d) white matter q_w , as defined by (9), over time. The curves show the expected values while vertical bars indicate the 99.73% confidence intervals of the different models.

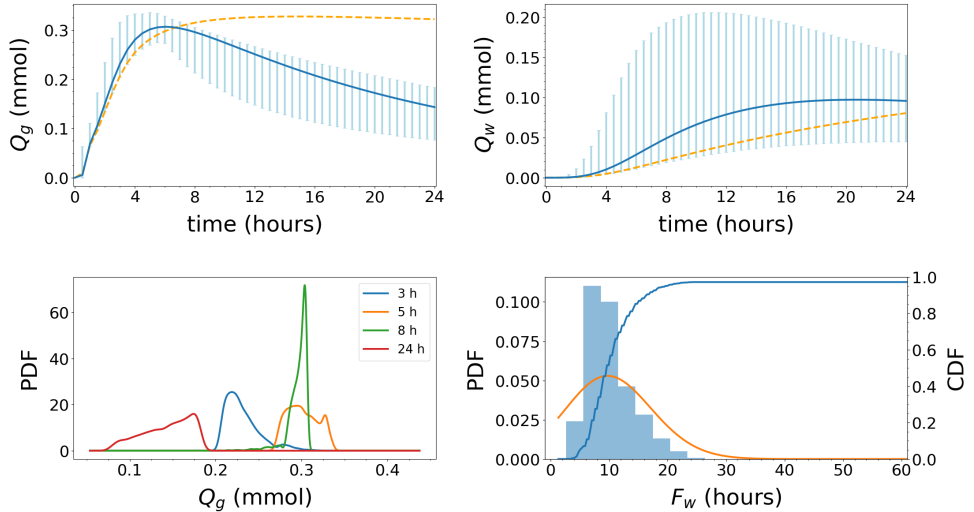


Figure 12: Model V3. The integrated amount of tracer in the (a) gray matter Q_g and (b) white matter Q_w over time; Q_g and Q_w as defined by (8). The blue curves show the expected value. The light blue vertical bars indicate the variability: 99.73% of the samples fall within the plotted range (with 0.135% of the samples above and 0.135% below). The dashed orange lines in (a) and (b) indicate the analogous expected value curve resulting from Model D1 (constant diffusion only), for comparison. Large variations in the white matter is found depending on the inflow velocity. (c) The probability density functions (PDFs) corresponding to Q_g at 3, 5, 8 and 24 hours after tracer injection. (d) Histogram of white matter activation time F_w as defined by (10) (bars), corresponding estimated PDF (orange curve), and corresponding cumulative density function (CDF). We note that the CDF peaks at 0.96 (< 1.0) as some samples never reached the white region activation threshold.

fidence intervals. For q_w , Model V1 and V2 are in close agreement, both with distinctly less variability than Model D1 (Figure 11d).

3.6 Quantifying the effect of paraarterial influx with drainage

A number of open questions remain in the context of glymphatic and paravascular efflux routes. To further investigate potential pathways, we also considered a model representing paraarterial influx combined with parenchymal ISF drainage (Model V3).

Pararterial inflow with drainage increases the amount of tracer found in the parenchyma for the early time points (Figure 12). After 4 hours, with the lowest velocities, the amount of tracer in the gray matter is equal to models with only diffusion (0.25 mmol). With higher velocities, however, the amount of tracer found in the gray matter increases by 32% to reach 0.33 mmol. After a peak at 6-8 hours, drainage and transport into white matter cause a decrease in the expected amount of tracer in the gray matter, while its variation stays more or less constant (0.11-0.12 mmol). The PDFs of the amount of tracer found in the gray matter thus have different characteristics than the two previous models, in particular

the red curve (24 hours) shows lower amounts of tracer than at the two previous time points.

For the white matter, the expected amount of tracer increases with time, rapidly in comparison with pure diffusion, and seems to peak at approximately 0.097 mmol (at 19-22 hours) before slowly decreasing. Variation, on the other hand, is substantial and in some cases the amount of tracer found in the white matter reaches 0.2 mmol, which higher than what is seen in any previous model. This is visible by a peak of the maximum values within the 99.73% interval after 11-12 hours. In Model V3, tracer is drained out of the system and the amount of tracer in the white matter is similar as for the previous models at 24 hours.

The white matter activation time is likely lower for Model V3 compared to previous models, and the variation is substantial (Figure 12d). The white matter activation time is less (than 10%) likely to be less than 6 hours, but (more than 90%) likely to be less than 16.5 hours. Note that the white matter activation threshold was not reached in 3% of the samples.

4 Discussion

In this study, we have investigated the variability in parenchymal tracer enhancement resulting from uncertainty in diffusion and convection parameters. We designed five computational models representing different diffusion and convection regimes and used stochastic analysis to rigorously evaluate the resulting probability distributions.

In all models, 10% of the tracer reached the white matter within 40 hours, with more variability in activation time for diffusion models and less variability for models including a convective velocity. Indeed, uncertainty in the diffusion parameters had a substantial impact on the amount of tracer in gray and white matter, and on the average tracer concentration in gray and white subregions. Overall, diffusion was not sufficient, with high likelihood, to transport tracer deep into the parenchyma.

A stochastic velocity field representing the glymphatic theory did not increase transport into any of the regions considered, unless augmented with an additional net flow with a prescribed directionality. In the latter case, transport was increased with overwhelming likelihood: for model V2, the entire 99.73% confidence interval for the gray subregion average tracer concentration was higher than for model D1. Models including parenchymal drainage displayed substantial variability, and reached peak values for the expected amount of tracer both in gray and white matter within 24 hours.

4.1 Comparison with previous work

Our models mimic the experimental set-up of an MRI study of parenchymal tracer distribution after intrathecal gadobutrol injection [64]. In our simulations, as in the MRI study, the tracer first spreads to inferior regions of the parenchyma closer to the (modelled) injection site. Modelling a healthy patient, we assumed that the tracer concentration in the ventricular CSF was low [64, 63]. Thus, no tracer spreads to the parenchyma from the ventricles directly. In models with diffusion only, the amount of tracer in the gray matter peaks at approximately 15 hours. In the MRI study, the time to peak enhancement in selected regions of interest was between 12 and 24 hours [64]. In a more recent study, time to peak values were considerably longer, up to 48 hours, for some regions [63]. However, in the latter study, the time to peak enhancement was shorter for the white matter than for the gray matter in healthy subjects. This observation is not consistent with the results from either of our computational models.

Most of the reported time to peak values in the two human MRI-studies [64, 63] are within the 99.73% confidence interval of the random homogeneous diffusion model (Model D1). However, even for the upper range of the confidence interval, the time to peak/steady state value for the white matter exceeds 24 hours in our model. The uncertainty in the diffusion coefficient may explain a four-fold difference in

the amount of tracer found in the white matter at 24 hours. Despite this large variation, the discrepancy between simulations and experiments in white matter could not be explained by uncertainty in the diffusion parameter. This may suggest other mechanisms in addition to diffusion for tracer transport into deeper regions of the brain. According to paraarterial influx theories in general and the glymphatic theory in particular, tracer flows rapidly along and into the parenchymal PVS[37] distributing tracer to the gray matter. Hence, one may expect diffusion models to underestimate the amount of tracer in gray matter at a given time. However, it is worth noting that we do not observe such an underestimation in our diffusion model, when compared to the experimental values[64]. In contrast, we do observe a delayed distribution of tracer in white matter.

Brain tissue is known to be both anisotropic and heterogeneous[51, 62, 77]. We found the variation due to spatial heterogeneity in the diffusion coefficient to be low. As the correlation length was small compared to the size of the gray and white matter, a lack of tracer concentration in one local region was balanced by enhancement in a different local region. In addition, we note that representing the diffusion coefficient as a random variable or a random field yields the same expected value. Tracer distribution to large brain regions can thus be well approximated using an average diffusion constant if the spatial heterogeneity is present on a shorter length scale.

In models with convection, given a homogenized velocity of average magnitude $0.17 \mu\text{m/s}$, tracer distribution depends on the characteristics of the velocity field. In the glymphatic theory, CSF enters the brain along arteries and re-enters the SAS along a paravenous efflux pathway[39, 37]. In our glymphatic circulation model, the stochastic velocity field, representing homogenized paraarterial and paravenous flow, did not increase tracer distribution to the brain. An increase in the amount of tracer surrounding paraarterial spaces was balanced by a lower distribution around paravenous spaces. However, when local regions are addressed, tracer concentration may increase by up to 13% compared to diffusion alone, depending on the surrounding velocity field and region of interest. As we consider a homogenized representation of the PVS, this change reflects an increase in regions surrounding arterial PVS (not only inside the PVS). Iliff et al. [38] reported a 2-fold increase in tracer intensity in PVS in normal mice compared to mice with internal carotid artery ligation. The increase in the surrounding parenchyma was lower, approximately 30-40%, which compares more naturally with our estimate of 13%. It should be noted however, that our region of interest was deeper into the parenchyma (extending from 0.6 to 4 mm depth) than the region of interest (at $100 \mu\text{m}$) used by Iliff et al. [38]. Moreover, our model parameters reflect a different species (man versus mouse), and the tracer spread takes place at a longer time scale.

When modelling paraarterial influx combined with parenchymal drainage (Model V3), the time to peak was reduced to 6-8 hours in the gray matter. Although lacking quantitative drainage parameters, we observe that substantial clearance would reduce both the time to peak and relative tracer enhancement in the brain compared to diffusion alone. In the glymphatic directionality model (Model V2), guided by [58], the presence of a paravascular directional velocity also decreases the expected time to peak tracer enhancement in gray matter, down to 11 hours (compared to 15 hours for pure diffusion). Thus, when experimental data suggests a time to peak enhancement shorter than for diffusion alone, it is not clear whether this is due to increased glymphatic function or increased clearance by parenchymal drainage.

In our models, the white matter (and subregions) is where the effect of a convective velocity becomes most prominent. The only model modification causing an expected time to peak enhancement in white matter of approximately 24 hours is with a paraarterial inflow and drainage (Model V3). In this model, the upper limit of the 99.73% confidence interval peaks at approximately 12 hours, which is more comparable to the rapid tracer enhancement observed in the white matter of healthy subjects[63].

Although diffusion may act as the main transport mechanism in the parenchyma [68, 36], we here show that convective velocities of magnitude less than $1 \mu\text{m/s}$ may play an important role for transport. This result holds when there is a structure of the glymphatic circulation as used in Model V2 or possibly a net inflow as in Model V3. It should be noted that this directional velocity field, in which pulsations

propagate upwards from the brain stem[41, 58], favors inflow when tracer is injected in lower CSF regions such as e.g. in the spinal canal.

4.2 Limitations

In the present study, we have used a continuous model of the brain parenchyma allowing only for an homogenized representation of paravascular spaces on the scale of micrometers. To remedy this limitation, combined with restrictions placed by mesh resolution, we used lower velocities acting over larger areas to model paravascular flows. In addition, the correlation length of which we expect flow to be coherent is constant in the entire brain. This is despite the shortening length scale as arterioles become capillaries. Thus, the correlation length we use may act as an upper limit. Even when using this upper limit of the correlation length, tracer enhancement was not increased due to the random convective velocity field. A smaller correlation length for capillaries will not change this result.

Further, we did not distinguish between white and gray matter in terms of the fluid velocity or in the diffusivity, although white matter is assumed to be more permeable [56]. However, in the absence of substantial drainage, net movement of fluid (in gray matter and PVS vs white matter) should on average be equal in the two regions by conservation of mass. Therefore, we used maximal velocity magnitudes of approximately $0.5 \mu\text{m/s}$, which is similar to what has been reported in white matter [1], but not as high as has been reported in local regions in the PVS[14, 48]. While we used qualitative measurements [41, 58] to suggest a directionality in the glymphatic circulation, we predict that more detailed measurements of glymphatic function in different brain regions would be important for tracer enhancement and clearance.

The boundary concentration in our model was assumed to spread in a manner similar to what was seen from the signal intensity in the MRI study by Ringstad et al[64]. A more detailed analysis of the spread of tracer in the CSF could be based on at least solving the Navier-Stokes equations in the SAS. In addition, our model ignores other efflux pathways directly from the SAS such as e.g. arachnoid granulations[29], dural lymphatics[46, 45], and nasal lymphatics[49], although lymphatic drainage of CSF has recently been proposed to dominate glymphatic clearance [47].

In the experiments by Ringstad et al. [64, 63], tracer distribution within the parenchyma varied considerably from patient to patient. In our analysis, we did not consider patient-specific meshes, but rather one representative mesh. Patient-specific meshes would add additional dimensions to the space of uncertainty, possibly giving different distributions in output in each of the patients.

The MRI-studies[64, 63] only provide quantitative values of tracer enhancement signal intensity, and not tracer concentrations. As the relation between signal intensity and concentration is nonlinear[20], we have not made a direct comparison between these two quantities. However, we have assumed that a peak in signal intensity corresponds to a peak in tracer concentration, thus allowing for a comparison of time-to-peak between the model results and experiments.

5 Conclusions

The results from this study show that uncertainty in the diffusion parameters substantially impact the amount of tracer in gray and white matter, and the average tracer concentration in gray and white sub-regions. However, even with an uncertainty in the diffusion coefficient of a factor three, and a resulting four-fold variation in white matter tracer enhancement, discrepancies between simulations of diffusion and experimental data are too large to be attributed to uncertainties in the diffusion coefficient alone.

A convective velocity field, representing the glymphatic circulation, increases tracer enhancement in the brain as compared to pure diffusion. However, increased enhancement is reliant on a directional

structure of the velocity field allowing for efficient inflow from given regions.

Diffusion alone was able to mimic behaviour in MR-studies in specific regions. However, this result does not imply lack of glymphatic circulation as the gray matter tracer enhancement was equal for the glymphatic model with directionality and for diffusion alone. However, the white matter concentration was greatly increased in the former model. Thus measuring glymphatic function requires detailed experimental data and analysis of the whole brain.

References

- [1] N. J. Abbott. Evidence for bulk flow of brain interstitial fluid: significance for physiology and pathology. *Neurochemistry international*, 45(4):545–552, 2004.
- [2] N. J. Abbott, M. E. Pizzo, J. E. Preston, D. Janigro, and R. G. Thorne. The role of brain barriers in fluid movement in the CNS: is there a 'glymphatic' system? *Acta neuropathologica*, pages 1–21, 2018.
- [3] P. Abrahamsen. *A Review of Gaussian Random Fields and Correlation Functions*. Norwegian Computing Center, 2 edition, 1997.
- [4] D. L. Adams, V. Piserchia, J. R. Economides, and J. C. Horton. Vascular supply of the cerebral cortex is specialized for cell layers but not columns. *Cerebral Cortex*, 25(10):3673–3681, 2015.
- [5] N. J. Albargothy, D. A. Johnston, M. MacGregor-Sharp, R. O. Weller, A. Verma, C. A. Hawkes, and R. O. Carare. Convective influx/glymphatic system: tracers injected into the csf enter and leave the brain along separate periarterial basement membrane pathways. *Acta neuropathologica*, 136(1):139–152, 2018.
- [6] R. Aldea, R. O. Weller, D. M. Wilcock, R. O. Carare, and G. Richardson. Cerebrovascular smooth muscle cells as the drivers of intramural periarterial drainage of the brain. *Frontiers in aging neuroscience*, 11, 2019.
- [7] M. Alnæs, J. Blechta, J. Hake, A. Johansson, B. Kehlet, A. Logg, C. Richardson, J. Ring, M. E. Rognes, and G. N. Wells. The FEniCS project version 1.5. *Archive of Numerical Software*, 3(100):9–23, 2015.
- [8] M. Asgari, D. De Zélicourt, and V. Kurtcuoglu. Glymphatic solute transport does not require bulk flow. *Scientific reports*, 6:38635, 2016.
- [9] A. Aspelund, S. Antila, S. T. Proulx, T. V. Karlsen, S. Karaman, M. Detmar, H. Wiig, and K. Alitalo. A dural lymphatic vascular system that drains brain interstitial fluid and macromolecules. *Journal of Experimental Medicine*, 212(7):991–999, 2015.
- [10] R. N. Auer. Histopathology of brain tissue response to stroke and injury. In *Stroke (Sixth Edition)*, pages 47–59. Elsevier, 2016.
- [11] E. N. Bakker, D. M. Naessens, and E. VanBavel. Paravascular spaces: entry to or exit from the brain? *Experimental physiology*, 2018.
- [12] S. Balay, S. Abhyankar, M. Adams, J. Brown, P. R. Brune, K. Buschelman, V. Eijkhout, W. Gropp, D. Kaushik, M. G. Knepley, and Others. PETSc users manual revision 3.8. Technical report, Argonne National Laboratory, ANL, 2017.

- [13] O. Balédent, C. Gondry-Jouet, M.-E. Meyer, G. De Marco, D. Le Gars, M.-C. Henry-Feugeas, and I. Idy-Peretti. Relationship between cerebrospinal fluid and blood dynamics in healthy volunteers and patients with communicating hydrocephalus. *Investigative radiology*, 39(1):45–55, 2004.
- [14] B. Bedussi, M. Almasian, J. de Vos, E. VanBavel, and E. N. Bakker. Paravascular spaces at the brain surface: Low resistance pathways for cerebrospinal fluid flow. *Journal of Cerebral Blood Flow & Metabolism*, 38(4):719–726, 2017.
- [15] B. Bedussi, M. G. Lier, J. W. Bartstra, J. Vos, M. Siebes, E. VanBavel, and E. N. Bakker. Clearance from the mouse brain by convection of interstitial fluid towards the ventricular system. *Fluids and Barriers of the CNS*, 12(1):23, 2015.
- [16] B. Bedussi, N. N. van der Wel, J. de Vos, H. van Veen, M. Siebes, E. VanBavel, and E. N. Bakker. Paravascular channels, cisterns, and the subarachnoid space in the rat brain: A single compartment with preferential pathways. *Journal of Cerebral Blood Flow & Metabolism*, 37(4):1374–1385, 2017.
- [17] J. Biehler, M. W. Gee, and W. A. Wall. Towards efficient uncertainty quantification in complex and large-scale biomechanical problems based on a Bayesian multi-fidelity scheme. *Biomech Model Mechanobiol*, 14:489–513, 2015.
- [18] R. Carare, M. Bernardes-Silva, T. Newman, A. Page, J. Nicoll, V. Perry, and R. Weller. Solutes, but not cells, drain from the brain parenchyma along basement membranes of capillaries and arteries: significance for cerebral amyloid angiopathy and neuroimmunology. *Neuropathology and applied neurobiology*, 34(2):131–144, 2008.
- [19] J. Charrier, R. Scheichl, and A. L. Teckentrup. Finite element error analysis of elliptic PDEs with random coefficients and its application to multilevel Monte Carlo methods. *SIAM Journal of Numerical Analysis*, 51(1):322–352, 2013.
- [20] X. Chen, G. W. Astarý, H. Sepulveda, T. H. Mareci, and M. Sarntinoranont. Quantitative assessment of macromolecular concentration during direct infusion into an agarose hydrogel phantom using contrast-enhanced MRI. *Magnetic resonance imaging*, 26(10):1433–1441, 2008.
- [21] K. A. Cliffe, M. B. Giles, R. Scheichl, and A. L. Teckentrup. Multilevel Monte Carlo methods and applications to elliptic PDEs with random coefficients. *Computing and Visualization in Science*, 14(1):3–15, 2011.
- [22] M. Croci, M. B. Giles, M. E. Rognes, and P. E. Farrell. Efficient White Noise Sampling and Coupling for Multilevel Monte Carlo with Nonnested Meshes. *SIAM/ASA Journal on Uncertainty Quantification*, 6(4):1630–1655, 2018.
- [23] A. K. Diem, M. MacGregor Sharp, M. Gatherer, N. W. Bressloff, R. O. Carare, and G. Richardson. Arterial pulsations cannot drive intramural periarterial drainage: significance for A β drainage. *Frontiers in neuroscience*, 11:475, 2017.
- [24] H. C. Elman, D. J. Silvester, and A. J. Wathen. *Finite elements and fast iterative solvers: with applications in incompressible fluid dynamics*. Oxford University Press, USA, 2014.
- [25] R. D. Falgout and U. M. Yang. Hypre: A library of high performance preconditioners. In *International Conference on Computational Science*, pages 632–641. Springer, Springer, 2002.

- [26] Q. Fang. Mesh-based Monte Carlo method using fast ray-tracing in Plücker coordinates. *Biomedical optics express*, 1(1):165–175, 2010.
- [27] C. Geuzaine and J.-F. Remacle. Gmsh: A 3-D finite element mesh generator with built-in pre-and post-processing facilities. *International journal for numerical methods in engineering*, 79(11):1309–1331, 2009.
- [28] L. Guo, J. C. Vardakis, T. Lassila, M. Mitolo, N. Ravikumar, D. Chou, M. Lange, A. Sarrami-Foroushani, B. J. Tully, Z. A. Taylor, et al. Subject-specific multi-poroelastic model for exploring the risk factors associated with the early stages of Alzheimer’s disease. *Interface focus*, 8(1):20170019, 2018.
- [29] A. C. Guyton and J. E. Hall. Textbook of medical physiology. 11th. *WB Saunders Company, Philadelphia*, 2006.
- [30] P. Hadaczek, Y. Yamashita, H. Mirek, L. Tamas, M. C. Bohn, C. Noble, J. W. Park, and K. Bankiewicz. The “perivascular pump” driven by arterial pulsation is a powerful mechanism for the distribution of therapeutic molecules within the brain. *Molecular Therapy*, 14(1):69–78, 2006.
- [31] M.-J. Hannocks, M. E. Pizzo, J. Huppert, T. Deshpande, N. J. Abbott, R. G. Thorne, and L. Sorokin. Molecular characterization of perivascular drainage pathways in the murine brain. *Journal of Cerebral Blood Flow & Metabolism*, 38(4):669–686, 2018.
- [32] I. F. Harrison, B. Siow, A. B. Akilo, P. G. Evans, O. Ismail, Y. Ohene, P. Nahavandi, D. L. Thomas, M. F. Lythgoe, and J. A. Wells. Non-invasive imaging of CSF-mediated brain clearance pathways via assessment of perivascular fluid movement with DTI MRI. *eLife*, 7:e34028, 2018.
- [33] P. Hauseux, J. S. Hale, S. Cotin, and S. P. A. Bordas. Quantifying the uncertainty in a hyperelastic soft tissue model with stochastic parameters. *Applied Mathematical Modelling*, 62:86–102, oct 2018.
- [34] S. B. Hladky and M. A. Barrand. Mechanisms of fluid movement into, through and out of the brain: evaluation of the evidence. *Fluids and Barriers of the CNS*, 11(1):26, 2014.
- [35] S. B. Hladky and M. A. Barrand. Elimination of substances from the brain parenchyma: efflux via perivascular pathways and via the blood–brain barrier. *Fluids and Barriers of the CNS*, 15(1):30, 2018.
- [36] K. E. Holter, B. Kehlet, A. Devor, T. J. Sejnowski, A. M. Dale, S. W. Omholt, O. P. Ottersen, E. A. Nagelhus, K.-A. Mardal, and K. H. Pettersen. Interstitial solute transport in 3D reconstructed neuropil occurs by diffusion rather than bulk flow. *Proceedings of the National Academy of Sciences*, 114(37):9894–9899, 2017.
- [37] J. J. Iliff, M. Wang, Y. Liao, B. A. Plogg, W. Peng, G. A. Gundersen, et al. A paravascular pathway facilitates CSF flow through the brain parenchyma and the clearance of interstitial solutes, including amyloid beta. *Sci Transl Med*, 4(147):147ra111, 2012.
- [38] J. J. Iliff, M. Wang, D. M. Zeppenfeld, A. Venkataraman, B. A. Plog, Y. Liao, R. Deane, and M. Nedergaard. Cerebral arterial pulsation drives paravascular CSF–interstitial fluid exchange in the murine brain. *Journal of Neuroscience*, 33(46):18190–18199, 2013.
- [39] N. A. Jessen, A. S. F. Munk, I. Lundgaard, and M. Nedergaard. The glymphatic system: a beginner’s guide. *Neurochemical research*, 40(12):2583–2599, 2015.

- [40] B.-J. Jin, A. J. Smith, and A. S. Verkman. Spatial model of convective solute transport in brain extracellular space does not support a 'glymphatic' mechanism. *The Journal of general physiology*, 148(6):489–501, 2016.
- [41] V. Kiviniemi, X. Wang, V. Korhonen, T. Keinänen, T. Tuovinen, J. Autio, P. LeVan, S. Keilholz, Y.-F. Zang, J. Hennig, et al. Ultra-fast magnetic resonance encephalography of physiological brain activity–glymphatic pulsation mechanisms? *Journal of Cerebral Blood Flow & Metabolism*, 36(6):1033–1045, 2016.
- [42] J. Krejza, M. Arkuszewski, S. E. Kasner, J. Weigele, A. Ustymowicz, R. W. Hurst, B. L. Cucchiara, and S. R. Messe. Carotid artery diameter in men and women and the relation to body and neck size. *Stroke*, 37(4):1103–1105, 2006.
- [43] P. Lacolley, P. Challande, S. Boumaza, G. Cohuet, S. Laurent, P. Boutouyrie, J.-A. Grimaud, D. Paulin, J.-M. D. Lamaziere, and Z. Li. Mechanical properties and structure of carotid arteries in mice lacking desmin. *Cardiovascular research*, 51(1):178–187, 2001.
- [44] F. Lindgren, H. Rue, and J. Lindström. An explicit link between Gaussian fields and Gaussian Markov random fields: the stochastic partial differential equation approach. *Journal of the Royal Statistical Society: Series B (Statistical Methodology)*, 73(4):423–498, 2009.
- [45] A. Louveau, B. A. Plog, S. Antila, K. Alitalo, M. Nedergaard, and J. Kipnis. Understanding the functions and relationships of the glymphatic system and meningeal lymphatics. *The Journal of clinical investigation*, 127(9):3210–3219, 2017.
- [46] A. Louveau, I. Smirnov, T. J. Keyes, J. D. Eccles, S. J. Rouhani, J. D. Peske, N. C. Derecki, D. Castle, J. W. Mandell, K. S. Lee, et al. Structural and functional features of central nervous system lymphatic vessels. *Nature*, 523(7560):337, 2015.
- [47] Q. Ma, M. Ries, Y. Decker, A. Müller, C. Riner, A. Bücker, K. Fassbender, M. Detmar, and S. T. Proulx. Rapid lymphatic efflux limits cerebrospinal fluid flow to the brain. *Acta neuropathologica*, pages 1–15, 2019.
- [48] H. Mestre, J. Tithof, T. Du, W. Song, W. Peng, A. M. Sweeney, G. Olveda, J. H. Thomas, M. Nedergaard, and D. H. Kelley. Flow of cerebrospinal fluid is driven by arterial pulsations and is reduced in hypertension. *Nature communications*, 9(1):4878, 2018.
- [49] R. Mollanji, R. Bozanovic-Sosic, A. Zakharov, L. Makarian, and M. G. Johnston. Blocking cerebrospinal fluid absorption through the cribriform plate increases resting intracranial pressure. *American Journal of Physiology-Regulatory, Integrative and Comparative Physiology*, 2002.
- [50] R. B. Nelsen. *An introduction to copulas*. Springer Science & Business Media, 2007.
- [51] C. Nicholson. Diffusion and related transport mechanisms in brain tissue. *Reports on progress in Physics*, 64(7):815, 2001.
- [52] C. Nilsson, F. Stahlberg, C. Thomsen, O. Henriksen, M. Herning, and C. Owman. Circadian variation in human cerebrospinal fluid production measured by magnetic resonance imaging. *American Journal of Physiology-Regulatory, Integrative and Comparative Physiology*, 262(1):R20–R24, 1992.
- [53] D. Orešković, M. Radoš, and M. Klarica. New concepts of cerebrospinal fluid physiology and development of hydrocephalus. *Pediatric neurosurgery*, 52(6):417–425, 2017.

- [54] D. Orešković, M. Radoš, and M. Klarica. Role of choroid plexus in cerebrospinal fluid hydrodynamics. *Neuroscience*, 354:69–87, 2017.
- [55] R. Potsepaev and C. L. Farmer. Application of stochastic partial differential equations to reservoir property modelling. In *ECMOR XII-12th European Conference on the Mathematics of Oil Recovery*, volume 2, 2014.
- [56] S. S. Prabhu, W. C. Broaddus, G. T. Gillies, W. G. Loudon, Z.-J. Chen, and B. Smith. Distribution of macromolecular dyes in brain using positive pressure infusion: a model for direct controlled delivery of therapeutic agents. *Surgical neurology*, 50(4):367–375, 1998.
- [57] A. Quaglino, S. Pezzuto, and R. Krause. Generalized Multifidelity Monte Carlo Estimators. *Preprint*, 2018.
- [58] Z. Rajna, L. Raitamaa, T. Tuovinen, J. Heikkilä, V. Kiviniemi, and T. Seppänen. 3D Multi-resolution Optical Flow Analysis of Cardiovascular Pulse Propagation in Human Brain. *IEEE transactions on medical imaging*, 2019.
- [59] L. Ray, J. J. Iliff, and J. J. Heys. Analysis of convective and diffusive transport in the brain interstitium. *Fluids and Barriers of the CNS*, 16(1):6, 2019.
- [60] M. Rennels, O. Blaumanis, and P. Grady. Rapid solute transport throughout the brain via paravascular fluid pathways. *Advances in neurology*, 52:431–439, 1990.
- [61] M. L. Rennels, T. F. Gregory, O. R. Blaumanis, K. Fujimoto, and P. A. Grady. Evidence for a ‘paravascular’ fluid circulation in the mammalian central nervous system, provided by the rapid distribution of tracer protein throughout the brain from the subarachnoid space. *Brain research*, 326(1):47–63, 1985.
- [62] M. E. Rice, Y. C. Okada, and C. Nicholson. Anisotropic and heterogeneous diffusion in the turtle cerebellum: implications for volume transmission. *Journal of neurophysiology*, 70(5):2035–2044, 1993.
- [63] G. Ringstad, L. M. Valnes, A. M. Dale, A. H. Pripp, S.-A. S. Vatnehol, K. E. Emblem, K.-A. Mardal, and P. K. Eide. Brain-wide glymphatic enhancement and clearance in humans assessed with MRI. *JCI insight*, 3(13), 2018.
- [64] G. Ringstad, S. A. S. Vatnehol, and P. K. Eide. Glymphatic MRI in idiopathic normal pressure hydrocephalus. *Brain*, 140(10):2691–2705, 2017.
- [65] G. Roth and U. Dicke. Evolution of the brain and intelligence. *Trends in cognitive sciences*, 9(5):250–257, 2005.
- [66] M. K. Sharp, R. O. Carare, and B. A. Martin. Dispersion in porous media in oscillatory flow between flat plates: applications to intrathecal, periarterial and paraarterial solute transport in the central nervous system. *Fluids and Barriers of the CNS*, 16(1):13, 2019.
- [67] A. J. Smith and A. S. Verkman. The ‘glymphatic’ mechanism for solute clearance in alzheimer’s disease: game changer or unproven speculation? *The FASEB Journal*, 32(2):543–551, 2017.
- [68] A. J. Smith, X. Yao, J. A. Dix, B.-J. Jin, and A. S. Verkman. Test of the ‘glymphatic’ hypothesis demonstrates diffusive and aquaporin-4-independent solute transport in rodent brain parenchyma. *Elife*, 6:e27679, 2017.

- [69] J. M. Tarasoff-Conway, R. O. Carare, R. S. Osorio, L. Glodzik, T. Butler, E. Fieremans, L. Axel, H. Rusinek, C. Nicholson, B. V. Zlokovic, et al. Clearance systems in the brain - implications for Alzheimer disease. *Nature reviews neurology*, 11(8):457, 2015.
- [70] A. L. Teckentrup, R. Scheichl, M. B. Giles, and E. Ullmann. Further analysis of multilevel Monte Carlo methods for elliptic PDEs with random coefficients. *Numerische Mathematik*, 125:569–600, 2013.
- [71] V. Thomée. On positivity preservation in some finite element methods for the heat equation. In *International Conference on Numerical Methods and Applications*, pages 13–24. Springer, 2014.
- [72] D. S. Tuch, T. G. Reese, M. R. Wiegell, N. Makris, J. W. Belliveau, and V. J. Wedeen. High angular resolution diffusion imaging reveals intravoxel white matter fiber heterogeneity. *Magnetic Resonance in Medicine: An Official Journal of the International Society for Magnetic Resonance in Medicine*, 48(4):577–582, 2002.
- [73] G. F. Vindedal, A. E. Thoren, V. Jensen, A. Klungland, Y. Zhang, M. J. Holtzman, O. P. Ottersen, and E. A. Nagelhus. Removal of aquaporin-4 from glial and ependymal membranes causes brain water accumulation. *Molecular and Cellular Neuroscience*, 77:47–52, 2016.
- [74] J. H. Wood. *Neurobiology of cerebrospinal fluid 2*. Springer Science & Business Media, 2013.
- [75] L. Xie, H. Kang, Q. Xu, M. J. Chen, Y. Liao, M. Thiagarajan, J. O’Donnell, D. J. Christensen, C. Nicholson, J. J. Iliff, et al. Sleep drives metabolite clearance from the adult brain. *science*, 342(6156):373–377, 2013.
- [76] Z. Ye, Y. Liu, X. Wang, X. Chen, C. Lin, Y. Su, T. Wang, Y. Tang, Y. Wu, and C. Qin. A rhesus monkey model of common carotid stenosis. *Int J Clin Exp Med*, 9(9):17487–17497, 2016.
- [77] S. Zuzana, E. Syková, et al. Diffusion heterogeneity and anisotropy in rat hippocampus. *Neuroreport*, 9(7):1299–1304, 1998.

A Model verification

To test the numerical approximations with respect to choice of mesh and time-step parameters, we performed convergence tests for all output functionals. We tested three different meshes resulting from adaptive and uniform refinement, and three different time steps. The first refinement of the mesh was performed locally close to the outer boundary, as refinement was needed in these regions of steep concentration gradients in the first time steps. We also tested that the SUPG-method performed similar to the other methods and confirmed that the SUPG-method was not needed for stability on finer meshes.

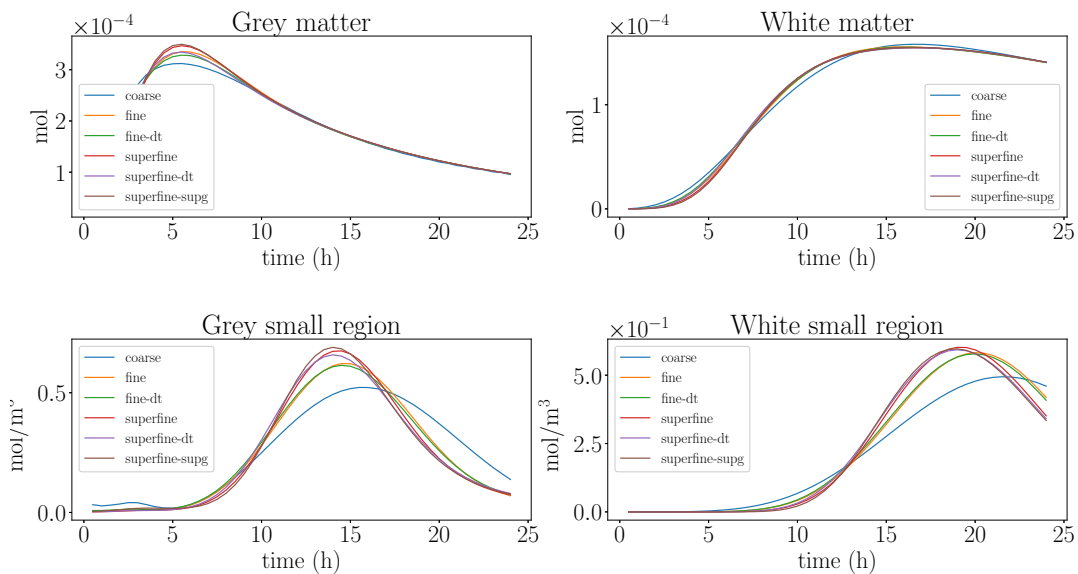


Figure 13: Convergence plots of Model V3 for a given deterministic velocity magnitude used to set up the velocity field. The local regions are more prone to error than the gray and white matter as a whole.

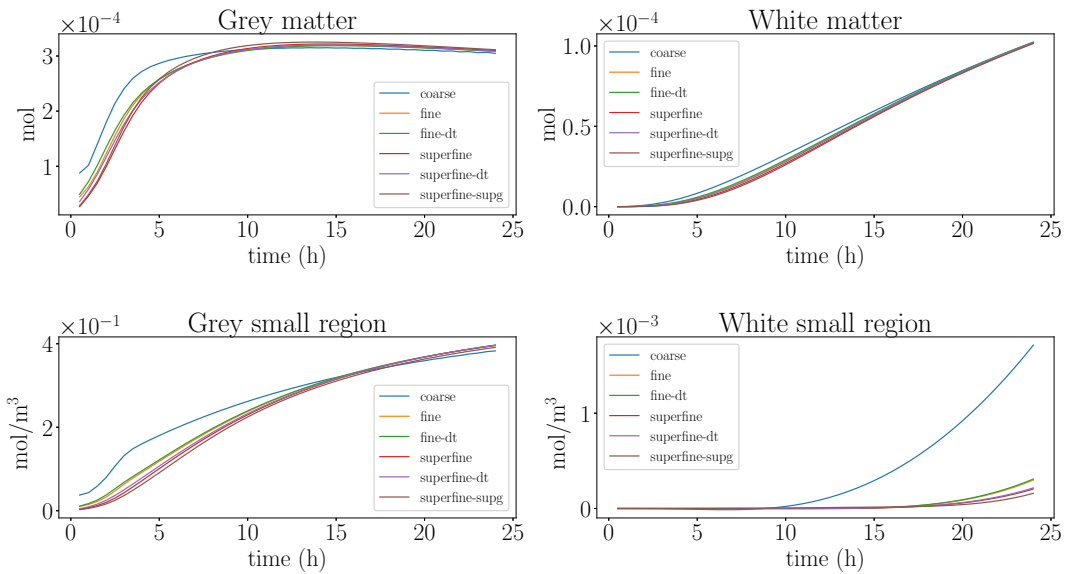


Figure 14: Convergence plots of Model V2 for a given deterministic velocity magnitude used to set up the velocity field. Due to high velocities, the mesh needs refinement to avoid considerable overshoot in the small white matter region.

Paper 4

Intracranial pressure elevation alters CSF clearance pathways

